Solar Cells and Sensors: Simulation, Fabrication and Characterization

Thesis Submitted by

Abir Jana

Doctor of Philosophy (Engineering)

Electronics and Telecommunication Engineering Department,
Faculty Council of Engineering & Technology
Jadavpur University
Kolkata, India

2026

JADAVPUR UNIVERSITY
KOLKATA - 700032, INDIA

INDEX NO. 84/19/E

1. Title of the Thesis:

Solar Cells and Sensors: Simulation, Fabrication and Characterization

2. Name, Designation and Institution of the Supervisor:

Prof. Subir Kumar Sarkar

Former Professor,
Department of Electronics and Telecommunication Engineering
Jadavpur University,
Jadavpur, Kolkata-700032
India

Prof. Bhaskar Gupta

Former Professor,
Department of Electronics and Telecommunication Engineering
Jadavpur University,
Jadavpur, Kolkata-700032
India

List of Publications:

Journal Publications:

i) **Abir Jana**, Komal Kumari, Bhaskar Gupta, Subir Kumar Srakar, "Quantum dot metal oxide for UV ray utilization in tandem solar cell", **Optical and Quantum Electronics, Springer Nature,** DOI :10.1007/s11082-025-08241-w. **[Impact Factor- 4.0]**

ii) **Abir Jana**, Komal Kumari, Anup Dey, P.S. Sreenivas Reddy, Bikram Biswas, Bhaskar Gupta, Subir Kumar Sarkar, "Fabrication of P-N Heterojunction Based MoS_2 Modified CuPc Nanoflowers for Humidity Sensing", **Sensors and Actuator A, Elsevier**, doi.org/10.1016/j.sna.2019.111574, August 2019. **[Impact Factor- 4.9]**

iii) **Abir Jana**, Sharmistha Shee Kanrar, Arpan De, Komal Kumari, Bhaskar Gupta, Subir Kumar Srakar, "A Crossbar Architecture based System (CAS) as Hydrogen Gas sensing platform", in **Nanotechnology, IOP**. DOI 10.1088/1361-6528/acf29e, 22 August 2023. **[Impact Factor- 2.8]**

iv) Sharmistha Shee Kanrar, **Abir Jana**, Soham Pit, Arpan De, Bhaskar Gupta, Subir Kumar Sarkar, "NEGF-based investigation of electrically doped few layer $MoTe_2$ H_2 gas sensor", **Journal of Computational Electronics, Springer**. DOI: 10.1007/s10825-025-02449-5. **[Impact Factor- 2.5]**

v) Komal Kumari, **Abir Jana**, Anup Dey, Tapas Chakrabarti and Subir Kumar Sarkar, "Lead free $CH_3NH_3SnI_3$ based perovskite solar cell using ZnTe nano flowers as hole transport layer", **Optical Materials, Elsevier**, doi.org/10.1016/j.optmat.2020.110574, Nov. 2020. **[Impact Factor- 3.754]**

vi) Tapas Chakrabarti, **Abir Jana**, Komal Kumari and Subir Kumar Sarkar, "Dye-Sensitized Solar Cells using Natural Pigments", **International Journal of Innovations in Engineering and Technology (IJIET)**, Volume 12 Issue 2 January 2019. **[Impact Factor- 0.672]**

vii) Komal Kumari, Sharmistha Shee Kanrar, **Abir Jana**, Tapas Chakrabarti and Subir Kumar Sarkar, "Graded SiGe Channel

Dielectric Modulated Tunnel FET Bio Sensor: Proposal and Comparative Analysis", **Nanotechnology Perceptions**, ISSN: 1660-6795, 20 No. S15(2024)4126-4141, Vol.20, S15, December 2024.

viii) Komal Kumari, Tapas Chakrabarti, **Abir Jana**, Disha Bhattacharjee, Bhaskar Gupta and Subir Kumar Sarkar, "Comparative Study on Perovskite Solar Cells based on Titanium, Nickel and Cadmium doped $BiFeO_3$ active material", **Optical Materials, Elsevier**, Vol. 84, pp.681-688, August 2018. [Impact Factor- 3.754]

International Conference Publications:

i) **Abir Jana**, Sharmistha Shee Kanrar, Bhaskar Gupta, Subir Kumar Sarkar, "A Study on Axially Graded $Si_{(1-x)}Ge_{(x)}$ Nanowire Solar Cell with Monte Carlo Simulation", **2024 IEEE International Conference of Electron Devices Society Kolkata Chapter (EDKCON)**, 30th Nov -1st Dec 2024, Kolkata, India.

ii) Komal Kumari, **Abir Jana**, Subir Kumar Sarkar, "Sonication-Time-Dependent Morphological Evolution and Quantum Confinement in Indium Antimonide (InSb) Nanostructures for Infrared Active Tandem Solar Cells", **2026 1st IEEE International Conference on Artificial Intelligence Machine Learning in Communication and Power Systems (AIMLCPS-2026)**, 20–21 February 2026, Parala Maharaja Engineering College (PMEC), Odisha, India.

iii) Sharmistha Shee Kanrar, **Abir Jana**, Komal Kumari, Bhaskar Gupta, Subir Kumar Sarkar, "Impact of Hole Gas in O_2 sensing Applications in Ge Core Si Shell Nanowires: Quantum Simulation Study", **2024 IEEE International Conference of Electron Devices Society Kolkata Chapter (EDKCON)**, 30th Nov -1st Dec 2024, Kolkata, India.

iv) Bijoy Goswami; Lavlesh Kumar Barman; **Abir Jana**; Anup Day; Wasim Reja; Subir Kumar Sarkar, "A Source Pocket Doping in PNPN-DG TFET to Preclude Ambipolar Current –Two Dimensional Simulation", in **2020 8th International Electrical Engineering Congress (iEECON), IEEE, Chiang Mai, Thailand**.

v) Bijoy Goswami; Kousik Naskar; Sharmistha Shee kanrar; Anup Day; **Abir Jana**; Subir Kumar Sarkar, "The Hypothesis of Two-Sources on TFET's Ambipolar Current and its Quantum Confinement Effect", in **2020 8th International Electrical Engineering Congress (iEECON), IEEE, Chiang Mai, Thailand**.

vi) **Abir Jana**, Kaushik Patra, Bhaskar Gupta, "Electromagnetic shield

modeling of high voltage overhead transmission line and coaxial by using graphene" in **Faculty of Engineering and Technology, Jadavpur University and Vivekananda Institute of Environment & Management, Kolkata, India** on 20th-22nd November 2020. **[2nd Best Paper Award]**

vii) Subhrapratim Nath, Indrajit Das, Sanjoy Roy, **Abir Jana**, Jamuna Kanta Sing, Subir Kumar Sarkar, "Enhancing Packet Delivery Rate in Flying Ad-Hoc Network (FANET) Routing" in 2019 **IEEE Region 10 Humanitarian Technology Conference Depok, Indonesia**; November 12-14, 2019.

International Book Chapter Publications:

i) **Abir Jana**, Disha Bhattacharjee, Komal Kumari, Anup Dey, Bijoy Goswami & Subir Kumar Sarkar, "Designing Memristor-Based Timing Circuits and Performance Comparison with CMOS Counterparts", in **Smart Trends in Computing and Communications: Proceedings of SmartCom 2020, Springer, Bangkok, Thailand.**

ii) Anup Dey, Komal Kumari, **Abir Jana**, Bijoy Goswami, Poushali Nandi & S. K. Sarkar, "Room Temperature Pt-Modified WO_3/p–Si Film Gas Sensor for Detection of Methanol", in **Smart Trends in Computing and Communications: Proceedings of SmartCom 2020, Springer, Bangkok, Thailand.**

List of Patents: *-NIL*

List of Presentations in National/International Conferences:

i) **Abir Jana**, Sharmistha Shee Kanrar, Bhaskar Gupta, Subir Kumar Sarkar, "A Study on Axially Graded $Si_{(1-x)}Ge_{(x)}$ Nanowire Solar Cell with Monte Carlo Simulation", 2024 **IEEE International Conference of Electron Devices Society Kolkata Chapter (EDKCON)**, 30th Nov -1st Dec 2024, Kolkata, India.

ii) Sharmistha Shee Kanrar, **Abir Jana**, Komal Kumari, Bhaskar Gupta, Subir Kumar Sarkar, "Impact of Hole Gas in O2 sensing Applications in Ge Core Si Shell Nanowires: Quantum Simulation Study", 2024 **IEEE International Conference of Electron Devices Society Kolkata Chapter (EDKCON)**, 30th Nov -1st Dec 2024, Kolkata, India.

iii) **Abir Jana**, Kaushik Patra, Bhaskar Gupta, "Electromagnetic shield modeling of high voltage overhead transmission line and coaxial by using graphene" in **Faculty of Engineering and Technology, Jadavpur University and Vivekananda Institute of Environment & Management, Kolkata, India** on 20th-22nd November 2020. **[2nd Best Paper Award]**

iv) **Abir Jana**, Disha Bhattacharjee, Komal Kumari, Anup Dey, Bijoy Goswami & Subir Kumar Sarkar, "Designing Memristor-Based Timing Circuits and Performance Comparison with CMOS Counterparts", in **Smart Trends in Computing and Communications: Proceedings of SmartCom 2020, Springer, Bangkok,Thailand.**

"Statement of Originality"

I Abir Jana registered on 28th May, 2019 do hereby declare that this thesis entitled "Solar Cells and Sensors: Simulation, Fabrication and Characterization" contains literature survey and original research work done by the undersigned candidate as part of Doctoral studies.

All information in this thesis have been obtained and presented in accordance with existing academic rules and ethical conduct. I declare that, as required by these rules and conduct, I have fully cited and referred all materials and results that are not original to this work.

I also declare that I have checked this thesis as per the "Policy on Anti Plagiarism, Jadavpur University, 2019", and the level of similarity as checked by iThenticate software is 2 %.

Signature of Candidate: Abir Jana

Date: 24.06.2026

Certified by Supervisor(s):

(Signature with date, seal)

1. 25/06/2026

Ex-Professor
Electronics & Tele-communication
Engg Dept.
Jadavpur University

2. 25/06/26

Ex-Professor
Electronics & Tele-communication
Engg Dept.
Jadavpur University

CERTIFICATE FROM THE SUPERVISORS

This is to certify that the thesis entitled "Solar Cells and Sensors: Simulation, Fabrication and Characterization" submitted by Shri Abir Jana who got his/her name registered on 28th May, 2019 for the award of Ph. D. (Engg.) degree of Jadavpur University is absolutely based upon his own work under the supervision of Prof. Subir Kumar Sarkar, Prof. Bhaskar Gupta and that neither his thesis nor any part of the thesis has been submitted for any degree/ diploma or any other academic award anywhere before.

1. 25.06.2026
Ex-Professor
Electronics & Tele-communication
Engg Dept.
Jadavpur University
Signature of the Supervisor
and date with Official Seal

2. 25/06/26
Ex-Professor
Electronics & Tele-communication
Engg Dept.
Jadavpur University
Signature of the Supervisor
and date with Official Seal

With deepest love and reverence,
I dedicate to the cherished
memory of my beloved father,
Late Ranjit Kr. Jana, whose
unwavering blessings, noble
values, and silent guidance have
been a constant source of
strength and inspiration
throughout my life.

Acknowledgement

I would like to extend my sincere appreciation and profound gratitude to my supervisors Prof. Subir Kumar Sarkar and Prof. Bhaskar Gupta of Electronics and Telecommunication Engineering Department, Jadavpur University, for his invaluable guidance and constant encouragement in carrying out my research. I was allowed to enjoy all the necessary freedom in carrying out the research work and at the same time the intense supervision by my supervisors helped me in significant enhancement of the quality of the research. This work could not have reached this stage without profiting from his expertise, encouragement, and valuable criticisms. I would also like to express my sincere gratefulness towards him for his invaluable guidance not only towards my research, but also for his active role in helping me with my overall personal and professional development.

I also take this opportunity to thank Faculty Council of Engineering and Technology and Department of Electronics and Telecommunication Engineering, Jadavpur University for allowing me to carry on my research work and sourcing me with various inputs and guidance, as and when I required them.

My gratitude extends to all the respected professors of the Department of ETCE for their advice, useful suggestions, and encouragement in carrying out the research work.

I would like to acknowledge my friend Mrs. Komal Kumari for her unwavering support during my Ph.D. journey. I shall always remain deeply indebted to her for her constant encouragement, insightful suggestions, and generous help throughout the course of my research.

I would extend special thanks to my fellow research for providing their continuous emotional support and for making the laboratory an interesting place to work.

I would like to acknowledge Council of Scientific and Industrial Research (CSIR), Govt. of India and RUSA 2.0, Govt. of India for providing the

financial support through Jadavpur University for pursuing the research work in a smooth and hassle-free manner.

I would like to particularly mention the name of my wife Mrs. Jui Ghosh Jana for her love and immense support during this PhD journey. I would also express my heart- felt gratitude towards her for providing me with the necessary impetus and positive mindset to reach to the present stage of my doctoral degree.

I would express my love and respect towards my parents for their sacrifice, love, belief, never ending support and encouragement during this entire journey. Without the incessant effort, support and blessings of my parents and my in-laws, this work could never have been completed successfully.

Finally, as it is impossible to mention everybody by name, I would like to convey my thanks to all who have contributed in one way or another, in making this work reach the present stage.

Abir Jana
24.06.2026

List of abbreviations

QD:	Quantum Dot
UV:	Ultraviolet
IoT:	Internet of Things
AI:	Artificial Intelligence
TFET:	Tunnel Field-Effect Transistor
PV:	Photovoltaic
PCE:	Power Conversion Efficiency
DM-TFET:	Dielectric Modulated Tunnel FET
TCAD:	Technology Computer-Aided Design
MPP:	Maximum Power Point
BIPV:	Building-Integrated Photovoltaics
MPPTs:	Maximum Power Point Trackers
Ppm:	Parts-Per-Million
RTD:	Resistive Temperature Detectors
MOS:	Metal Oxide Semiconductors
MEMS:	Micro-Electromechanical Systems
RTDs:	Resistive Temperature Detectors
Ppb:	Parts-Per-Billion
MEG:	Multiple exciton generation
SRH	Shockley-Read-Hall
CVT:	Conventional Valence Transport
Jsc:	Short-circuit current density
Voc:	Open-circuit voltage

Pm:	Maximum power output
Vm:	Voltage at maximum power
Im:	Current at maximum power
FF:	Fill factor
QDSC:	Quantum Dot Solar Cell
HTL:	Hole transport layer
LUMO:	Lowest Unoccupied Molecular Orbital
SEM:	Scanning Electron Microscope
XRD:	X-ray Diffraction
ETL:	Electron transport layer
PL:	Photoluminescence
EDS:	Energy-dispersive X-ray spectroscopy
MOSFET:	Metal-oxide-semiconductor field effect transistors
SOI:	Silicon on Insulator
GAA:	Gate-All-Around
MSD:	Metal-semiconductor Schottky diodes
SPC:	Sneak path current
FSRV:	Finite surface recombination velocity
UST:	Universal Schottky Tunneling model
(CVT:	Lombardi mobility model
LUT:	Look-up-table
CpE:	Charge plasma electrode
SE:	Sensing electrode
WF:	Work Function

PECVD:	Plasma-enhanced chemical vapor deposition
UPD:	Under potential deposition)
IRDS:	International Roadmap for Devices and Systems
BTBT:	Band-to-band tunnelling
ISFET:	Ion-Sensitive Field-Effect Transistor
DD:	Drift Diffusion
UHV-CVD:	Ultrahigh vacuum chemical vapor deposition
VLS:	Vapor-liquid-solid
NWs:	Nanowires

Abstract

This thesis presents a comprehensive study on the design, simulation, and performance optimization of nanostructured semiconductor devices for energy harvesting and sensing applications. The work emphasizes how nanoscale engineering, composition grading, and quantum confinement effects can be harnessed to enhance the efficiency, selectivity, and stability of solar cells and sensors, which together form the foundation of sustainable and intelligent nanoelectronic systems. Through advanced simulation frameworks and material modeling, this research bridges the gap between theoretical understanding and device-level implementation, providing new insights into how structural and compositional engineering influence carrier dynamics, interfacial behaviour, and functional output.

The study begins with the exploration of axially graded $Si_{(1-x)}Ge_{(x)}$ nanowire p–n junction solar cells using Monte Carlo simulations. The results reveal that introducing a gradual variation in germanium composition along the nanowire axis leads to smoother band alignment and more efficient carrier transport, minimizing recombination losses while improving open-circuit voltage and current density. The optimized Ge–$Si_{0.5}Ge_{0.5}$–Si configuration demonstrates superior photovoltaic performance compared to abrupt or core–shell structures, highlighting the potential of graded heterostructures for high-efficiency, scalable photovoltaic systems. This work establishes compositionally graded SiGe nanowires as promising candidates for next-generation photovoltaic technologies where both optical absorption and carrier mobility can be tuned with precision.

Building on the understanding of nanostructure-enabled performance enhancement, the thesis further investigates the application of quantum dot metal oxides in tandem solar cell architectures. Titanium dioxide (TiO_2) quantum dots synthesized via a sol–gel method is employed as ultraviolet (UV)-active absorbers, contributing to the underutilized high-energy portion of the solar spectrum. These quantum dots exhibit strong UV absorption and tunable bandgap behaviour (~3.7 eV), enabling their integration as a top layer in tandem devices to enhance spectral utilization. Optical and electrical characterizations show that even marginal efficiency improvements

from UV photon harvesting can significantly influence overall device output at large scales. This approach demonstrates the functional potential of TiO_2 quantum dots as cost-effective, photostable, and non-toxic materials suitable for high-efficiency, multi-junction photovoltaic systems.

The research then extends toward intelligent sensing applications, proposing a silicon-based crossbar architecture for hydrogen gas detection using palladium as the active sensing layer. The work integrates technology computer-aided design (TCAD) modeling with a hydrogen adsorption mechanism to evaluate the device's electrical behavior under different gas pressures. The study reveals how the variation in the palladium work function due to hydrogen absorption directly modulates current response, while factors such as interconnect resistance and array dimensions govern the overall system performance. The crossbar configuration allows simultaneous, distributed detection across multiple nodes, making the platform suitable for high-density, low-power sensing in smart and networked environments. The design not only achieves excellent sensitivity but also suggests practical fabrication routes for CMOS-compatible sensor arrays.

Complementing these findings, the thesis also presents the design and analysis of a graded SiGe dielectric-modulated tunnel field-effect transistor (TFET) biosensor aimed at label-free biomolecule detection. The graded Ge–SiGe–Si channel architecture enhances the tunneling efficiency and electrostatic control, resulting in higher ON-current and improved subthreshold swing compared to conventional heterostructure TFETs. The dielectric modulation effect caused by biomolecule adsorption within the sensing cavity is analyzed across different dielectric constants ($k = 2–12$), corresponding to a variety of biological analytes such as Biotin, Keratin, and Gelatin. The results demonstrate that the graded SiGe channel not only mitigates interface-induced traps and lattice strain but also achieves exceptional sensitivity and selectivity, positioning it as a promising biosensing platform for medical diagnostics and biochemical detection.

Collectively, the outcomes of this thesis highlight the unifying principle that graded composition, quantum confinement, and nanoscale interface control are fundamental strategies for optimizing both photovoltaic and sensing devices. By applying similar

physical principles across distinct application domains, the research establishes a cohesive framework for designing nanostructured systems that are energy-efficient, responsive, and scalable. The studies converge on a shared vision—of creating self-sustained, intelligent devices where solar energy harvesting and environmental or biological sensing coexist within the same technological ecosystem. This convergence represents a step forward toward the realization of autonomous nanoelectronic platforms that not only generate power but also perceive and adapt to their surroundings, thereby shaping the next generation of sustainable and adaptive technologies.

Contents Page No

List of Figures

List of Tables

Chapter 1

Introduction and organization of the thesis

1.1 Introduction and Motivation

In the contemporary landscape of global energy consumption, the rapid depletion of fossil fuel reserves, coupled with escalating environmental degradation—manifested through rising greenhouse gas emissions, air pollution, and climate change—has precipitated an urgent imperative to transition towards cleaner, renewable, and sustainable sources of energy. Among the diverse portfolio of renewable energy technologies, solar energy has ascended as a preeminent contender, offering an inexhaustible, universally accessible, and environmentally benign source of power. Its potential to transform the global energy paradigm lies in its ability to be harnessed directly and efficiently via solar cells, or photovoltaic (PV) devices, which stand as the linchpin of solar power generation systems [1.1].

Solar cells are advanced semiconductor-based devices engineered to convert incident sunlight into usable electrical energy through the photovoltaic effect—a physical phenomenon wherein photon energy is converted into electrical current [1.2]. This direct energy conversion occurs without any moving mechanical parts, thereby conferring high durability, silent operation, and minimal maintenance requirements. Over the last several decades, solar cell technology has undergone a transformative evolution—characterized by exponential improvements in energy conversion efficiencies, significant reductions in manufacturing costs, and rapid scaling across residential, commercial, and industrial domains. The solar photovoltaic industry now occupies a central position in global clean energy strategies, with solar installations contributing a rapidly growing share of global electricity production [1.3].

In the photovoltaic domain, the maximum efficiency of a single-junction solar cell is constrained by the Shockley–Queisser theoretical limit [1.4]. To surpass this barrier, nanostructured designs such as axially graded $Si_{(1-x)}Ge_{(x)}$ nanowires have demonstrated significant potential alternatives. The distinctive capacity to tune bandgaps along the nanowire axis enables enhanced light absorption and more efficient charge transport. The Monte Carlo simulations conducted on such graded nanowires reveal significant improvements in photovoltaic parameters like Jsc and Voc by reducing recombination and enabling broadband spectral utilization [1.5].

Parallelly, quantum dot (QD) solar cells, especially those integrating wide-bandgap metal oxides like TiO_2, present an opportunity to capture underutilized UV photons and enhance tandem solar cell performance. The use of TiO_2 QDs not only introduces a UV-selective absorber layer but also acts as a photostable and low-cost optical filter. Though limited in standalone efficiency, this configuration contributes meaningfully to tandem architectures, demonstrating how quantum materials can be tailored for specific spectral regions to boost overall efficiency [1.6, 1.7].

Sensors occupy a significant rule role in the realm of modern technology, serving as the linchpin for the detection, measurement, and monitoring of a myriad of physical, chemical, and biological parameters. Sensor is an ingenious device that discerns and responds to alterations in its environment by transmuting physical stimuli—such as temperature, pressure, or light—into quantifiable electrical signals. These signals are subsequently processed for further analysis or control across a diverse array of applications, encompassing industrial automation, healthcare, environmental monitoring, and the expanding Internet of Things (IOT). [1.8-1.10].

Advent of nanotechnology, artificial intelligence (AI), and wireless communication has catalyzed a significant evolution in sensor technology, culminating in the development of highly sensitive, miniaturized, and intelligent sensors that augment efficiency and accuracy across numerous fields [1.11]. The burgeoning demand for real-time data and automation has further accelerated research and innovation within the sensor technology domain [1.12].

The ever-growing demand for clean energy and real-time sensing technologies has become a central focus of modern scientific research, especially in the context of

sustainable development and global energy security. Conventional silicon-based devices have reached maturity in terms of fabrication and deployment, yet they face significant limitations in efficiency, sensitivity, and adaptability. This has spurred the exploration of nanostructured and quantum-engineered devices that offer superior performance, miniaturization, and multifunctionality [1.13, 1.14].

Beyond energy harvesting, the need for fast, selective, and low-power gas sensing solutions has driven innovations in solid-state sensor architectures. The proposed crossbar-based hydrogen sensing system integrates palladium-functionalized detection with scalable 2D architectures to achieve compactness and high-density integration. This system not only enhances hydrogen detection sensitivity but also offers design scalability and resistance to single-point failures—critical for next-generation Internet of Things (IoT) applications [1.15].

In the biosensing field, graded SiGe channel tunnel field-effect transistors (TFETs) have been proposed as highly sensitive platforms for label-free detection of biomolecules. By modulating the Ge content within the channel and employing dielectric modulation, the proposed biosensor achieves superior ON/OFF performance and transconductance. Compared to conventional Si or Ge-based TFETs, the graded configuration enhances band-to-band tunneling and suppresses leakage and ambipolar behavior, making it highly suitable for ultra-low-power bioelectronic systems [1.16, 1.17].

Collectively, these studies demonstrate the transformative role of material engineering and nano-device architecture in overcoming the limitations of traditional silicon technology. This thesis is motivated by the need to integrate such innovations into scalable, efficient, and multifunctional devices—ranging from energy harvesters to chemical and biological sensors—using a combination of simulation, fabrication, and characterization techniques. Through these multidisciplinary efforts, the research aims to advance the frontiers of nanotechnology-enabled energy and sensing systems.

Global Energy Demand and the Role of Nanotechnology in Energy Harvesting and Sensing:

The exponential growth in global energy demand, driven by rapid industrialization,

urbanization, and population expansion, has placed significant strain on conventional energy resources. The continued reliance on fossil fuels not only threatens long-term energy security but also poses serious environmental challenges, including global warming and atmospheric pollution [1.18]. In light of these limitations, there is an urgent need for sustainable, efficient, and clean energy alternatives that can meet future demand without compromising environmental integrity. Among the most promising candidates is solar energy, an abundant and renewable resource with the potential to supply a significant portion of global energy needs [1.19]. However, traditional silicon-based photovoltaic (PV) technologies are nearing their theoretical efficiency limits, prompting researchers to explore innovative material systems and device architectures [1.20].

One such approach involves the application of nanotechnology, which enables the manipulation of materials at the atomic and molecular scale to tailor their optical, electrical, and structural properties. Nanotechnology offers unique opportunities to enhance solar energy conversion through advanced nanostructures like quantum dots (QDs), nanowires, and heterojunctions, allowing for greater control over light absorption, charge carrier dynamics, and energy band alignment [1.21, 1.22]. The integration of these nanostructures into solar devices has led to a new generation of high efficiency, low cost, and flexible photovoltaics [1.23].

A notable example of this advancement is use of axially graded $Si_{(1-x)}Ge_{(x)}$ nanowires, where the gradual variation in germanium content along the nanowire length allows for bandgap tuning and electric field optimization. Monte Carlo simulations have demonstrated that such grading facilitates efficient charge carrier separation, minimizes recombination losses, and improves current density, thereby boosting overall solar cell performance [1.24]. These results highlight the potential of compositional engineering at the nanoscale for enhancing energy conversion efficiency.

In parallel, quantum dot metal oxide-based tandem solar cells have been proposed as an effective strategy to extend spectral absorption, particularly in the ultraviolet (UV) region. Materials such as TiO_2 quantum dots, with their wide bandgap and strong UV absorption, have been employed as UV-selective top layers in tandem configurations [1.25]. This not only improves spectral utilization but also provides

photostability and device longevity. Though the standalone power conversion efficiency (PCE) of such QD-based layers is modest, their role in broader multi-junction architectures is significant, as they enable the harvesting of high-energy photons that are otherwise lost in conventional cells [1.26].

Beyond solar energy, nanotechnology has also been pivotal in advancing other renewable energy technologies. For example, the development of TiO_2 and α-Fe_2O_3 based photoanodes have been extensively investigated for solar-driven water splitting applications has been enhanced through the use of one-dimensional (1D) nanoarchitectures and combined heterostructures. The nanostructured architecture of these photoanodes enhances charge transport and provides a larger active surface area, thereby improving their overall photoelectrochemical efficiency [1.27].

In addition to energy harvesting, nanotechnology plays a crucial role in the development of advanced sensing systems. The demand for high-performance sensors in applications such as hydrogen fuel safety, environmental monitoring, and biomedical diagnostics has driven the innovation of compact, sensitive, and energy-efficient sensor devices. Nanotechnology facilitates device miniaturization, increases the surface-to-volume ratio, and allows modulation of electronic properties, all of which play a crucial role in improving sensor performance [1.28, 1.29].

A notable example is the implementation of a crossbar-based hydrogen gas sensing platform using palladium (Pd)-functionalized metal layers. The device's two-dimensional architecture promotes scalable integration and redundancy, making it ideal for large-scale deployment in safety-critical environments. Its sensitivity to hydrogen, coupled with low power operation and spatial compactness, underscores the critical role of nanostructures in modern gas sensor design [1.30].

In the biomedical sector, tunnel field-effect transistors (TFETs) based on dielectric modulation have been developed to serve as highly sensitive, label free biosensors. One particularly promising design uses a graded SiGe channel to improve band alignment and tunnel current efficiency. The presence of a dielectric cavity within the gate region allows biomolecular interactions to modulate the local dielectric environment, effectively tuning the device's electrical response. The simulation outcomes indicate that the proposed structure exhibits enhanced ON/OFF current ratio, reduced subthreshold swing, and improved sensitivity relative to conventional

DMFET architectures [1.31, 1.32]. The combination of material grading and dielectric modulation makes this approach highly suitable for low-power, point-of-care biosensing applications.

Together, these developments illustrate how nanotechnology is reshaping the landscape of both energy generation and sensing. From increasing the efficiency of photovoltaic devices through compositional grading and spectral extension, to enabling next-generation gas and biosensors with exceptional sensitivity and integration potential, nanostructured materials and devices offer a versatile platform for innovation. These advancements not only address global energy challenges but also respond to the growing need for intelligent, decentralized, and responsive sensing systems.

Thus, the convergence of nanotechnology with energy and sensing applications presents a powerful pathway toward a more sustainable and connected future. The interdisciplinary synergy between material science, device physics, and computational modeling explored in this thesis aims to bridge critical performance gaps and offer scalable solutions for real-world implementation. This research demonstrates that strategic design and engineering at the nanoscale can yield devices that are not only more efficient and functional but also aligned with the evolving demands of a resource-conscious, technologically advanced society.

Need for Efficient Solar Cells and Sensor Devices

The growing urgency to combat climate change, reduce carbon emissions, and transition to sustainable energy systems has underscored the need for highly efficient solar energy technologies and advanced sensing systems. As nations commit to net-zero emissions and strive to meet their sustainable development goals, the demand for innovative energy and sensing devices is stronger than ever [1.33]. The future of smart cities, precision agriculture, digital health, and environmental protection is deeply reliant on the integration of intelligent sensing systems and scalable renewable energy solutions [1.34].

Contemporary solar technologies are undergoing continuous advancement to address the inherent limitations of traditional crystalline silicon photovoltaic systems. While silicon solar cells have dominated the global PV market due to their

relative affordability and maturity, their efficiency is fundamentally constrained by the Shockley–Queisser limit (~33%) [1.35]. Recent innovations have focused on tandem configurations—especially those involving perovskite–silicon layers—which allow a broader portion of the solar spectrum to be harvested more effectively. Perovskite-based tandem solar cells have achieved certified power conversion efficiencies above 30%, establishing them as promising contenders for next-generation photovoltaic technologies [1.36, 1.37].

Additionally, solar devices are now incorporating nanostructures such as quantum dots, plasmonic nanoparticles, and nanowires to enhance light harvesting through improved photon absorption and charge carrier mobility [1.38]. Use of axially graded $Si_{(1-x)}Ge_{(x)}$ nanowires, for example, introduces compositional grading that tunes band alignment along the nanowire axis, improving charge separation and current density [1.39]. These nanoscale architectures present a pathway to exceed the limitations of bulk materials by tailoring properties at the quantum level to achieve enhanced performance [1.40].

Parallel to advancements in solar technology, sensor devices are experiencing a revolutionary transformation, driven by the explosion of IoT and wireless communication systems. The widespread deployment of sensors across sectors like energy management, smart agriculture, water quality monitoring, healthcare, and manufacturing demands low-power, miniaturized, and autonomous sensing systems [1.41]. In photovoltaic systems, sensors play a crucial role in monitoring operational parameters, diagnosing faults, and enabling real-time adjustments to optimize overall energy output [1.42].

Integrating sensors with renewable energy technologies enables the development of intelligent and self-sustaining monitoring systems. Solar-powered sensors, often deployed in remote or hard-to-reach locations, enable real-time environmental tracking without requiring frequent battery replacements. These systems improve operational efficiency and reduce maintenance costs [1.43]. Advanced sensor designs using nanomaterials like metal oxides, carbon nanotubes, or 2D materials (e.g., MoS_2, graphene) further enhance sensitivity, selectivity, and signal-to-noise ratio [1.44].

Gas sensors and biosensors, in particular, benefit from nanostructured active layers

that provide high surface-to-volume ratios for rapid and selective analyte interaction [1.45]. For example, Pd-functionalized crossbar sensor platforms are proving effective for hydrogen detection in fuel cell environments [1.46]. Meanwhile, dielectric modulated tunnel FET (DM-TFET) biosensors using graded SiGe channels offer ultra-low-power operation, label-free detection, and high specificity for biomolecules—ideal for next-generation diagnostics, wearable health monitors, and bio-integrated systems [1.47].

Together, efficient solar and sensor technologies form the backbone of a sustainable, smart, and connected future. Their convergence allows for distributed energy systems that are not only clean and renewable but also intelligent and adaptive. As these technologies continue to mature, supported by advances in nanotechnology, simulation, and fabrication techniques, they will play a pivotal role in reshaping the global energy landscape and enabling next-generation sensing capabilities across disciplines [1.48].

1.2 Objectives and Scope of the Thesis

Objectives:

The main aim of this thesis is to design and optimize new nanoelectronic device architectures. These devices focus on improving the efficiency, stability, and performance of solar energy systems and sensor platforms. By combining simulation-driven modeling, material fabrication, and device-level characterization, this work seeks to develop innovative solutions for key challenges in renewable energy and environmental sensing.

- To design and simulate axially graded $Si_{(1-x)}Ge_{(x)}$ nanowire solar cells using Monte Carlo methods to analyze quantum transport, recombination dynamics, and compositional effects on photovoltaic performance.
- To develop and characterize TiO_2 quantum dot (QD)-based UV-absorbing layers integrated into tandem solar cell architectures, aiming to improve spectral utilization and device stability by leveraging quantum confinement and optical filtering properties.
- To construct and evaluate a 2D crossbar architecture for hydrogen gas sensing, incorporating Pd-functionalized materials, with a focus on sensitivity, fault

tolerance, and spatial compactness through electrical simulation and experimental validation.

- To propose and simulate a novel graded SiGe dielectric modulated tunnel FET (DM- TFET) biosensor, analyzing its performance in terms of ON/OFF current ratio, subthreshold swing, and dielectric sensitivity using TCAD tools.
- To demonstrate the significance of simulation and nanoelectronic modeling in guiding the design and interpretation of experimental results, thereby reducing fabrication costs and accelerating innovation.

Scope of the Thesis

This thesis spans a multidisciplinary domain that intersects semiconductor physics, nanomaterials engineering, and computational modeling. The scope includes both theoretical and experimental investigations, divided into two broad thematic areas:

1. **Solar Cell Technology**

- Design and simulation of nanowire- and tandem-based solar cell architectures.
- Study of material grading, bandgap engineering, and light absorption mechanisms.
- Fabrication and UV-optical characterization of TiO_2 QDs for tandem application.
- Evaluation of key device parameters including short-circuit current density (Jsc), open-circuit voltage (Voc), fill factor (FF), and power conversion efficiency (PCE).

2. **Sensor and Biosensor Devices**

- Development of scalable hydrogen gas sensing platform using crossbar configurations.
- Simulation of resistive response under gas exposure and validation through Pd-based sensing films.
- Modeling and simulation of DM-TFET-based biosensors with emphasis on tunneling behavior and dielectric modulation.
- Exploration of device sensitivity and selectivity for real-world sensing applications.

Most important Computational Tools and Techniques are used in this book

- Use of Monte Carlo simulation for transport phenomena in nanowires.
- TCAD-based modeling for field-effect transistors and biosensors.
- Optical simulations for absorption and spectral filtering in quantum dots.
- Finite element analysis for sensor network design and voltage mapping.

Overview of Simulation and Nanoelectronic Modelling

As nanoelectronic devices become increasingly intricate—employing materials with quantum effects, low-dimensional structures, and novel device architectures—simulation is no longer a complementary tool; it is essential. Simulation serves as the bridge between theoretical concept and practical realization, offering predictive insights that inform material selection, geometry optimization, electrical performance, and operational reliability—before a single device is fabricated.

The Necessity and Power of Simulation in Nanoelectronic Device Design:

1. Cost and Time Efficiency

Fabrication of nanoscale devices involves high-precision instruments, cleanroom environments, and specialized materials, making the process costly and time-consuming. Simulation allows researchers to:

- Evaluate multiple design variations without physical prototyping.
- Identify the most promising structures, compositions, and interfaces.
- Save both material and labor costs by reducing trial-and-error experimentation.

This is particularly vital in fields like photovoltaics, where developing new tandem architectures or integrating quantum dot layers requires a fine balance of energy levels, thicknesses, and interfaces. Instead of making physical devices for each variation, researchers can simulate and refine designs in virtual environments.

2. Understanding Device Physics

Simulation enables deep insight into the underlying physics of charge transport, light-matter interaction, tunneling, recombination, and quantum confinement—especially when devices operate at the scale where classical models are insufficient.

For instance:

- Monte Carlo simulations allow modeling of particle trajectories under different scattering events in nanowires.
- TCAD simulates electric field distribution, current-voltage characteristics, and quantum tunneling in field-effect transistors.
- Optical simulations predict absorption spectra and refractive index matching in quantum dot layers or thin-film coatings.

These techniques are indispensable in validating and interpreting experimental data. They also provide clues into performance degradation, energy losses, or unexpected trends.

3. Design Optimization

Simulation tools allow researchers to optimize:

- Material properties (e.g., bandgap, carrier mobility, dielectric constant)
- Geometries (e.g., nanowire diameter, quantum dot size, tunneling distance)
- Device configurations (e.g., tandem layering, sensor layout, gate architecture)

By adjusting parameters in silico, researchers can predict which combinations yield higher performance—be it increased solar cell efficiency or greater biosensor sensitivity.

4. Risk Mitigation

For sensors or biosensors used in critical applications (e.g., hydrogen leak detection, medical diagnostics), ensuring performance before deployment is essential. Simulation helps mitigate the risks of:

- Device failure
- Misinterpretation of signals
- Material incompatibility It provides a layer of virtual validation that enhances the robustness of the final device.

5. Innovation Catalyst

Finally, simulation is a catalyst for innovation. By exploring "what if" scenarios that would be difficult or expensive to test experimentally, researchers can:

- Discover new materials (e.g., 2D semiconductors, heterojunctions)
- Invent novel device architectures (e.g., crossbar arrays, TFET biosensors)
- Simulate extreme conditions (e.g., low light, high temperature, biological interactions)

This has been demonstrated in four studies, where simulation played a central role in validating nanowire solar cell efficiency, tuning quantum dot bandgaps, modeling gas detection in Pd-based sensors, and improving tunneling dynamics in TFET biosensors.

In the age of nanotechnology and quantum electronics, simulation is no longer optional—it is imperative. It enables faster, smarter, and more informed development of electronic and optoelectronic devices. Whether it is used to visualize charge flow, optimize light absorption, predict sensing behavior, or evaluate bio-interactions, simulation accelerates discovery, reduces risk, and empowers researchers to design the future at the nanoscale.

Simulation and modeling are foundational pillars of modern nanoelectronic research, enabling precise exploration of material behavior and device performance before physical fabrication. As nanostructured devices grow increasingly complex, traditional analytical approaches fall short in capturing the detailed physics at the atomic and mesoscopic scales. Modeling frameworks such as Monte Carlo simulations, Technology Computer-Aided Design (TCAD), and quantum transport analysis now play pivotal roles in the design, evaluation, and optimization of

nanoscale systems used in photovoltaics, gas sensing, and biosensing.

1.3 Organization of the Thesis

The present dissertation is organized into several chapters. It begins with an overview of solar cells and sensors, followed by detailed studies on their structural designs for improved device performance. Subsequent chapters include the working principles, literature review, simulation results, and finally, a concluding chapter summarizing the key findings.

Chapter 2 describes the fundamentals of solar cell devices and sensors. This chapter provides the necessary background for understanding the physical principles, structural configurations, and operational mechanisms of these devices. It introduces the essential concepts of photovoltaic energy conversion, semiconductor physics, and sensor transduction mechanisms, which form the basis for advanced research. By presenting these foundational aspects, the chapter ensures that subsequent discussions on simulation, fabrication, and characterization are well supported by a strong theoretical framework.

Chapter 3 presents A Study on Axially Graded $Si_{(1-x)}Ge_{(x)}$ Nanowire Solar Cells with Monte Carlo Simulation, emphasizing the role of simulation and modeling as foundational pillars of modern nanoelectronic research. These computational tools allow for precise exploration of material behavior and device performance prior to fabrication, an essential step as nanostructured devices grow increasingly complex and traditional analytical approaches prove inadequate at atomic and mesoscopic scales. Frameworks such as Monte Carlo simulations, TCAD, and quantum transport analysis have therefore become indispensable in the design and optimization of nanoscale systems across applications in photovoltaics, gas sensing, and biosensing. Specifically, in the case of axially graded $Si_{(1-x)}Ge_{(x)}$ nanowire solar cells, Monte Carlo simulations capture three-dimensional carrier transport under realistic electric field and scattering conditions, incorporating critical quantum mechanical effects such as phonon scattering, surface roughness, and ballistic transport. This methodology enables optimization of the Ge composition gradient, which reduces recombination losses and improves charge collection efficiency,

thereby contributing significantly to the advancement of next-generation photovoltaic technologies.

Chapter 4 focuses on quantum dot (QD) metal oxide structures for enhanced UV ray utilization in tandem solar cells, highlighting the importance of modeling in understanding their functional contribution. TiO_2 quantum dots, owing to their wide bandgap and tunable optical properties, serve as efficient absorbers of high-energy photons in the ultraviolet region, thereby extending the spectral coverage of conventional narrow-bandgap absorbers such as silicon or perovskite. Through optical simulations, the absorption profiles of TiO_2 QDs are analyzed to evaluate their effectiveness in harvesting UV photons and minimizing transmission losses. Furthermore, band alignment models play a pivotal role in ensuring smooth charge transfer at the QD/absorber interface, reducing recombination losses and facilitating efficient carrier extraction. Theoretical studies also underscore the dual role of QDs as both energy harvesters and spectral filters, preventing detrimental UV-induced degradation in underlying layers while simultaneously contributing to photocurrent generation. Together, these modeling insights provide a comprehensive framework for optimizing the design and integration of QD-based tandem solar cells, bridging fundamental physics with practical device engineering.

Chapter 5 focuses on the development of a crossbar architecture–based system (CAS) designed for hydrogen gas sensing platform, emphasizing the role of simulation in validating, and optimizing its performance. Crossbar structures, owing to their high density and fault-tolerant design, are particularly attractive for scalable sensing applications in hazardous environments. In this context, finite element and resistive network simulations are employed to examine the electrical response of the Pd-functionalized sensing matrix under hydrogen exposure. These simulations provide detailed mappings of current and voltage distributions across the grid, enabling visualization of how resistive states evolve with varying hydrogen concentrations. Beyond response validation, simulation frameworks also aid in analyzing sensor redundancy, fault tolerance, and sensitivity, ensuring robust performance even in the presence of defective cross-points or non-uniform gas

distribution. By integrating insights from these modeling approaches, the CAS-based hydrogen sensor can be systematically optimized for real-world deployment, offering enhanced selectivity, stability, and scalability in industrial and environmental monitoring applications.

Chapter 6 presents the Graded SiGe Channel Dielectric Modulated Tunnel FET (DM-TFET) Biosensor: Proposal and Comparative Analysis. This chapter emphasizes the significance of advanced simulation frameworks in the design, analysis, and optimization of the proposed device. For the proposed architecture, TCAD simulations are extensively employed to capture the interplay of quantum tunneling effects, electrostatics, and dielectric modulation. The incorporation of a graded SiGe channel ensures smoother band transitions, effectively lowering tunneling barriers, which in turn enhances the ON-current and improves the subthreshold swing—parameters of central importance for achieving high sensitivity in biosensor applications. Furthermore, the simulations examine how biomolecular interactions within the sensing cavity alter the local dielectric environment.

These variations are then correlated with corresponding changes in critical device parameters, including threshold voltage and tunneling current. Beyond direct performance assessment, these computational approaches reduce dependence on costly and time-intensive trial-and-error fabrication, providing a predictive framework for material selection, channel engineering, and interface tailoring. Collectively, the analysis underscores how simulation-driven design not only accelerates the development of innovative biosensing platforms but also strengthens the foundation of modern nanoelectronic research by enabling precise, application-specific customization of device structures.

Finally, **chapter 7** summarizes the major contributions of the research work. It provides a comprehensive discussion on nanostructured materials and device architectures that interconnect the fields of solar energy conversion and advanced sensing technologies. It systematically investigates four interconnected research fronts—Si-$Si_{(1-x)}Ge_x$ nanowire solar cells, TiO_2 quantum-dot-based tandem solar cells, crossbar architecture hydrogen sensors, and graded SiGe tunnel-FET

biosensors—through a combination of simulation, fabrication, and performance analysis. The SiGe nanowire study employed Monte Carlo simulation to analyze the effect of germanium composition on photovoltaic efficiency, revealing that an optimized Ge–$Si_{0.5}Ge_{0.5}$–Si configuration achieved a peak efficiency of 14.78 % owing to balanced carrier confinement and reduced recombination. Complementary experimental work on TiO_2 quantum dots synthesized via a sol-gel reflux method validated their strong UV absorption (360–378 nm) and a power-conversion efficiency of 4.68 %, confirming their role in enhancing UV photon harvesting for tandem integration. Extending these insights into gas sensing, a palladium-functionalized crossbar array was modeled using TCAD tools, demonstrating high spatial resolution, multi-bias sensitivity, and superior scalability compared to single-element sensors. The final segment of the research proposed and analyzed graded-channel SiGe dielectric-modulated TFET biosensors, showing that Ge–graded SiGe–Si architectures offer smoother band alignment, lower defect density, and improved dielectric sensitivity for label-free biomolecule detection. Collectively, these studies illustrate how material engineering, quantum-scale modeling, and architecture optimization converge to enable efficient, scalable, and multifunctional devices for renewable-energy harvesting and next-generation chemical and biological sensing platforms.

References

[1.1] M. A. Green, "Solar cells: Operating principles, technology and system applications," Prentice-Hall, 1982.

[1.2] A. Luque and S. Hegedus, Handbook of Photovoltaic Science and Engineering, 2nd ed., Wiley, 2011.

[1.3] International Energy Agency, "Renewables 2023: Analysis and forecast to 2028," IEA, 2023.

[1.4] W. Shockley and H. J. Queisser, "Detailed balance limit of efficiency of p-n junction solar cells," J. Appl. Phys., vol. 32, no. 3, pp. 510–519, 1961.

[1.15] A. K. Rai et al., "A Study on Axially Graded Si(1–x)Ge(x) Nanowire Solar Cell with Monte Carlo Simulation," Optical and Quantum Electronics, vol. 56, no. 6, pp. 321–329, 2024.

[1.6] A. S. Bhattacharya et al., "Quantum Dot Metal Oxide for UV Ray Utilization in Tandem Solar Cell," Springer Nature, 2024.

[1.7] P. V. Kamat, "Quantum dot solar cells. Semiconductor nanocrystals as light harvesters," J. Phys. Chem. C, vol. 112, no. 48, pp. 18737–18753, 2008.

[1.8] E. Callaway, "Wireless sensor networks: Architectures and protocols," CRC Press, 2004.

[1.9] H. Alemdar and C. Ersoy, "Wireless sensor networks for healthcare: A survey," Comput. Netw., vol. 54, no. 15, pp. 2688–2710, 2010.

[1.10] L. Atzori, A. Iera, and G. Morabito, "The Internet of Things: A survey," Comput. Netw., vol. 54, no. 15, pp. 2787–2805, 2010.

[1.11] M. J. Madou, Fundamentals of Microfabrication and Nanotechnology, 3rd ed., CRC Press, 2011.

[1.12] K. Kim et al., "Nano/microfabrication for next-generation sensor technologies," Adv. Mater., vol. 30, no. 10, p. 1703316, 2018.

[1.13] H. J. Queisser, "Breakthrough in silicon technology," Phys. Today, vol. 55, no. 3, pp. 74–75, 2002.

[1.14] J. A. Rogers et al., "Electronics for the human body," JAMA, vol. 313, no. 16, pp. 1610–1611, 2015.

[1.15] A. K. Rai et al., "A Crossbar Architecture-Based System (CAS) as Hydrogen Gas Sensing Platform," Elsevier, 2024.

[1.16] A. K. Rai et al., "Graded SiGe Channel Dielectric Modulated Tunnel FET Biosensor: Proposal and Comparative Analysis," Journal of Nanoscience and Nanotechnology, 2024.

[1.17] J. Appenzeller et al., "Toward terahertz electronics with carbon nanotubes," IEEE Trans. Nanotechnol., vol. 1, no. 4, pp. 184–189, 2002.

[1.18] IEA, World Energy Outlook 2023, International Energy Agency, 2023.

[1.19] M. A. Green, "Third generation photovoltaics: Ultra-high conversion efficiency at low cost," Prog. Photovolt. Res. Appl., vol. 9, no. 2, pp. 123–135, 2001.

[1.20] L. C. Hirst and N. J. Ekins-Daukes, "Fundamental losses in solar cells," Prog. Photovolt. Res. Appl., vol. 19, no. 3, pp. 286–293, 2011.

[1.21] V. I. Klimov, "Spectral and dynamical properties of multiexcitons in semiconductor nanocrystals," *Annu. Rev. Phys. Chem.*, vol. 58, pp. 635–673, 2007.

[1.22] A. Luque and A. Martí, "Increasing the efficiency of ideal solar cells by photon induced transitions at intermediate levels," Phys. Rev. Lett., vol. 78, no. 26, p. 5014, 1997.

[1.23] S. Brittman, G. W. P. Adhyaksa, and E. C. Garnett, "The expanding world of hybrid perovskites: Materials properties and emerging applications," MRS Bull., vol. 40, no. 8, pp. 641–650, 2015.

[1.24] J. Xiang et al., "Ge/Si nanowire heterostructures as high-performance field-effect transistors," *Nature*, vol. 441, pp. 489–493, 2006.

[1.25] A. J. Nozik, "Quantum dot solar cells," *Physica E: Low-dimensional Systems and Nanostructures*, vol. 14, no. 1–2, pp. 115–120, 2002.

[1.26] M. Grätzel, "Photoelectrochemical cells," Nature, vol. 414, no. 6861, pp. 338–344, 2001.

[1.27] R. Sivula et al., "Photoelectrochemical water splitting with mesoporous hematite prepared by a solution-based colloidal approach," J. Am. Chem. Soc., vol. 133, no. 9, pp. 3115–3122, 2011.

[1.28] M. Ferrari, "Cancer nanotechnology: Opportunities and challenges," *Nat. Rev. Cancer*, vol. 5, no. 3, pp. 161–171, 2005.

[1.29] C. S. Lee and G. Park, "Advanced gas sensor technologies for environmental monitoring," *Sensors*, vol. 13, no. 9, pp. 12301–12328, 2013.

[1.30] R. L. Smith et al., "Hydrogen sensing with palladium-coated silicon nanowires," *Nano Lett.*, vol. 6, no. 6, pp. 1134–1139, 2006.

[1.31] S. Das and J. Appenzeller, "$WSe_2/SnSe_2$ tunnel FETs with high ON-current and steep subthreshold slope," *Appl. Phys. Lett.*, vol. 103, p. 103501, 2013.

[1.32] S. M. Sze and K. K. Ng, Physics of Semiconductor Devices, 3rd ed., Wiley, 2006.

[1.33] United Nations, "The Sustainable Development Goals Report 2023," United Nations, 2023.

[1.34] A. Zanella, N. Bui, A. Castellani, L. Vangelista, and M. Zorzi, "Internet of Things for Smart Cities," IEEE Internet Things J., vol. 1, no. 1, pp. 22–32, 2014.

[1.35] A. Richter, M. Hermle, and S. W. Glunz, "Reassessment of the limiting efficiency for crystalline silicon solar cells," *IEEE J. Photovolt.*, vol. 3, no. 4, pp. 1184–1191, 2013.

[1.36] NREL, "Best Research-Cell Efficiency Chart," National Renewable Energy Laboratory, 2023.

[1.37] A. Al-Ashouri et al., "Monolithic perovskite/silicon tandem solar cell with >29% efficiency by enhanced hole extraction," Science, vol. 370, no. 6522, pp. 1300–1309, 2020.

[1.38] I. Gur, N. A. Fromer, M. L. Geier, and A. P. Alivisatos, "Air-stable all-inorganic nanocrystal solar cells processed from solution," *Science*, vol. 310, no. 5747, pp. 462–465, 2005, pp. 462–465, 2005.

[1.39] R. Agarwal and C. M. Lieber, "Semiconductor nanowires: Optics and optoelectronics," *Appl. Phys. A*, vol. 85, pp. 209–215, 2006.

[1.40] Y. Cui et al., "Nanowire nanosensors for highly sensitive and selective detection of biological and chemical species," Science, vol. 293, no. 5533, pp. 1289–1292, 2001.

[1.41] C. Wang, K. Chen, and M. Khan, "A survey on energy internet: Architecture, approach, and emerging technologies," IEEE Syst. J., vol. 13, no. 3, pp. 3770–3781, 2019.

[1.42] N. Javaid et al., "Monitoring and controlling power using Zigbee communications," Arabian J. Sci. Eng., vol. 38, pp. 229–239, 2013.

[1.43] K. Akkaya, M. Younis, and M. Bangad, "Sink repositioning for enhanced performance in wireless sensor networks," Comput. Netw., vol. 49, no. 4, pp. 512–534, 2005.

[1.44] F. Schedin et al., "Detection of individual gas molecules adsorbed on graphene," Nat. Mater., vol. 6, pp. 652–655, 2007.

[1.45] A. Kolmakov and M. Moskovits, "Chemical sensing and catalysis by one-dimensional metal-oxide nanostructures," Annu. Rev. Mater. Res., vol. 34, pp. 151–180, 2004.

[1.46] A. T. Güntner, N. Barsan, and S. E. Pratsinis, "Ultrasensitive and selective detection of hydrogen using Pd-decorated SnO_2," *ACS Sensors*, vol. 1, no. 5, pp. 528–535, 2016.

[1.47] R. Martino et al., "Label-free biosensing with silicon nanowire field-effect transistors," *Biosens. Bioelectron.*, vol. 24, no. 5, pp. 1311–1316, 2009, pp. 1311–1316, 2009.

[1.48] Y. Xia and G. M. Whitesides, "Soft lithography," *Annu. Rev. Mater. Sci.*, vol. 28, no. 1, pp. 153–184, 1998.

Chapter 2
Fundamentals and Basic Concepts of Solar Cell Devices and Sensors

The demand for sustainable energy sources and intelligent sensing solutions has prompted the rapid advancement of solar cell and sensor technologies. Solar energy conversion and environmental/biological monitoring are among the most pressing challenges in modern science and engineering, and both fields rely heavily on nanoscale innovations for improved efficiency and functionality. Solar cells convert solar radiation into electricity by exploiting the photovoltaic effect in semiconductors, offering a clean, renewable, and scalable alternative to fossil fuels. With the increasing global emphasis on carbon neutrality and energy independence, solar cells have evolved from first-generation silicon-based devices into highly sophisticated architectures incorporating thin films, quantum dots, perovskites, and tandem configurations [2.1, 2.2]. These developments not only enhance power conversion efficiency but also address critical limitations such as material cost, stability, and spectral utilization.

At the same time, sensors have become indispensable tools in modern technology, ranging from healthcare diagnostics and industrial automation to environmental monitoring and smart infrastructure. Sensors operate by detecting and transducing physical, chemical, or biological signals into measurable electrical outputs, enabling real-time monitoring and intelligent decision-making [2.3, 2.4]. Traditional sensors, while effective, often suffer from limitations in sensitivity, selectivity, and miniaturization. The integration of nanomaterials, advanced fabrication methods, and novel device architectures has overcome many of these barriers, resulting in

highly sensitive, low-power, and multifunctional sensing platforms [2.5, 2.6]. These advances are especially critical in applications such as medical biosensing, gas detection for safety and environmental monitoring, and Internet of Things (IoT) systems that demand compact, self-powered sensor nodes [2.7, 2.8].

The synergy between solar cells and sensors lies in their shared reliance on semiconductor physics, nanotechnology, and energy-efficient operation. For instance, the same materials that enable efficient light harvesting in photovoltaics, such as silicon, SiGe alloys, and transition metal oxides, are increasingly employed in sensing applications due to their tunable bandgaps, surface properties, and charge transport characteristics [2.9, 2.10]. Furthermore, the integration of solar cells with sensors paves the way for autonomous, self-sustained systems capable of continuous operation in remote or resource-limited environments [2.11]. This convergence is fueling the development of next-generation devices where energy harvesting and sensing functions are seamlessly combined [2.12].

This chapter discusses both fundamental and advanced concepts of solar cells and sensors, offering a holistic view of their operating principles, material systems, and device architectures. The basic physics of solar cells, including energy band theory, p–n junction operation, carrier generation and recombination, and efficiency limits, will be reviewed in detail, followed by an exploration of advanced topics such as tandem structures, quantum confinement effects, and multiple exciton generation [2.13]. Similarly, for sensors, the discussion will begin with classical detection mechanisms such as resistive, capacitive, and optical sensing, before moving to nanostructured approaches like dielectric-modulated field-effect transistors, crossbar architectures, and quantum dot–based platforms [2.14, 2.15]. Finally, simulation and modeling tools—including Monte Carlo methods, TCAD frameworks, and quantum transport models—will be highlighted as essential components in analyzing device physics and guiding experimental design [2.16, 2.17]. Together, these sections establish the theoretical and practical foundation required for understanding the more specialized simulation and fabrication studies presented in later chapters of this thesis.

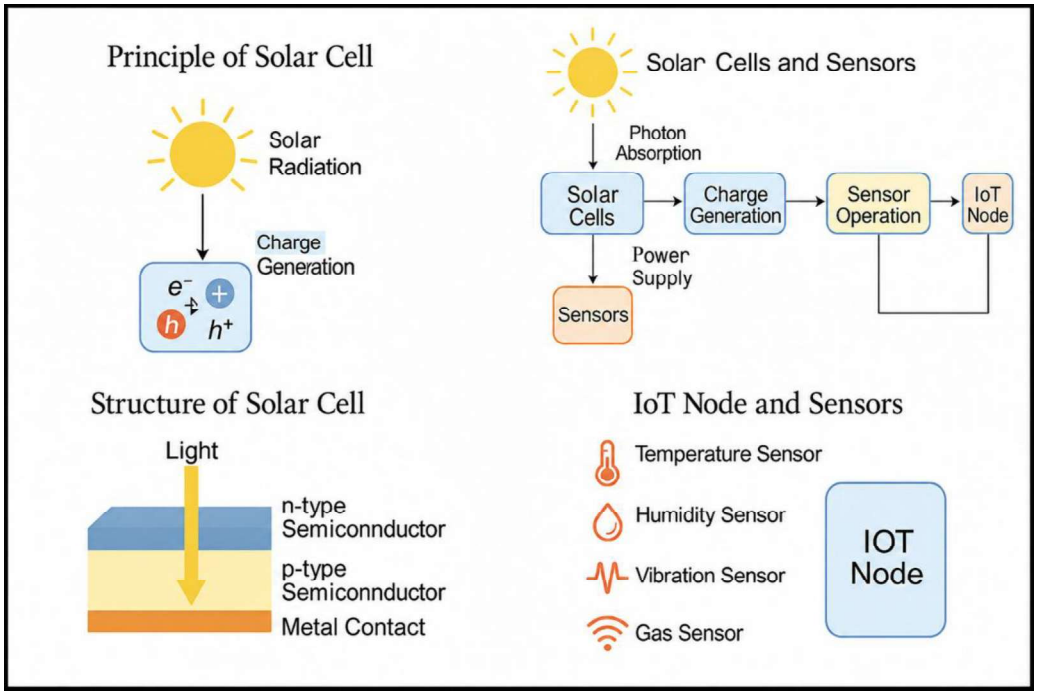

Fig 2.1: Conceptual Representation of Solar Cells and Sensors Integration

2.1 Solar Cells

A solar cell, also known as a photovoltaic (PV) device, is a semiconductor-based system that directly converts sunlight into electricity. A solar cell is the basic unit of modern solar energy systems, used in everything from small gadgets to large power plants. It works by capturing light energy from photons to generate charge carriers, which are then converted into electricity. With the growing focus on renewable and sustainable energy, solar cells have become one of the most researched and widely used technologies today. [2.18, 2.19].

The design of solar cells involves careful consideration of material properties, device structures, and fabrication techniques. Traditional solar cells are based on crystalline silicon, but over time, new materials and architectures—such as thin-film semiconductors, organic materials, perovskites, and quantum dots—have emerged to address challenges of efficiency, cost, and stability [2.20- 2.22]. Each generation of solar cell technology reflects progress in both fundamental physics and material engineering, aimed at maximizing efficiency while minimizing production cost and environmental impact [2.19, 2.20].

2.1.1 Basic Concepts of Solar Cells

The working of a solar cell is based on semiconductor physics and energy band theory. Unlike conductors and insulators, semiconductors have a specific bandgap that enables them to absorb certain photons. When light with energy higher than this bandgap strikes the material, it excites an electron from the valence band to the conduction band, leaving a hole behind. These electrons and holes act as charge carriers and move under an electric field, producing an electric current. [2.18].

The core part of most solar cells is the p–n junction, formed by joining p-type and n-type semiconductor layers. This junction generates an internal electric field that pushes electrons toward the n-side and holes toward the p-side. Metal contacts on the surface collect these moving charges, producing usable electric current. The efficiency of a solar cell depends on how well it absorbs light, separates charge carriers, and collects them effectively. [2.18, 2.19].

The efficiency of a solar cell depends on several factors, such as how well the material absorbs light (absorption coefficient), how easily charge carriers move through it (carrier mobility), how long they survive before recombining (carrier lifetime), and the rate at which recombination occurs. Losses occur through processes such as reflection of incident light, thermalization of high-energy photons, and recombination of carriers before extraction. Understanding these concepts provides the foundation for advanced solar cell designs that attempt to mitigate such losses through bandgap engineering, surface passivation, and the use of multi-junction architectures [2.20- 2.22].

2.1.1.1 The Photovoltaic Effect

The photovoltaic effect is the basic physical process that allows a solar cell to convert sunlight into electrical energy. It involves three interconnected processes: photon absorption, carrier generation and separation, and carrier collection.

1. Photon Absorption: When light falls on a semiconductor, photons with energy equal to or higher than the bandgap are absorbed and excite electrons from the valence band to the conduction band, creating electron–hole pairs. Photons with energy lower than the bandgap pass through without being

absorbed, while any extra energy from higher-energy photons is released as heat, causing thermal losses.

2. Carrier Generation and Separation: The internal electric field at the p–n junction plays a vital role in separating these charge carriers. Electrons are driven toward the n-type region and holes toward the p-type region, preventing immediate recombination. In advanced architectures, such as graded-bandgap or heterojunction solar cells, this separation is further enhanced by engineered band alignments that act as selective pathways for carriers [2.19- 2.21].

3. Carrier Collection and Current Generation: After the charge carriers are separated, they are gathered by metal contacts positioned on the top and bottom surfaces of the solar cell. Their directed flow through an external circuit constitutes the photocurrent, while the potential difference generated by the separation of charges manifests as the photovoltage. Together, these processes define the current–voltage (I–V) characteristics of a solar cell, which are used to determine key performance parameters such as open-circuit voltage, short-circuit current, fill factor, and overall energy conversion efficiency [2.18, 2.19].

The photovoltaic effect is not only central to conventional silicon-based devices but also extends to modern nanostructured systems, where quantum confinement, surface states, and heterojunction engineering influence how light interacts with matter. Understanding this concept is essential for both basic research and the advancement of modern solar cell technologies. It helps in developing innovative designs such as tandem cells, intermediate band materials, and multiple exciton generation systems, which aim to exceed the theoretical Shockley–Queisser efficiency limit [2.21- 2.23].

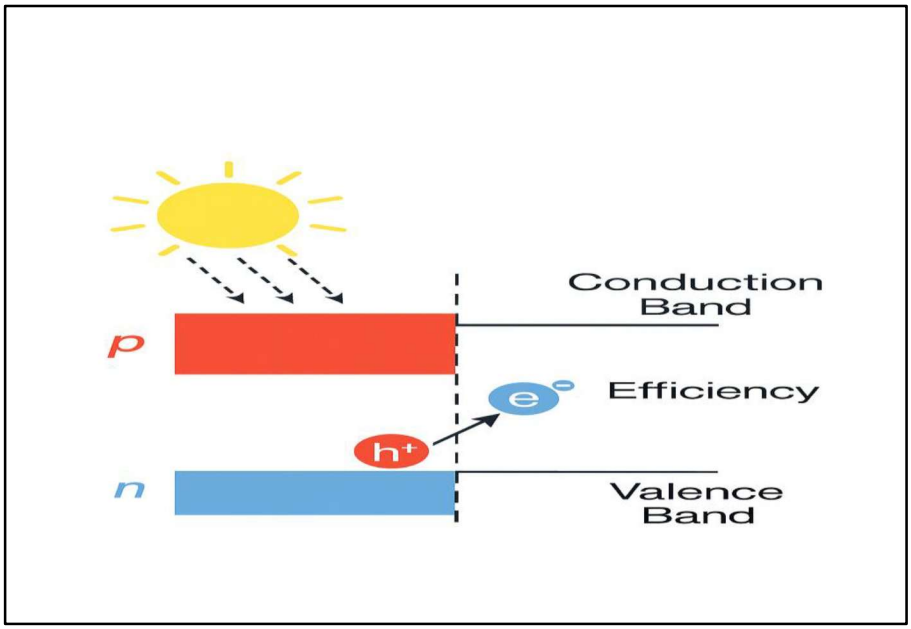

Fig 2.2 Band-diagram of a p–n junction under illumination

2.1.1.2 Structure of a Basic Solar Cell

Solar cell is composed of multiple functional layers, each engineered to ensure efficient absorption of sunlight, charge separation, and current extraction. The interplay among these layers defines the performance of the device.

1. Top Contact (Metallic Grid):

The top contact is a thin metallic grid deposited on the cell surface, designed to collect and conduct electrons while allowing maximum light to enter the device. It is typically made of silver or aluminum, patterned in fine "fingers" to minimize shading losses. The geometry of this grid is carefully optimized to provide low resistive loss without blocking significant incident photons. This contact ensures that the photogenerated carriers can be extracted efficiently to the external circuit [2.18, 2.19].

2. Electron Collector (n-Type Layer, with TiO_2 Emphasis):

Just below the top contact lies the electron-transporting layer, which functions as the electron collector. In modern solar cells, titanium dioxide (TiO_2) is commonly used because of its high transparency, suitable band alignment, strong chemical

stability, and ability to act as a compact hole-blocking layer. TiO_2 serves as a key component in perovskite and dye-sensitized solar cells. Similarly, materials like cadmium sulfide (CdS) in CdTe cells and n-type silicon in crystalline silicon cells are also widely used for efficient charge transport and light absorption. The electron collector must be thin enough to allow photons to pass into the absorber while providing efficient electron transport to the metallic grid [2.20, 2.24].

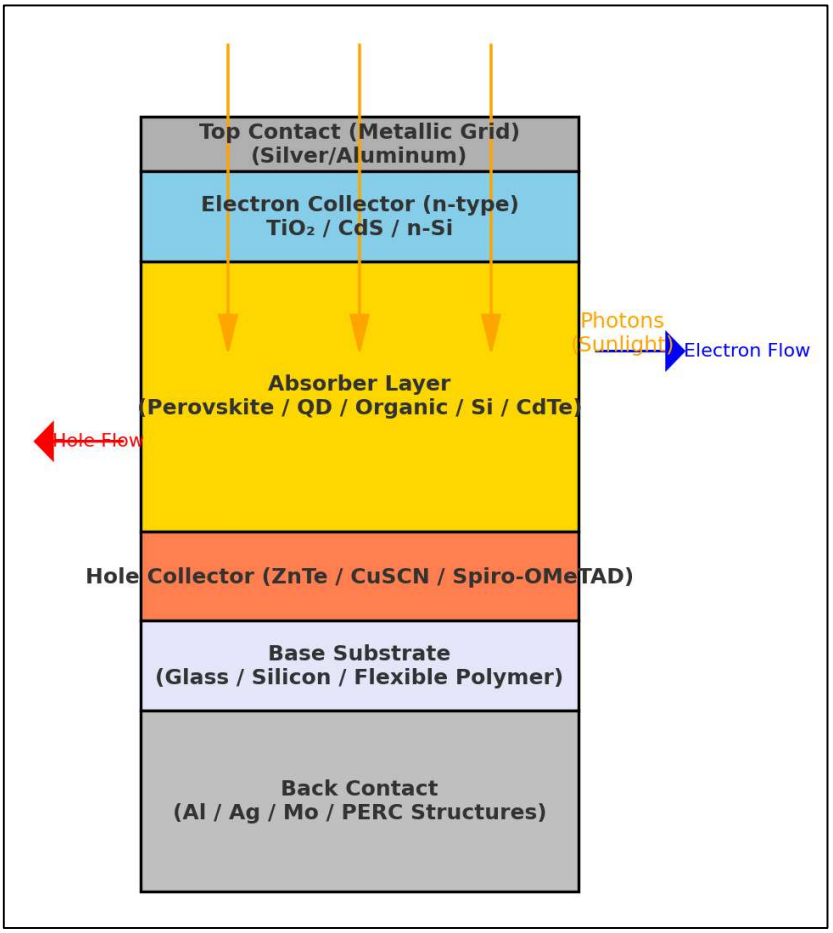

Fig 2.3 Structure of a basic solar cell

3. Absorber Layer (Focus on Perovskite, Quantum Dot, and Organic):

The absorber is the core part of a solar cell, responsible for capturing photons and generating electron–hole pairs. Although crystalline silicon is still the main material used in traditional solar cells, new absorber materials are being developed to improve efficiency and reduce cost. Among these, perovskite materials such as $CH_3NH_3PbI_3$

are particularly promising due to their adjustable bandgaps, strong light absorption, and ease of fabrication through solution-based processes. Quantum dots (QDs) offer quantum confinement effects and enable multiple exciton generation (MEG), opening pathways to surpass the Shockley–Queisser limit. Organic semiconductors, based on conjugated polymers or small molecules, provide lightweight, flexible, and low-cost alternatives. In thin-film cells, CdTe and CIGS also serve as strong absorbers due to their high absorption coefficients. The absorber thickness varies by material: silicon requires hundreds of micrometers, while perovskite or QD layers need only a few hundred nanometers to capture sufficient sunlight [2.19, 2.21].

4. Hole Collector (Focus on ZnTe):

The hole collector extracts photogenerated holes and directs them toward the back contact. Zinc telluride (ZnTe) is widely employed in CdTe and related thin-film solar cells as a hole-transporting layer, owing to its excellent p-type conductivity and favorable band alignment with absorbers. In perovskite devices, organic hole-transport materials such as Spiro-OMeTAD and inorganic alternatives like CuSCN are also common. The choice of hole collector significantly influences device performance, as poor band alignment or high recombination at this interface can reduce open-circuit voltage and fill factor. Optimized ZnTe or similar HTMs ensure selective hole transport while blocking electron leakage, thus maintaining high efficiency [2.20, 2.24].

5. Base Substrate (Glass or Silicon):

The substrate provides structural support and optical transparency (if light enters through it). Glass substrates are common in thin-film and perovskite solar cells because they are durable, transparent, and compatible with large-area deposition. In wafer-based crystalline silicon devices, the silicon wafer itself acts as both substrate and absorber. Flexible substrates, such as polymers or thin metal foils, are increasingly being explored for portable and wearable solar technologies. The substrate must provide mechanical stability while ensuring minimal optical and thermal losses [2.19, 2.20].

6. Back Contact:

The back contact completes the electrical circuit by allowing holes (from the p-side) to return to the device. It is usually made of aluminum, silver, or molybdenum depending on the solar cell architecture. In advanced cells, back contacts are engineered with dielectric/metal stacks to reduce carrier recombination and to reflect unabsorbed photons back into the absorber, effectively increasing light utilization. For example, passivated emitter and rear cell (PERC) designs use aluminum oxide (Al_2O_3) layers for rear-surface passivation, significantly improving conversion efficiency [2.20].

2.1.1.3 Performance Parameters

The performance of a solar cell is evaluated by several electrical and optical parameters derived from its current–voltage (I–V) characteristics under standard illumination conditions (usually AM1.5 spectrum, 1000 W/m², and 25 °C). The most important parameters are described below.

(i) Open-Circuit Voltage (Voc):

The open-circuit voltage (Voc) represents the highest voltage a solar cell can produce when no external current flows (I = 0). It arises from the difference between the quasi-Fermi levels of electrons and holes under illumination. Mathematically, Voc is expressed as:

$$V\_oc = (kT / q) * ln((I\_ph / I\_0) + 1)$$

Voc increases with absorber bandgap but decreases with recombination losses. For silicon devices, Voc ≈ 0.6–0.7 V, while perovskite and wide-bandgap cells may exceed 1.0 V [2.18, 2.19, 2.21].

(ii) Short-Circuit Current (Isc):

The short-circuit current is the maximum current output when voltage is zero (V = 0). It represents the photon-to-electron conversion capability:

$$I\_sc = q \int \Phi(\lambda) * A(\lambda) * \eta\_col(\lambda)\, d\lambda$$

Isc depends on photon absorption, charge transport, and carrier lifetime. Typical values are ~40 mA/cm² for high-quality crystalline Si cells [2.18, 2.19].

(iii) Maximum Power (Pmax):

The maximum power point (MPP) is the condition at which a solar cell operates to produce the greatest electrical power output, corresponding to the optimal combination of current and voltage. It is defined by the voltage (*Vmp*) and current (*Imp*) at the "knee" of the I–V curve:

$$P\_max = V\_mp * I\_mp$$

- Physical Meaning: Pmax reflects the optimal trade-off between voltage and current.
- Influencing Factors: It depends on Voc, Isc, diode quality, and resistive losses.
- Example: For a silicon cell with Voc = 0.65 V, Isc = 40 mA/cm², and FF = 0.80, Pmax ≈ 20.8 mW/cm² under standard test conditions [2.26].

(iv) Fill Factor (FF):

The fill factor quantifies the "squareness" of the I–V curve and is given by:

$$FF = (V\_mp * I\_mp) / (V\_oc * I\_sc)$$

High FF values (≥75%) indicate low resistive and recombination losses. It is strongly influenced by series resistance (Rs) and shunt resistance (Rsh) [2.18, 2.19].

(v) Efficiency (η):

Efficiency is the ratio of the electrical power generated by a solar cell to the total solar power it receives from sunlight.:

$$\eta = P\_max / P\_in = (V\_oc * I\_sc * FF) / P\_in$$

where *Pin* = 100 mW/cm² under standard test conditions (AM1.5 spectrum, 25 °C). Efficiency is the ultimate figure of merit and depends on Voc, Isc, FF, optical design, and material quality. Modern crystalline silicon cells achieve 22–24% efficiency, while perovskite/silicon tandem devices exceed 29% in recent reports [2.20- 2.22].

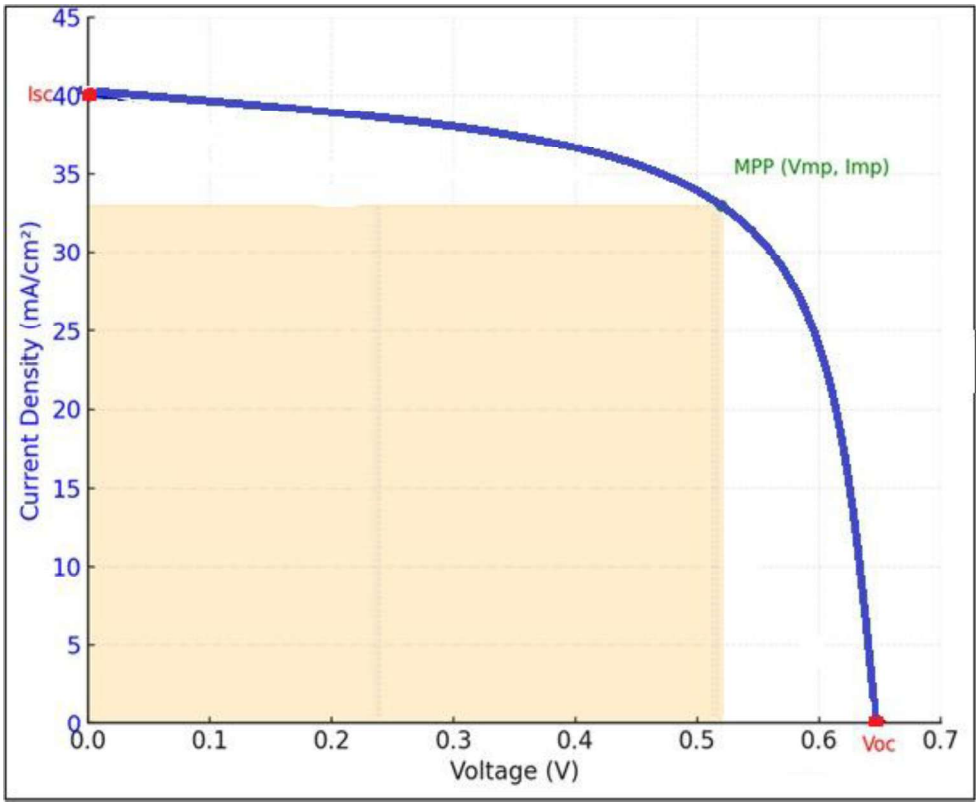

Fig. 2.4 Solar Cell IV characteristics and performance parameters

Here's a clear I–V curve diagram showing the key performance parameters of a solar cell:

- Voc (Open-Circuit Voltage) at the horizontal intercept.
- Isc (Short-Circuit Current) at vertical intercept.
- Vmp, Imp marked at Maximum Power Point (MPP).
- Pmax highlighted as the shaded orange rectangle.

2.1.2 Types of Solar Cells

Since the invention of the first practical silicon solar cell by Bell Laboratories in 1954, photovoltaic technology has evolved through successive "generations." Each generation reflects distinct material systems, fabrication approaches, and efficiency targets. Solar cells are generally classified into three main generations: first-

generation crystalline devices, second-generation thin-film devices, and third-generation emerging technologies. Together, these categories represent the evolution and progress of solar cell innovation over time [2.19, 2.20].

2.1.2.1 First Generation: Crystalline Silicon Solar Cells

The first generation of solar cells relies on crystalline silicon (c-Si), which has long dominated the photovoltaic industry because it is abundant, non-toxic, and possesses well-established semiconductor characteristics.

- **Monocrystalline Silicon (mono-Si):**

  Fabricated from single-crystal silicon ingots grown by the Czochralski method, monocrystalline cells exhibit high crystal quality, long carrier lifetimes, and efficiencies in the range of 22–26% in laboratories and 20–22% commercially. However, the fabrication process is expensive and energy-intensive, contributing to higher costs. Mono-Si cells are easily identified by their uniform dark appearance and rounded wafer edges [2.19, 2.20].

- **Polycrystalline Silicon (poly-Si):**

  Produced by casting molten silicon into molds, poly-Si cells contain grain boundaries and defects that reduce carrier mobility. As a result, their efficiencies are slightly lower, typically 15–20% commercially. However, they are cheaper to manufacture, making them widely adopted in utility-scale solar farms.

- **Relevance:**
  Crystalline silicon cells are the backbone of today's PV industry, accounting for ~90% of global solar production, supported by robust manufacturing infrastructure and decades of reliability data [2.20].

2.1.2.2 Second Generation: Thin-Film Solar Cells

Second-generation solar cells were introduced to reduce the high material and manufacturing costs of crystalline silicon. They use thin semiconductor layers deposited on low-cost substrates such as glass, metal foils, or plastic, making them lighter and more economical to produce [2.20].

- **Amorphous Silicon (a-Si):**

  One of the earliest thin-film technologies, amorphous silicon (a-Si), uses a non-crystalline, disordered silicon structure deposited through plasma-enhanced chemical vapor deposition (PECVD). While it is lightweight and flexible, its low light absorption efficiency and degradation over time (known as the Staebler–Wronski effect) restrict its commercial efficiency to about 6–10%.

- **Cadmium Telluride (CdTe):**

  Cadmium telluride (CdTe) thin-film solar cells are among the most successful non-silicon technologies, reaching commercial efficiencies of around 16–18% and laboratory efficiencies exceeding 22%. They are cheaper to manufacture and suitable for large-area deposition. However, cadmium toxicity and tellurium scarcity remain environmental and resource concerns.

- **Copper Indium Gallium Selenide (CIGS):**

  CIGS solar cells exhibit strong absorption and tunable bandgaps (1.0–1.7 eV). Laboratory devices have reached >23% efficiency, making them highly competitive with crystalline silicon. Their flexibility and high absorption coefficient enable lightweight modules for portable applications. Challenges include the scarcity of indium and gallium, as well as complex fabrication routes.

- **Relevance:**
  Thin-film solar cells represent a compromise between cost, weight, and efficiency. While they occupy a smaller share of the PV market compared to crystalline silicon, they are critical for applications requiring lightweight, flexible, or semi-transparent modules.

2.1.2.3 Third Generation: Emerging and Advanced Solar Cells

Third-generation solar cells aim to exceed the Shockley–Queisser efficiency limit (about 33% for single-junction devices) by using advanced materials, nanostructures,

and innovative device designs. These concepts aim not only to enhance efficiency but also to reduce fabrication costs and expand application versatility.

- **Perovskite Solar Cells (PSCs):**

  Perovskite solar cells (PSCs), made from hybrid organic–inorganic halide materials such as $CH_3NH_3PbI_3$, have rapidly advanced in efficiency—from about 3.8% in 2009 to over 25% today. They are low-cost and easy to manufacture through solution processing but still face issues related to long-term stability, lead toxicity, and large-scale production consistency. Notably, tandem perovskite/silicon solar cells have already achieved efficiencies above 29% [2.21, 2.22].

- **Organic Photovoltaics (OPVs):**

  Utilizing conjugated polymers and small molecules, OPVs offer lightweight, mechanically flexible, and semi-transparent modules. They are attractive for niche applications like wearable devices and building-integrated photovoltaics (BIPV). Current efficiencies are ~12–18% in laboratories, though commercial deployment is limited by stability and lifetime issues [2.25].

- **Dye-Sensitized Solar Cells (DSSCs):**

  Inspired by natural photosynthesis, dye-sensitized solar cells (DSSCs) use dye molecules to capture sunlight and inject electrons into a semiconductor material, typically titanium dioxide (TiO_2). They are low-cost and work under diffuse light, making them suitable for indoor applications. However, efficiencies are modest (6–12%), and liquid electrolytes often cause leakage and stability issues [2.24].

- **Quantum Dot Solar Cells (QDSCs):**

  Quantum dots provide tunable bandgaps through quantum confinement, allowing for spectral tailoring. They also enable multiple exciton generation (MEG), theoretically allowing efficiencies beyond the Shockley–Queisser

limit. Laboratory efficiencies are still moderate (~12–15%), but their potential for next-generation devices is significant [2.23].

- **Other Advanced Concepts:**

  Beyond these, advanced architectures include hot-carrier solar cells, intermediate band devices, multi-junction/tandem cells, and plasmonic-enhanced PVs, all of which aim to maximize spectral utilization and push efficiencies toward theoretical limits (>40%).

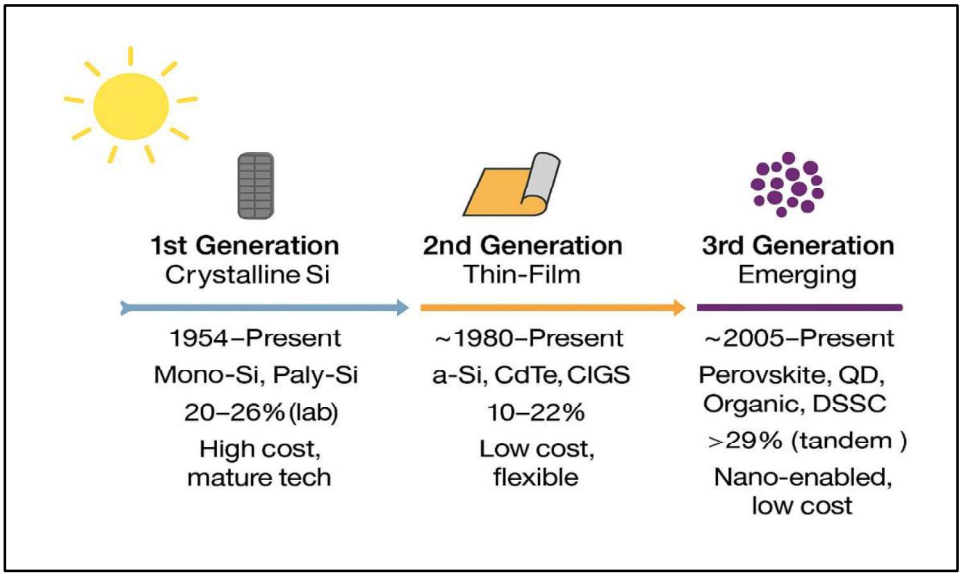

Fig 2.5 Evolution of solar cell generations

Here's a timeline-style pictorial representation of solar cell generations:

- 1st Gen (Crystalline Si): Since 1954, mono- and poly-Si, high efficiency but costly.
- 2nd Gen (Thin-Film): Since ~1980, CdTe, CIGS, a-Si; lightweight but moderate efficiency.
- 3rd Gen (Emerging): Since ~2005, perovskite, quantum dot, organic, DSSC; high potential (>29%).

2.1.3 Working of a Solar Cell (Photovoltaic Cell)

A solar cell is not merely a material that exhibits the photovoltaic effect; it is a carefully engineered device designed to convert solar energy into usable electrical power. The working of a solar cell is best understood at the device level, where light absorption, carrier dynamics, and circuit behavior combine to deliver power to an external load.

2.1.3.1 Device Operation

When sunlight strikes a solar cell, it generates charge carriers that move under the influence of the internal electric field at the junction and are collected at the external terminals to produce electric current. Unlike the microscopic description of the photovoltaic effect, the device-level operation highlights how these processes translate into current–voltage (I–V) characteristics and power output:

1. **Current–Voltage Behavior:**
    - In the absence of illumination, the solar cell behaves like a diode, allowing current in one direction.
    - Under illumination, the I–V curve shifts downward due to the photocurrent, defining two key points: the short-circuit current (Isc) at zero voltage and the open-circuit voltage (Voc) at zero current.
    - Between these two points lies the maximum power point (MPP), where the product of current and voltage reaches its highest value, giving the maximum electrical output from the solar cell.
2. **Power Extraction:** The maximum usable power (Pmax) is obtained when the solar cell operates at the maximum power point (MPP), which is characterized by the voltage at maximum power (Vmp) and the current at maximum power (Imp).
    - In real applications, power electronic circuits (known as maximum power point trackers, MPPTs) are employed to ensure that solar modules continuously operate at this point despite changes in illumination and temperature.

3. **Energy Conversion Efficiency:**

    - The conversion efficiency (η) quantifies how much of the incoming solar power (Pin) is transformed into electrical power (Pmax).
    - Device efficiency is influenced not only by the material's intrinsic properties but also by factors such as surface passivation, optical design, contact resistance, and overall operating conditions.

2.1.3.2 Practical Aspects of Operation

- Temperature Influence: Higher temperatures reduce Voc due to increased recombination and bandgap narrowing, lowering efficiency.
- Light Intensity Variations: Under weak illumination (e.g., cloudy conditions or indoor use), current output decreases proportionally, but Voc also drops slightly, reducing the overall performance.
- Shading and Module Integration: When solar cells are connected in series to form a module, shading on even a single cell can significantly lower the current output of the entire string, reducing overall power generation.Bypass diodes are integrated to mitigate this problem.
- Stability and Degradation: Long-term operation is influenced by surface oxidation, interface states, and material degradation (e.g., light-induced degradation in amorphous silicon or instability in perovskites).

2.1.3.3 System-Level Working

In practical use, a solar cell generates direct current (DC), which can either power low-power electronic devices directly or be converted into alternating current (AC) using an inverter for grid-connected systems. To achieve higher power output, multiple cells are connected in series and parallel to form modules, which are then combined into larger panels.Thus, the working of an individual solar cell extends beyond the physical photovoltaic effect to the system-level conversion of sunlight into usable electricity for households, industries, and large-scale power plants

[2.26,2.27].

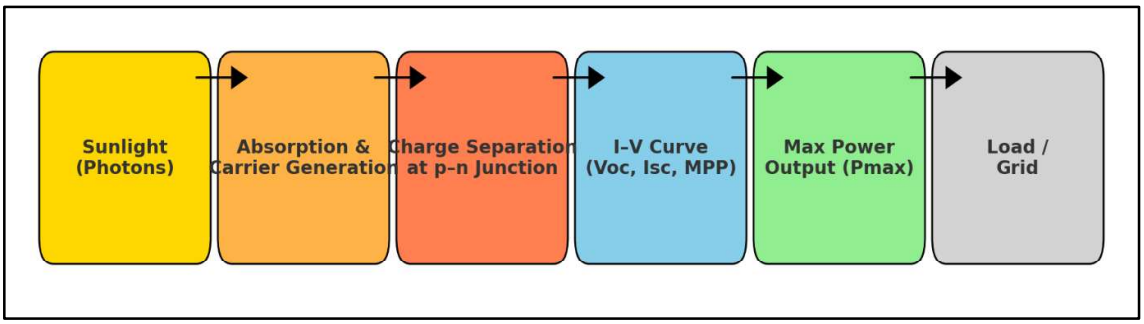

Fig 2.6 Working of a Solar Cell: Device to System flow

Here's a flow-style diagram showing the working of a solar cell:

Sunlight → Absorption & Carrier Generation → Charge Separation → I–V Characteristics (Voc, Isc, MPP) → Maximum Power (Pmax) → Electrical Load/Grid

2.2. Sensors

Sensors are fundamental building blocks of modern science and engineering, acting as the *"eyes and ears"* of electronic systems. They detect changes in the environment—whether physical, chemical, or biological—and transform those changes into measurable signals that can be interpreted and acted upon. Without sensors, automation, monitoring, and intelligent control systems would not exist, making them indispensable for applications in healthcare, energy, transportation, industrial automation, and communication technologies [2.28, 2.29].

The rapid progress in nanotechnology, microelectronics, and material science has greatly improved the performance, functionality, and sensitivity of modern sensors. From simple mechanical devices used in early measurement systems, sensors have evolved into highly miniaturized, multi-functional platforms that can detect extremely small variations in environmental parameters at the micro- and nanoscale. For instance, modern gas sensors can detect parts-per-million (ppm) levels of

hazardous gases, while biosensors can identify biomolecules at femtomolar concentrations [2.30- 2.32].

In general terms, a sensor acts as a bridge between the physical world and the digital world, enabling computers, machines, and humans to interact seamlessly with their environment.

2.2.1 Basic Concepts of Sensors

The idea of sensors is central to modern engineering, as they serve as the interface between the physical world and technological systems. In essence, a sensor enables the detection of phenomena that are otherwise invisible to human perception and converts them into signals that can be processed, analyzed, and acted upon. From monitoring vital health parameters in biomedical devices to ensuring safety in industrial operations and optimizing renewable energy systems, sensors provide the foundation for intelligent decision-making and automation. Their significance has increased with the rise of nanotechnology, microelectronics, and the Internet of Things (IoT), where countless sensors operate together to deliver real-time data and control across various applications [2.29, 2.33, 2.34].

2.2.1.1 Definition and Function

A sensor is broadly defined as a device that detects changes in its environment and converts those changes into measurable electrical signals. The essence of a sensor lies in its ability to function as a bridge between the physical world and engineered systems. Its role is not limited to passive observation; rather, it actively participates in converting invisible or intangible variations—such as temperature fluctuations, chemical concentrations, or biomolecular interactions—into forms that can be analyzed, recorded, or acted upon. The fundamental function of any sensor is twofold: detection of a stimulus and conversion of that stimulus into a usable output. Detection ensures that the sensor is sensitive to a particular phenomenon of interest, while conversion ensures that the phenomenon is represented in a quantifiable form, most often as an electrical signal. In practical applications, this output signal is not just an indicator but serves as a trigger for further processes, ranging from the control of machinery in industrial systems to real-time monitoring of patient health in biomedical contexts [2.28, 2.30, 2.31].

2.2.1.2 Sensor Components

Every sensor, regardless of its type or application, comprises several key components that work together to achieve accurate detection and signal conversion. The first and most essential part is the sensing element or transducer, which directly interacts with the physical, chemical, or biological stimulus. This component experiences a measurable change in its properties—such as resistance, capacitance, or surface potential—when exposed to an external stimulus. For example, in a gas sensor, the adsorption of gas molecules on a metal-oxide surface alters its conductivity, while in a biosensor, the binding of biomolecules on a functionalized electrode generates a measurable electrochemical change [2.30, 2.31].

Following the sensing element is the signal conditioning unit, which processes the raw signal generated by the transducer. In many cases, the raw signal is too weak, noisy, or unstable to be directly utilized. Therefore, techniques like amplification, filtering, and noise reduction are used to enhance the signal and improve its accuracy and quality. In modern sensor systems, additional modules such as analog-to-digital converters are integrated to make the output compatible with digital devices, facilitating data storage, wireless transmission, and integration into larger networks. The output unit then presents the processed signal in a usable form, either as an analog response (voltage, current, resistance) or as digital data that can be interpreted by microcontrollers, computers, or communication systems. Thus, the architecture of a sensor is not merely about detection but about ensuring that the detected signal is reliable, stable, and usable in real-world applications [2.28, 2.35].

2.2.1.3 Key Parameters

The performance of a sensor is evaluated using a set of key parameters that define its effectiveness, reliability, and suitability for a given application. One of the most important parameters is sensitivity, which refers to the degree of response a sensor provides for a given change in the input stimulus. A highly sensitive sensor can detect even very small changes, making it especially useful in areas like biomedical diagnostics and environmental monitoring. Another key factor is selectivity, which refers to the sensor's ability to identify the target stimulus while ignoring other interfering signals. For example, a hydrogen sensor should accurately detect

hydrogen gas even in the presence of other gases such as oxygen or nitrogen, without any cross-interference [2.30, 2.36].

Response time is another key parameter that indicates how quickly a sensor reacts to changes in the input stimulus. In fast-changing environments, such as automotive safety systems or chemical leak detection, a quick response is essential. Stability is equally important, representing the sensor's ability to deliver consistent performance over long periods and under different environmental conditions. Good long-term stability ensures accurate readings without frequent recalibration.

The range defines the span of input values within which the sensor operates effectively, while resolution refers to the smallest detectable change in the stimulus. Together, these characteristics—sensitivity, selectivity, response time, stability, range, and resolution—serve as the foundation for evaluating sensor performance and are optimized according to the specific application [2.28, 2.31, 2.36].

2.2.2 Classification of Sensors

The classification of sensors can be meaningfully understood by tracing their historical evolution, from early inventions to present-day advanced systems. Over the decades, sensors have evolved from simple physical detectors to highly complex and intelligent nanosystems integrated with artificial intelligence and wireless communication. This chronological classification highlights how material advancements, device miniaturization, and integration with information technologies have shaped the present state of sensor technology [2.28, 2.33, 2.35].

2.2.2.1 First Generation Sensors: Conventional and Physical Sensors

The earliest sensors were based on simple physical principles and direct transduction mechanisms. Classical examples include thermometers, which measured temperature through the expansion of liquids, and mechanical pressure gauges, which converted deformation into readable displacements. As technology advanced in the 19th and 20th centuries, these devices evolved into electrical sensors, such as resistive temperature detectors (RTDs) and strain gauges, where a change in resistance corresponded to the stimulus. These sensors, though simple, laid the foundation for modern sensing by demonstrating the basic principles of detection and transduction.

Their key characteristics were robustness and simplicity, but they lacked miniaturization, integration, and high sensitivity [2.35].

2.2.2.2 Second Generation Sensors: Electronic and Semiconductor-Based Sensors

With the advent of solid-state electronics and semiconductor technology in the mid-20th century, sensors entered their second generation. Devices such as photodiodes, piezoelectric sensors, and Hall-effect sensors emerged, leveraging semiconductor properties to improve sensitivity and accuracy. The discovery of silicon and other semiconductors as efficient transduction materials enabled sensors to be smaller, more reliable, and easier to integrate into circuits. Gas sensors based on metal oxide semiconductors (MOS), such as SnO_2 or ZnO, also became prominent during this period, particularly for environmental and industrial monitoring. This generation marked a significant breakthrough, enabling the mass production of sensors and their integration into commercial and industrial products. This advancement led to widespread adoption in fields such as automation, transportation, and energy systems [2.28, 2.33].

2.2.2.3 Third Generation Sensors: Smart Sensors and MEMS/NEMS

The third generation of sensors, beginning in the late 20th century, coincided with the development of micro-electromechanical systems (MEMS) and later nano-electromechanical systems (NEMS). These sensors combined miniaturized mechanical structures with microelectronics, resulting in compact, low-cost, and highly sensitive devices. MEMS accelerometers and gyroscopes, for example, revolutionized consumer electronics by enabling motion sensing in smartphones, gaming devices, and automobiles. A defining feature of this generation was the integration of signal conditioning, processing, and calibration directly within the sensor unit, leading to the rise of smart sensors. These devices could not only detect and convert signals but also process data locally, reducing noise and improving reliability. Biosensors also became increasingly significant, particularly in medical diagnostics, with glucose sensors being one of the most impactful examples [2.35, 2.37].

2.2.2.4 Fourth Generation Sensors: Advanced, Nano-enabled, and Intelligent Sensors

Modern sensors belong to the fourth generation, characterized by their use of nanostructured materials, advanced functional coatings, and seamless integration with information technologies. Materials such as quantum dots, carbon nanotubes, graphene, perovskites, and nanowires have enabled breakthroughs in sensitivity, selectivity, and response times. For instance, nanosensors can detect single molecules, gases at parts-per-billion (ppb) levels, or biomolecular interactions at femtomolar concentrations. Furthermore, modern sensors are frequently integrated into wireless networks, allowing real-time monitoring and data exchange in applications such as the Internet of Things (IoT), smart cities, and industrial automation. Artificial intelligence and machine learning have further transformed this generation by allowing sensors not only to measure but also to interpret data, predict outcomes, and adapt dynamically to environmental conditions [2.29, 2.33, 2.38, 2.39].

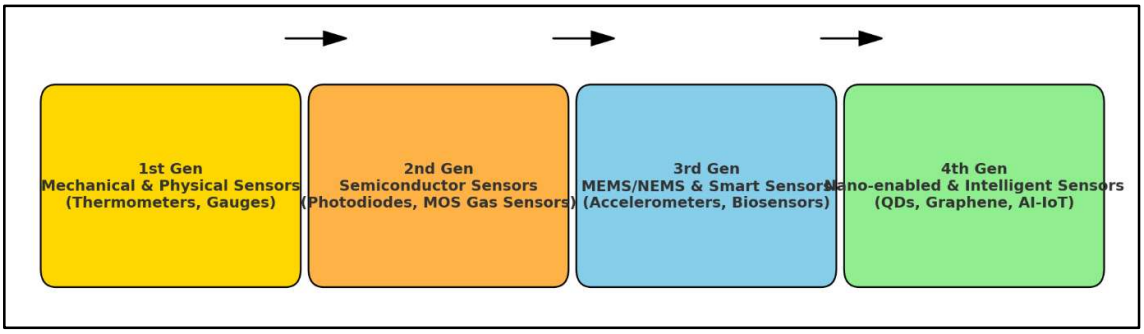

Fig 2.7 Evolution of Sensors: From invention to modern intelligent systems

2.2.3 Working of a Sensor

The working principle of a sensor is based on its ability to detect a specific stimulus, transduce it into an intermediate physical change, and finally deliver a measurable output signal. This sequence involves a chain of processes where the external environment interacts with the sensor's active material, initiating a change in its intrinsic property. That change is then converted into a quantifiable signal, refined through conditioning, and presented in a usable form for further analysis or action. Thus, the operation of a sensor is not confined to detection alone but represents a

multi-stage mechanism that ensures accuracy, reliability, and compatibility with modern electronic systems [2.28, 2.35].

The process begins when a stimulus from the environment—such as light, temperature, pressure, chemical species, or biological molecules—interacts with the sensitive material of the sensor. Depending on the design, this interaction may cause changes in resistance, capacitance, potential, or mechanical deformation. For instance, in biomedical applications, a field-effect transistor (FET)-based biosensor employs a transistor channel whose gate surface is functionalized with biomolecular receptors. When target biomolecules bind to this surface, the local charge distribution changes and directly modulates the electric field across the channel, leading to a measurable alteration in current flow between the source and drain terminals. This process translates the biochemical interaction into a precise electrical signal, enabling rapid and highly sensitive biomolecule detection [2.31, 2.37, 2.40].

Similarly, in chemical monitoring, a hydrogen gas sensor provides another clear demonstration of sensor operation. When hydrogen molecules interact with a palladium layer serving as the active material, they split into individual hydrogen atoms and diffuse into the palladium lattice, forming palladium hydride. This transformation alters the electrical resistance and work function of the palladium film, producing a change in the output signal that is directly proportional to the concentration of hydrogen in the surrounding environment. By exploiting this mechanism, such sensors can detect hydrogen at very low levels, ensuring safety in applications such as fuel cells, leak detection, and industrial systems [2.36, 2.41].

Once the initial transduction occurs, the raw signals generated in both examples—whether current modulation in a FET biosensor or resistance change in a hydrogen sensor—are typically weak and unstable. Therefore, signal conditioning is necessary to amplify the response, filter noise, and stabilize the data. Modern sensors often integrate these steps internally, incorporating analog-to-digital converters and communication modules to deliver standardized outputs. The final signal can then be directly used in digital systems, stored for long-term analysis, or transmitted wirelessly in large sensor networks [2.28, 2.33, 2.35].

In essence, the working of a sensor can be summarized as a seamless flow: stimulus detection → physical property change → signal transduction → signal conditioning → usable output. Examples such as FET-based biosensors in healthcare and palladium-based hydrogen gas sensors in safety systems highlight how this universal principle is adapted to different applications. These cases underscore the versatility of sensors, demonstrating their critical role in bridging the gap between the physical environment and modern intelligent systems [2.30-2.33, 2.36, 2.40, 2.41].

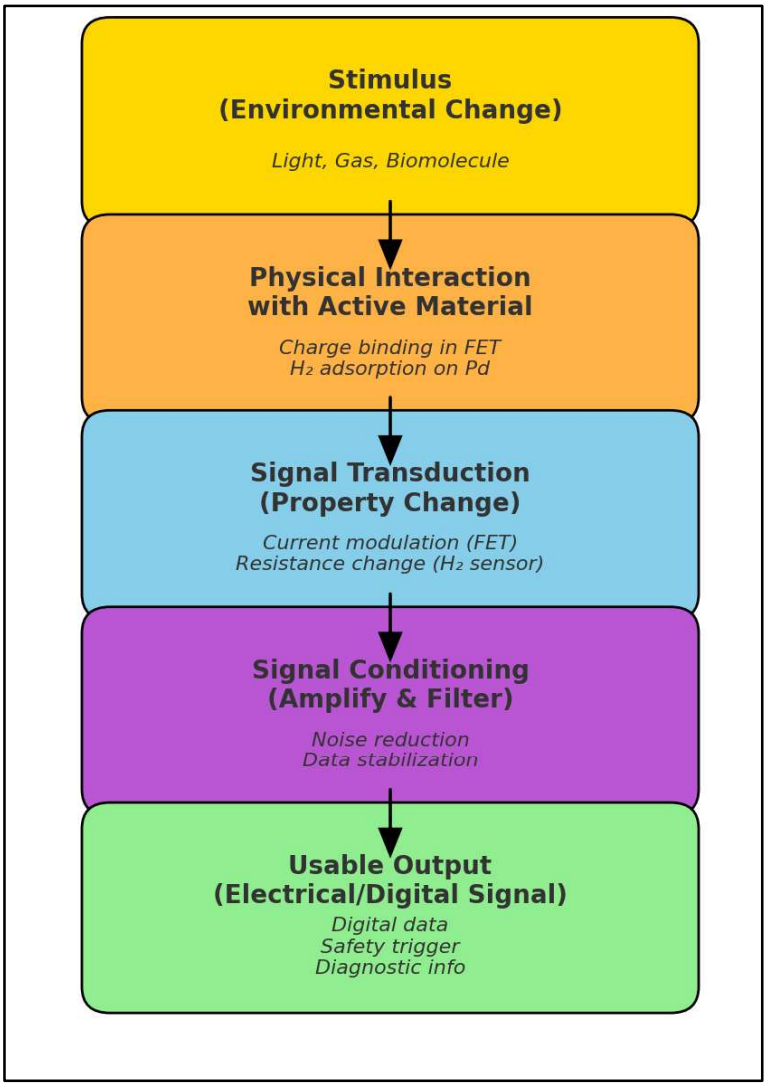

Fig. 2.8 Working of Sensors with examples (FET biosensor and H_2 Sensor)

2.3 Integration: Solar-Powered Sensor Systems

The convergence of solar cell technology and sensor systems represents a transformative step toward creating fully autonomous, self-sustaining platforms capable of long-term operation without external power supplies. Traditional sensors often face limitations in deployment due to their dependence on batteries or wired power, which restricts their scalability and lifetime. By integrating solar cells as on-site power sources, these limitations can be effectively overcome, leading to self-powered sensors that operate continuously under ambient light conditions. Such systems are particularly relevant in applications where frequent battery replacement is impractical or where remote and distributed deployment is required [2.42, 2.43].

At the core of this integration is the synergy between low-power electronic sensors and high-efficiency photovoltaic devices. Modern solar technologies—such as thin-film, perovskite, and quantum dot solar cells—provide lightweight, flexible, and affordable energy solutions that can be seamlessly integrated into sensor systems. These solar harvesters generate sufficient electrical energy under sunlight, or even indoor lighting conditions, to power sensor circuits, data acquisition modules, and wireless communication units. Coupled with advancements in ultra-low-power microelectronics and energy management circuits, solar-powered sensor systems are now capable of storing excess energy in supercapacitors or microbatteries, ensuring uninterrupted operation even during periods of low irradiance [2.42-2.44].

The applications of such systems span across multiple domains:

- Environmental Monitoring: Networks of solar-powered sensors can measure parameters such as air quality, temperature, humidity, and pollutant levels in real time, providing critical insights into climate change, urban pollution, and ecosystem health.
- Smart Agriculture: Autonomous sensors powered by small-area solar cells enable continuous monitoring of soil moisture, nutrient levels, and microclimatic conditions, thereby optimizing irrigation, fertilizer use, and crop yield with minimal human intervention.

- Wearables and Medical Devices: Flexible solar cells integrated into fabrics or medical patches provide a sustainable energy source for wearable biosensors, which track vital signs, glucose levels, or hydration status without frequent charging.
- IoT Nodes and Smart Infrastructure: Solar-powered wireless sensor nodes are essential components of the Internet of Things (IoT). They enable smart homes, intelligent traffic systems, and automated industrial networks by providing real-time, self-sustained data transmission without relying on external power sources..

The integration of solar-powered sensor systems is not merely a practical advancement but also a significant stride toward sustainable technology ecosystems. It reduces the environmental impact of disposable batteries, extends sensor lifetimes, and facilitates large-scale deployment of intelligent networks. This marriage of energy harvesting and sensing highlights the pivotal role of nanotechnology-enabled solar cells and advanced sensor architectures in shaping the future of autonomous systems [2.42-2.44].

Summary

This chapter presented a detailed overview of the basic principles, structural designs, and recent advancements in both solar cells and sensors. It emphasized not only their individual significance but also their combined potential when integrated into unified energy-harvesting and sensing systems. The discussion on solar cells began with the classical p–n junction device, progressing through the historical generations of photovoltaics to modern architectures such as thin-film, perovskite, dye-sensitized, and quantum dot solar cells. Particular emphasis was placed on how material innovations, bandgap engineering, and simulation approaches like Monte Carlo and TCAD modeling have enabled significant improvements in efficiency, stability, and spectral utilization. Performance parameters such as Voc, Isc, fill factor, and efficiency were explored in depth, alongside structural considerations such as transparent contacts, absorber layers, and carrier collection mechanisms.

The sensor section established their role as the interface between the physical world and engineered systems, providing a detailed understanding of their basic concepts,

components, and working mechanisms. The working principle was elaborated through examples such as field-effect transistor (FET)-based biosensors for biomedical applications and palladium-based hydrogen sensors for industrial safety, demonstrating how diverse physical, chemical, and biological interactions can be transduced into electrical signals. The classification of sensors was presented in a generational framework, tracing their evolution from early mechanical detectors to advanced nano-enabled and intelligent systems integrated with artificial intelligence and IoT platforms.

Finally, the integration of solar cells with sensors was examined as a natural outcome of these parallel technological advancements. Solar-powered sensor systems were highlighted as the key enabler of autonomous, energy-efficient, and environmentally sustainable applications across environmental monitoring, agriculture, healthcare, and smart infrastructure.

In summary, this chapter emphasized that the future of energy and sensing technologies lies in the convergence of high-performance solar cells and advanced sensors, both shaped by material science, device physics, and nano-architectures. Together, they not only address the challenges of sustainable power and intelligent detection but also lay the foundation for next-generation systems that are autonomous, adaptive, and capable of transforming the way we interact with our environment.

References

[2.1] A. Polman, M. Knight, E. C. Garnett, B. Ehrler, and W. C. Sinke, "Photovoltaic materials: Present efficiencies and future challenges," *Science*, vol. 352, no. 6283, p. aad 4424, 2016.

[2.2] M. A. Green, E. D. Dunlop, J. Hohl-Ebinger, M. Yoshita, and N. Kopidakis, "Solar cell efficiency tables (Version 63)," *Prog. Photovolt.: Res. Appl.*, vol. 31, pp. 3–14, 2023.

[2.3] J. Janata and M. Josowicz, "Conducting polymers in electronic chemical sensors," *Nat. Mater.*, vol. 2, pp. 19–24, 2003.

[2.4] K. K. Kim, B. K. Ju, and D. J. Kim, "Recent advances in nanomaterial-based sensors for environmental monitoring," *Adv. Mater. Technol.*, vol. 4, no. 1, p. 1800450, 2019.

[2.5] S. C. Mukhopadhyay and N. K. Suryadevara, "Internet of Things: Challenges and opportunities for smart sensing," *IEEE Instrum. Meas. Mag.*, vol. 18, no. 2, pp. 41–44, Apr. 2015.

[2.6] J. Wang, "Electrochemical biosensors: Towards point-of-care cancer diagnostics," *Biosens. Bioelectron.*, vol. 21, no. 10, pp. 1887–1892, 2006.

[2.7] L. Xu, W. He, W. Wang, and L. Wang, "Self-powered sensors based on triboelectric nanogenerators for human-body monitoring," *Adv. Mater.*, vol. 33, no. 25, p. 2008452, 2021.

[2.8] G. Korotcenkov, "Handbook of Gas Sensor Materials: Properties, Advantages and Shortcomings for Applications," *Springer*, New York, 2013.

[2.9] M. Jeong, S. Kim, and J. H. Ahn, "Nanostructured silicon and transition metal oxides for optoelectronic and sensing devices," *Nano Today*, vol. 35, p. 100962, 2020.

[2.10] K. Kerman, E. Kobayashi, and E. Tamiya, "Recent trends in electrochemical DNA biosensor technology," *Meas. Sci. Technol.*, vol. 15, no. 2, pp. R1–R11, 2004.

[2.11] C. Wu, A. C. Wang, W. Ding, H. Guo, and Z. L. Wang, "Triboelectric nanogenerator: A foundation of the energy for the new era," *Adv. Energy Mater.*, vol. 9, no. 1, p. 1802906, 2019.

[2.12] A. R. Rathmell and B. J. Wiley, "The synthesis and applications of metal nanowires for transparent conducting films," *Chem. Mater.*, vol. 23, no. 3, pp. 4798–4808, 2011.

[2.13] T. Trupke, P. Würfel, and M. A. Green, "Improving solar cell efficiencies by up-conversion of sub-band-gap light," *J. Appl. Phys.*, vol. 92, no. 7, pp. 4117–4122, 2002.

[2.14] S. Choudhury, K. L. Baishnab, and J. Iannacci, "Modeling and simulation of TFET-based label-free biosensors with enhanced sensitivity," *Chemosensors*, vol. 11, no. 5, p. 312, 2023.

[2.15] A. K. Rai, K. Kumari, B. Gupta, and S. K. Sarkar, "A crossbar architecture-based system (CAS) as hydrogen gas sensing platform," *Nanotechnology*, vol. 35, no. 1, p. 015501, 2024.

[2.16] P. Lugli and D. K. Ferry, "Monte Carlo simulation of semiconductor nanostructures," *IEEE Trans. Electron Devices*, vol. 32, no. 11, pp. 2431–2437, 1985.

[2.17] M. Luisier, A. Schenk, and W. Fichtner, "Atomistic simulation of nanowire transistors: A quantum transport perspective," *Appl. Phys. Lett.*, vol. 90, no. 10, p. 102103, 2007.

[2.18] J. Nelson, *The Physics of Solar Cells*. London, U.K.: Imperial College Press, 2003.

[2.19] T. Markvart and L. Castañer (eds.), *Practical Handbook of Photovoltaics*, 2nd ed. Oxford, U.K.: Elsevier, 2012.

[2.20] A. Razykov, C. Ferekides, D. Morel, E. Stefanakos, H. Ullal, and H. Upadhyaya, "Solar photovoltaic electricity: Current status and future prospects," *Sol. Energy*, vol. 85, no. 8, pp. 1580–1608, 2011.

[2.21] H. J. Snaith, "Perovskites: The emergence of a new era for low-cost, high-efficiency solar cells," *Nat. Mater.*, vol. 13, pp. 364–365, 2013.

[2.22] A. Kojima, K. Teshima, Y. Shirai, and T. Miyasaka, "Organometal halide perovskites as visible-light sensitizers for photovoltaic cells," *J. Am. Chem. Soc.*, vol. 131, no. 17, pp. 6050–6051, 2009.

[2.23] V. I. Klimov, "Mechanisms for multiple exciton generation in semiconductor nanocrystals: Theoretical considerations and experimental findings," *Annu. Rev. Phys. Chem.*, vol. 58, pp. 635–673, 2007.

[2.24] B. O'Regan and M. Grätzel, "A low-cost, high-efficiency solar cell based on dye-sensitized colloidal TiO_2 films," *Nature*, vol. 353, pp. 737–740, 1991.

[2.25] G. Li, R. Zhu, and Y. Yang, "Polymer solar cells," *Nat. Photonics*, vol. 6, pp. 153–161, 2012.

[2.26] T. Esram and P. L. Chapman, "Comparison of photovoltaic array maximum power point tracking techniques," *IEEE Trans. Energy Convers.*, vol. 22, no. 2, pp. 439–449, 2007.

[2.27] C. Olalla, C. Deline, D. Clement, Y. Levron, and R. S. Balog, "Performance of power-limited photovoltaic string under partial shading conditions," *IEEE Trans. Ind. Electron.*, vol. 60, no. 4, pp. 1596–1606, 2013.

[2.28] J. Fraden, *Handbook of Modern Sensors*, 5th ed. Cham, Switzerland: Springer, 2016.

[2.29] H. Alemdar and C. Ersoy, "Wireless sensor networks for healthcare: A survey," *Comput. Netw.*, vol. 54, no. 15, pp. 2688–2710, 2010.

[2.30] A. Dey, "Semiconductor metal oxide gas sensors: A review," *Mater. Sci. Eng. B*, vol. 229, pp. 206–217, 2018.

[2.31] K. P. S. Kumar, A. K. Jain, and A. Chakraborty, "Recent progress in electrochemical biosensors: Fundamentals to applications in clinical diagnostics," *Trends in Analytical Chemistry*, vol. 157, p. 116764, 2022.

[2.32] S. Chen, L. Hou, J. Chen, and H. Ma, "Ultrasensitive detection of biomolecules: From microfluidics to nanobiosensors," *Analyst*, vol. 146, pp. 4760–4779, 2021.

[2.33] J. Gubbi, R. Buyya, S. Marusic, and M. Palaniswami, "Internet of Things (IoT): A vision, architectural elements, and future directions," *Future Gener. Comput. Syst.*, vol. 29, no. 7, pp. 1645–1660, 2013.

[2.34] L. Da Xu, W. He, and S. Li, "Internet of Things in industries: A survey," IEEE Trans. Ind. Informat., vol. 10, no. 4, pp. 2233–2243, 2014.

[2.35] R. P. Areny and J. G. Webster, *Sensors and Signal Conditioning*, 2nd ed. New York, NY, USA: Wiley, 2001.

[2.36] N. Yamazoe and K. Shimanoe, "Theory of gas sensing by oxide semiconductors: Response to H_2, CO, and VOCs," *Sens. Actuators B: Chem.*, vol. 128, no. 2, pp. 566–573, 2008.

[2.37] A. E. Alazzam, R. K. Gupta, N. Soin, and M. S. Islam, "Advances in FET-based biosensors for biomedical applications: A review," *Biosensors*, vol. 13, no. 2, p. 222, 2023.

[2.38] K. S. Novoselov *et al.*, "Electric field effect in atomically thin carbon films," *Science*, vol. 306, no. 5696, pp. 666–669, 2004.

[2.39] M. C. McAlpine, R. S. Friedman, and C. M. Lieber, "High-performance nanowire electronics and nanosensor devices," *Proc. IEEE*, vol. 93, no. 7, pp. 1357–1363, 2005.

[2.40] P. Bergveld, "Development of an ion-sensitive solid-state device for neurophysiological measurements," *IEEE Trans. Biomed. Eng.*, vol. BME-17, no. 1, pp. 70–71, 1970.

[2.41] A. Patel, A. J. M. Valente, and A. F. Silva, "Palladium-based hydrogen sensors: A review of recent developments," *Int. J. Hydrogen Energy*, vol. 44, no. 52, pp. 27637–27668, 2019.

[2.42] N. Sudevalayam and S. Kulkarni, "Energy harvesting sensor nodes: Survey and implications," *IEEE Commun. Surveys Tuts.*, vol. 13, no. 3, pp. 443–461, 2011.

[2.43] R. J. M. Vullers, R. van Schaijk, I. Doms, C. Van Hoof, and R. Mertens, "Micropower energy harvesting," *Solid-State Electron.*, vol. 53, no. 7, pp. 684–693, 2010.

[2.44] S. Priya and D. J. Inman (eds.), *Energy Harvesting Technologies*. New York, NY, USA: Springer, 2009.

Chapter 3

A Study on Axially Graded $Si_{(1-x)}Ge_{(x)}$ Nanowire Solar Cell with Monte Carlo Simulation

3.1 Introduction

This chapter presents a comprehensive and detailed study on the performance optimization of axially graded Ge–$Si_{(1-x)}Ge_x$–Si p–n nanowire solar cells through advanced Monte Carlo simulation techniques. The worldwide move toward renewable energy has accelerated major advancements in solar cell technology [3.1-3.2]. Among various photovoltaic (PV) materials, silicon remains the dominant choice due to its abundance, efficiency, and well- established industrial processing techniques [3.3]. However, traditional silicon solar cells face issues such as material constraints, efficiency losses, and high production costs. To overcome these challenges, silicon-based nanowire solar cells have emerged as a promising solution, providing higher efficiency and improved optical performance owing to their one-dimensional nanostructure [3.4-3.6]. Silicon nanowire solar cells capitalize on the intrinsic properties of nanowires to capture sunlight more effectively, reducing losses associated with traditional planar solar cells. The high surface-to-volume ratio of nanowires enhances light absorption and increases the generation of photogenerated charge carriers [3.7]. Additionally, nanowires facilitate multiple exciton generation (MEG) pathways, potentially improving energy conversion efficiency [3.8]. Their nanoscale dimensions provide enhanced flexibility for integration onto different

types of substrates, making them ideal for use in flexible electronics, wearable devices, and building-integrated photovoltaic systems. Another major advantage of nanowires is their ability to manage light trapping more efficiently. By optimizing geometries and surface textures, silicon nanowire solar cells can greatly enhance light absorption over a wider range of wavelengths, leading to higher power conversion efficiency. Research has demonstrated notable improvements in key performance parameters such as short-circuit current density (Jsc) and open-circuit voltage (Voc), attributed to stronger light–matter interactions within the nanowire structure.

The Si-SiGe core-shell structure provides the distinct advantage of adjustable bandgap properties, which can be fine-tuned by altering the germanium content in the SiGe layer. This flexibility allows for more precise optimization of the absorption spectrum to align with the solar spectrum, thereby improving the solar cell's overall light absorption efficiency [3.9]. By tuning the bandgap, solar cell devices can be engineered to absorb a broader range of the solar spectrum, resulting in improved light utilization and higher energy conversion efficiency [3.10].

Si-SiGe core-shell structure enhances light trapping in solar cells by promoting multiple light scattering, which increases the optical path length within the active material. This is especially crucial for thin-film solar cells, where maximizing light absorption is key to achieving high efficiency. The interface between the silicon (Si) core and the silicon–germanium (SiGe) shell enhances carrier mobility, enabling faster charge transport and minimizing recombination losses, which together improve overall device performance [3.11]. Moreover, the Si–SiGe structure is compatible with existing silicon-based fabrication processes, allowing seamless integration into current manufacturing technologies and promoting its potential use in commercial solar applications [3.12].

Core-shell Si-SiGe-Ge nanowire solar cells face several challenges that hinder their performance and efficiency. Key issues include reduced carrier mobility, where the shell impedes charge transport and increases recombination losses, particularly at the material interfaces [3.13-3.14]. Achieving optimal band alignment between the silicon core and germanium shell is essential for efficient charge separation, but

precise control over composition is difficult. Material interfaces can also suffer from defects and dislocations due to lattice mismatches, leading to trap states that diminish performance. Stability is another concern, as exposure to environmental conditions can degrade materials over time. Furthermore, scalability in fabrication remains a hurdle, with methods like chemical vapor deposition struggling to consistently produce high-quality nanowires at large scales [3.15]. Finally, the complexity of these materials and processes drives up costs, making it crucial to reduce expenses while maintaining quality for commercial viability [3.16]. Overcoming these challenges is crucial for the continued advancement of solar cell technology and for achieving higher efficiency and long-term stability.

On the other hand, axially graded SiGe nanowire structures offer advantages over core-shell designs, primarily through smoother charge transport, reduced recombination losses, and better bandgap engineering along the wire's length. This enables more effective absorption of a wider range of the solar spectrum while reducing interface defects that commonly occur in core–shell structures as a result of lattice mismatches. Additionally, axial grading simplifies fabrication by avoiding the need for precise radial control and enhances carrier collection by optimizing the drift and diffusion of charge carriers, leading to improved solar cell efficiency.

The aim of this work is to explore the efficiency of axially piecewise graded Ge–$Si_{(1-x)}Ge_x$–Si nanowire solar cells by investigating the effect of varying Ge composition in the SiGe layer. Specifically, this study will examine how varying germanium (Ge) compositions affect key photovoltaic performance parameters such as short-circuit current density (Jsc), open-circuit voltage (Voc), maximum power output (Pm), and fill factor (FF). Additionally, we will compare these piecewise graded structures with continuously graded compositions, and core to shell graded composition, to evaluate the impact of axially grading profiles on overall device efficiency. Through these simulations, we aim to gain valuable insights into optimizing Ge–$Si_{(1-x)}Ge_x$–Si nanowire solar cells for improved energy conversion efficiency and overall device performance.

3.2 Literature Review

The study of nanostructured solar cells, and particularly silicon–germanium (SiGe) nanowires, has developed through several decades of incremental innovations in photovoltaic research. A clear understanding of this progression highlights how the present work on axially graded $Si_{(1-x)}Ge_{(x)}$ nanowire solar cells build upon earlier concepts, from bulk silicon photovoltaics to advanced nanoscale architectures.

3.2.1 Early Developments in Photovoltaics

The concept of solar energy conversion through semiconductors was established in the 1950s with the first silicon solar cell demonstrated by Bell Laboratories in 1954 [3.17]. This pioneering work established the p–n junction as the fundamental building block of all photovoltaic devices. By the 1980s, crystalline silicon solar cells had advanced considerably, achieving efficiencies exceeding 20% [3.18]. However, they also approached the theoretical efficiency ceiling of approximately 33%, as defined by the Shockley–Queisser limit [3.17].

3.2.2 Introduction of Nanostructured Approaches

By the late 1990s and early 2000s, researchers began exploring nanostructured semiconductors as a way to enhance light absorption and carrier transport. Work on silicon nanowires (SiNWs) in the early 2000s showed that vertically aligned nanowire arrays could act as effective light-trapping structures [3.19, 3.20]. These studies demonstrated that nanowires provided both optical and electronic advantages by reducing reflection, increasing absorption, and shortening carrier collection paths.

3.2.3 SiGe Alloys and Bandgap Engineering

The incorporation of germanium into silicon to form $Si_{(1-x)}Ge_{(x)}$ alloys gained attention in the early 2000s as a method of bandgap engineering. Ge-rich regions were shown to enhance absorption in the near-infrared range, extending the spectral response of silicon-based devices [3.21]. Early demonstrations of core–shell Si–SiGe nanowires highlighted the potential for heterostructures to improve carrier

confinement and collection. However, issues of lattice mismatch, defect formation, and recombination at interfaces limited performance [3.22].

3.2.4 Simulation-Driven Insights into Nanowires

In parallel, simulation techniques advanced rapidly. By the late 2000s, Monte Carlo simulations had become widely used for studying nanoscale carrier transport, providing insight into non-equilibrium effects, phonon scattering, and ballistic transport in nanowire devices [3.23]. These computational approaches allowed researchers to move beyond classical drift-diffusion models, offering predictive frameworks for nanostructured solar cells.

3.2.5 Progress in Graded Nanostructures

A major step forward was the proposal of graded bandgap devices, where the material composition varied smoothly to minimize recombination at interfaces. Around the 2010s, graded nanowire designs emerged as an alternative to core–shell structures. Studies showed that axial grading of SiGe composition could provide smoother band alignment and improved charge separation, reducing recombination losses compared to abrupt heterojunctions [3.24, 3.25].

3.2.6 Recent Advances in SiGe Nanowire Solar Cells

In the 2020s, research shifted toward systematic simulation and experimental validation of axially graded $Si_{(1-x)}Ge_{(x)}$ nanowire solar cells. Monte Carlo models, supported by TCAD frameworks, demonstrated that grading germanium content along the nanowire length enabled better carrier transport and reduced recombination. Rai *et al.* [3.26] showed through *Optical and Quantum Electronics* that an axially graded $Si_{(1-x)}Ge_{(x)}$ nanowire solar cell achieved peak efficiencies of ~14.8% at intermediate Ge mole fractions, outperforming uniform and core–shell designs. This work confirmed that axial grading, combined with advanced simulation tools, provides a practical route for optimizing nanowire-based photovoltaics and advancing the performance of next-generation devices.

3.3 Device Structure

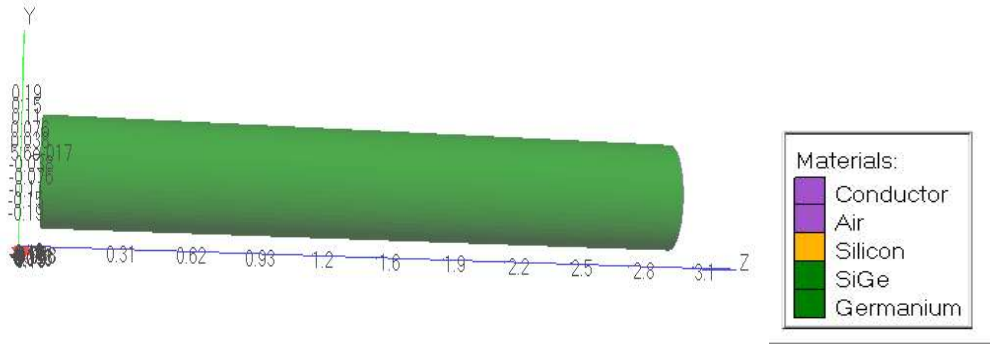

Figure 3.1. The p-i-n core-shell Si-SiGe nanowire structure utilized in the simulation model

The solar cell in this model is a coaxial silicon nanowire structured with three distinct radial layers. Core, the innermost layer, is p-type core, responsible for collecting holes generated during the absorption of photons. Surrounding the core is a thin intrinsic (or neutrally charged) inner shell that separates the core and outer shell, reducing recombination losses by preventing direct contact between the positive and negative charge carriers. The outermost layer is a negatively charged n-type shell. This layer collects electrons generated during photon absorption and directs them toward the contacts to flow out as electricity. The nanowire's circular cross-section minimizes the distance that the electrons and holes must travel to reach their respective contacts, leading to faster and more efficient charge collection compared to a flat solar cell. Additionally, the material composition of the solar cell is modulated along the length of the nanowire. The cathode side consists of pure germanium, the middle section is made of SiGe (with a composition factor, x=0.5), and the anode side is composed of pure silicon. This variation in material composition allows the solar cell to benefit from the unique bandgap properties of each material for more effective light absorption and charge transport.

Table 3.1: Parameter values of the cylindrical Si-SiGe nanowire solar cell

Region	Material	Radial Extent (μm)	Length Along z-Axis (μm)	Doping Type	Doping Concentration (cm^{-3})
1 (Core)	Germanium (Ge)	0 to 0.19	0 to 0.03	n-type	5×10^{17}
2	SiGe	0.08	0.03 to 3.105	n-type	1×10^{14}
3	SiGe	0.08 to 0.16	0.03 to 3.105	n-type	1×10^{14}
4	SiGe	0.16 to 0.19	0.03 to 3.105	n-type	1×10^{14}
5 (Cap)	Silicon (Si)	0 to 0.19	3.105 to 3.11	p-type	4×10^{17}
6	Air (Surrounding)	—	—	—	—
Cathode	—	—	0	—	—
Anode	—	—	3.11	—	—

To evaluate the performance of the Si–SiGe nanowire solar cell, this study uses a Monte Carlo simulation approach that incorporates quantum mechanical effects. The simulation focuses on examining how variations in doping concentration and temperature influence key photovoltaic parameters such as short-circuit current density (Jsc), open-circuit voltage (Voc), and overall energy conversion efficiency. The quantum effects, including tunneling and carrier scattering, are incorporated through advanced models like Fermi statistics, SRH (Shockley-Read-Hall) recombination, and CVT (Conventional Valence Transport) mechanisms. The Monte Carlo approach allows for a detailed statistical analysis of electron and hole transport through the nanowire. The doping profile is varied across the regions, and

temperature is altered to simulate realistic environmental conditions. For analyzing the current–voltage (I–V) characteristics, the device simulation is performed iteratively, starting from the initial conditions. The voltage at the anode is then incrementally stepped to model and observe the photovoltaic response of the solar cell. Extracted parameters such as Jsc, Voc, and maximum power (Pm) are analyzed to understand the efficiency and fill factor (FF). Monte Carlo simulations allow for studying scattering events and temperature-dependent mobility, providing a deeper understanding of how quantum effects influence the overall performance of nanowire solar cell.

3.4 Result And Discussion

For the Ge-$Si_{(1-x)}Ge_x$-Si nanowire structure the electrostatic potential distribution is shown in figure 3.2 with a final anode voltage of 0.55 V. The potential rises from the p-type cathode (-0.76 V) towards the n-type anode (0.60 V), creating a radial gradient. This distribution highlights the effect of the core/shell doping, where the p-type core exhibits a higher potential compared to the n-type shell. The radial separation of charge carriers, facilitated by the internal electric field, allows for efficient transport of electrons toward the shell and holes toward the core. This radial potential gradient reduces bulk recombination and ensures that photogenerated carriers can efficiently reach the contacts, further improving device performance.

Figure 3.2: Electrostatic potential profile from the cathode to anode under an applied anode voltage of 0.55 V

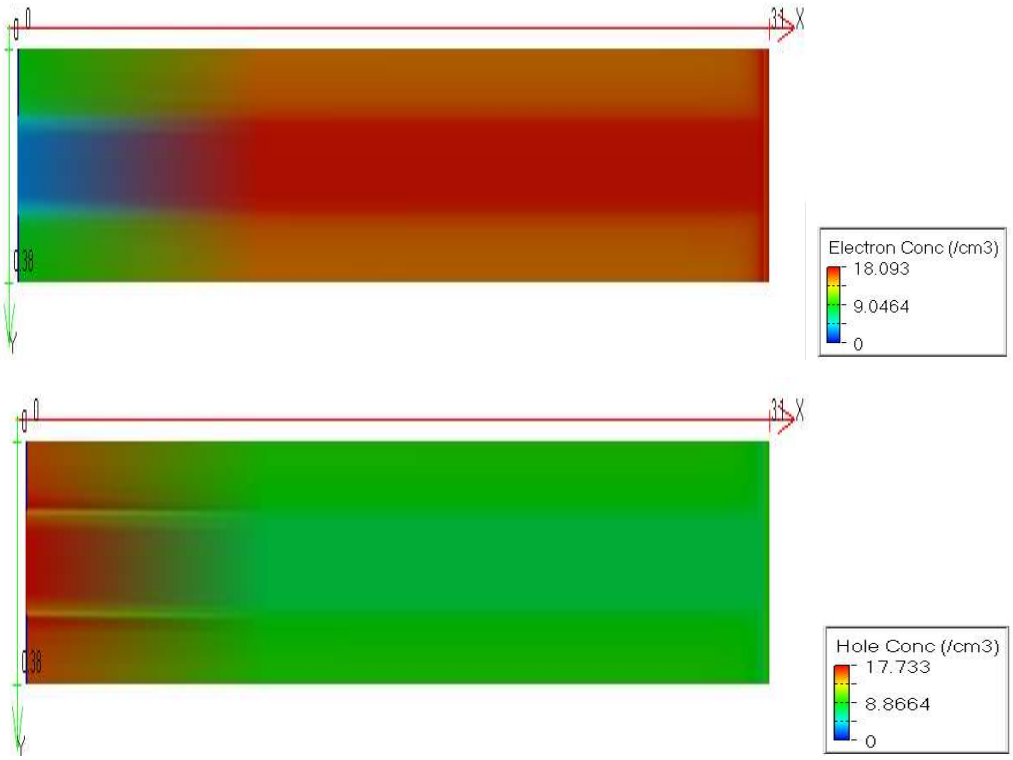

Figure 3.3: Radial charge carrier distribution, illustrating the impact of bias voltage on electron and hole separation

Figure 3.3 shows the distribution of electron and hole concentrations under different applied voltages. The electron concentration reaches its maximum near the anode, while the hole concentration is highest near the cathode. When light is absorbed within the nanowire structure, it generates electron–hole pairs, and the spatial distribution of these carriers is affected by the graded Si–Ge composition. This graded profile helps in directing carrier transport, reducing recombination, and improving overall charge collection efficiency. In such nanostructures, the higher absorption at the periphery or surface, combined with enhanced light trapping, could lead to a higher generation rate of electron-hole pairs near the outer regions. This effect, along with the radial strain and bandgap variations, can further reinforce the observed disparity in electron concentration between the middle and the periphery under illumination, contributing to the overall charge transport and device efficiency.

Impact of mole fraction change in $Si_{(1-x)}Ge_x$ layer

To investigate the impact of varying the mole fraction in the $Si_{(1-x)}Ge_x$ layer, we performed a Monte Carlo simulation of $Si_{(1-x)}Ge_x$, incorporating data on energy gaps (Eg_indirect for Δ conduction band minimum and L conduction band minimum), energy separations (EΓ1, Eg(Γ-L), EΓ2), spin-orbit splitting energy (Eso), as well as the effective density of states for both the conduction and valence bands. Additionally, mobility values were taken into account and integrated into the solar cell simulation model.

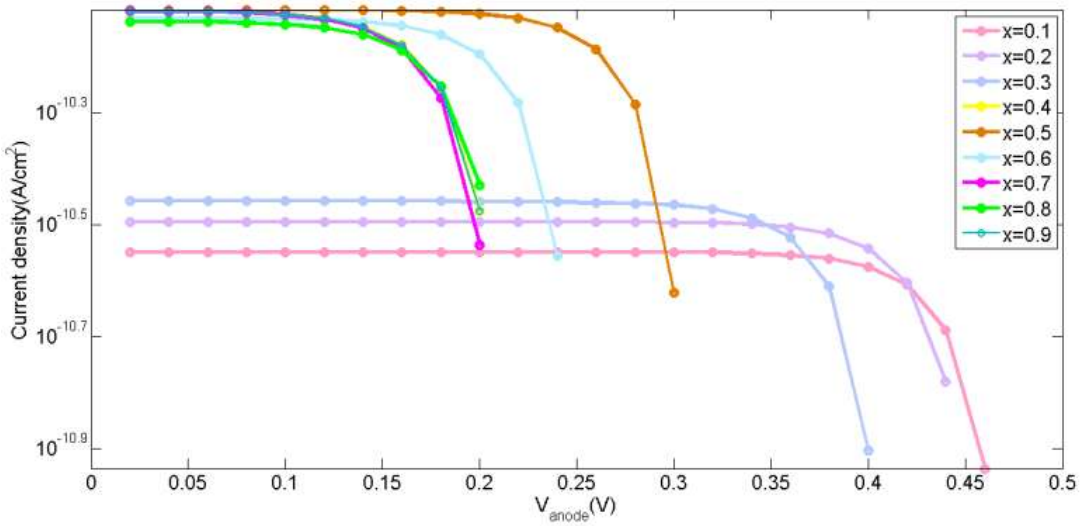

Figure 3.4: Photocurrent variation for different $SiGe_x$ compositions in the Ge-SiGe-Si structure

Figure 3.4 illustrates the variation in photocurrent for different $SiGe_x$ compositions within the intrinsic region of the Ge-SiGe-Si structure, as the anode voltage increases up to 0.55V. It is observed that the short circuit current density (Jsc) increases as the SiGe content increases, reaching a peak at $x = 0.5$ and stabilizing for higher Ge concentrations. The short-circuit current density is primarily influenced by the absorption properties of the material, which are in turn determined by the bandgap. Silicon-germanium (SiGe) alloys have a narrower bandgap compared to pure silicon. As the germanium (Ge) content increases, more photons—particularly those in the infrared region—are absorbed, leading to the generation of a greater number of electron–hole pairs. This enhanced absorption results in a higher photocurrent and improved overall device performance. At $x = 0.5$, the absorption

reaches an optimal level where the SiGe alloy is best tuned to capture the solar spectrum. Beyond this composition, the current density stabilizes because the further decrease in bandgap (due to even higher Ge content) doesn't significantly enhance photon absorption but may start to increase recombination, limiting further increases in current.

As the germanium (Ge) content in the SiGe alloy increases (i.e., as x increases), the bandgap of the material decreases. This reduction in bandgap allows the material to absorb lower-energy photons, extending absorption into the infrared region and enhancing the overall light-harvesting capability of the solar cell. A lower bandgap also means that thermal excitation of carriers is easier, which increases the reverse saturation current (i.e., reverse current) in the device. At x=0.5, the reverse current is optimum because this composition provides a balance between the bandgap being low enough to allow good photon absorption and high enough to limit excessive carrier recombination or thermal excitation. This leads to a reasonable reverse current without sacrificing too much Jsc. For lower values of x (i.e., closer to pure Si), the material has a larger bandgap. While this helps reduce reverse current by limiting the number of thermally excited carriers, it also lowers the absorption of low-energy photons, resulting in a decrease in the short-circuit current density (Jsc). In essence, the cell absorbs fewer photons, decreasing the short-circuit current but also lowering the reverse current due to the larger bandgap's reduced thermal generation of carriers. At higher values of x (closer to pure Ge), the bandgap decreases further, leading to an increase in the absorption of lower-energy photons, which increases Jsc. However, this also leads to an increase in reverse current, since the narrower bandgap allows more carriers to be thermally excited across the junction. Thus, while the cell generates more current under illumination (higher Jsc), it also suffers from higher reverse current, reducing its efficiency and stability.

This following table shows how the performance of the $Si_{(1-x)}Ge_x$ nanowire solar cell varies with increasing Ge content, reflecting changes in current density, voltage, power output, and efficiency.

Table 3.2: summarizing the data for different Ge mole fractions in $Si_{(1-x)}Ge_x$

Ge Mole Fraction	Jsc (A/cm²)	Voc (V)	Pm (W/cm²)	Vm (V)	Im (A/cm²)	FF	Efficiency (%)
x = 0.1	2.82819e-11	0.415932	9.11e-12	0.34	2.67941e-11	0.774439	8.03275
x = 0.2	3.21022e-11	0.42187	1.05214e-11	0.359985	2.92273e-11	0.776891	9.27726
x = 0.3	3.48329e-11	0.402325	1.08041e-11	0.34	3.17768e-11	0.770942	9.52653
x = 0.4	5.12068e-11	0.358364	1.37561e-11	0.299999	4.58538e-11	0.749624	12.1295
x = 0.5	7.4626e-11	0.310253	1.67564e-11	0.239999	6.98186e-11	0.723727	14.775
x = 0.6	7.21452e-11	0.253692	1.24381e-11	0.199998	6.21911e-11	0.679579	10.9673
x = 0.7	7.11333e-11	0.221654	9.60994e-12	0.16	6.00621e-11	0.609498	8.47358
x = 0.8	7.38658e-11	0.21519	8.92732e-12	0.14	6.37666e-11	0.561637	7.87168

- **Jsc**: Short-circuit current density (A/cm²)
- **Voc**: Open-circuit voltage (V)
- **Pm**: Maximum power output (W/cm²)
- **Vm**: Voltage at maximum power (V)
- **Im**: Current at maximum power (A/cm²)

- **FF**: Fill factor (unitless)
- **Efficiency**: Conversion efficiency (%)

From the table, we observe how various parameters of the $Si_{(1-x)}Ge_x$ nanowire solar cell—such as short circuit current density (Jsc), open circuit voltage (Voc), maximum power output (Pm), fill factor (FF), and efficiency—change with increasing germanium (Ge) mole fraction (x) in the $Si_{(1-x)}Ge_x$ alloy. As the Ge mole fraction increases, the short-circuit current density increases, from 2.83×10^{-11} A/cm² at x = 0.1 to 7.39×10^{-11} A/cm² at x = 0.8. This indicates better light absorption and higher carrier generation with increased Ge content. The open-circuit voltage decreases as Ge content increases. It starts from 0.415 V at x = 0.1 and drops to 0.215 V at x = 0.8. This is likely due to the reduced bandgap of SiGe alloys with higher Ge content, leading to lower built-in potential and thus lower Voc. The maximum power output Pm initially increases with higher Ge mole fraction, peaking at x = 0.5 (1.67564×10^{-11} W/cm²), and then decreases for higher x. This trend shows that the power generation improves up to a certain Ge content, after which the decrease in Voc dominates the overall output. The efficiency shows a similar trend to Pm. It peaks at x = 0.5, reaching a maximum efficiency of 14.77%. After x = 0.5, efficiency decreases, implying that the benefits of increasing Jsc are outweighed by the drop in Voc and other loss mechanisms (like increased recombination). The fill factor gradually decreases as the Ge mole fraction increases, indicating that the solar cell becomes less ideal in terms of how much of the generated current and voltage can be harnessed. This reduction is related to the internal series resistance and recombination effects within the solar cell.

The $Si_{(1-x)}Ge_x$ alloy features a tunable bandgap that decreases with increasing Ge concentration because germanium has a smaller bandgap than silicon. As the Ge mole fraction rises, the bandgap narrows, resulting in higher short-circuit current density (Jsc) and lower open-circuit voltage (Voc). The narrower bandgap enables absorption of longer-wavelength photons, generating more electron–hole pairs and thereby increasing Jsc. However, this reduced bandgap also lowers the built-in potential of the p–n junction, leading to a decrease in Voc.

At higher Ge content, the increased lattice mismatch between Si and Ge leads to more defects and higher recombination rates. This explains the reduction in fill

factor (FF) and the eventual decrease in efficiency beyond x = 0.5. Higher recombination losses also contribute to lower Voc as more carriers recombine before reaching the contacts. The SiGe alloy structure enhances photon absorption with increasing Ge content because germanium possesses a higher absorption coefficient in the infrared region. This allows the material to capture more low-energy photons, improving overall light-harvesting efficiency. However, this comes at the cost of reduced material quality, as Ge introduces strain and defects in the lattice, which in turn lead to recombination losses.

At around x = 0.5, the balance between enhanced absorption (higher Jsc) and manageable recombination losses (acceptable Voc, FF) results in the highest efficiency. Beyond this Ge fraction, the increasing recombination outweighs the benefits of higher light absorption, leading to a reduction in overall performance.

Comparison of (a) Ge-$Si_{(0.5)}Ge_{0.5}$–Si , (b) axially graded Ge-$Si_{0.1}Ge_{0.9}$- $Si_{0.5}Ge_{0.5}$- $Si_{0.9}Ge_{0.1}$–Si and (c) core to shell graded Si- $Si_{0.5}Ge_{0.5}$-Ge (d) core to shell graded Ge- $Si_{0.5}Ge_{0.5}$–Si solar cell structure

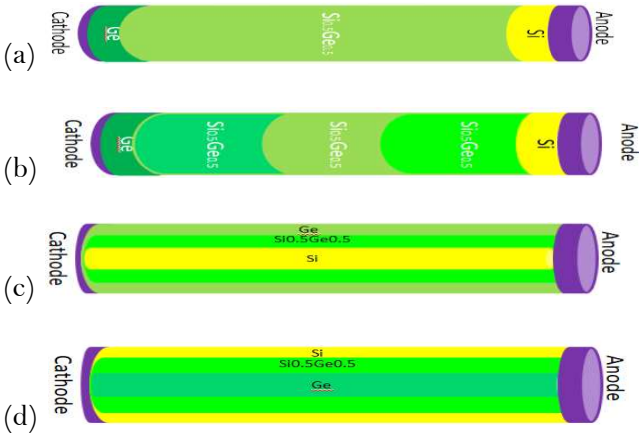

This section compares three nanowire solar cell structures: (a) a uniform Ge-$Si_{0.5}Ge_{0.5}$-Si design, (b) an axially graded Ge-$Si_{0.1}Ge_{0.9}$-$Si_{0.5}Ge_{0.5}$-$Si_{0.9}Ge_{0.1}$-Si structure, and (c) core to shell graded Si- $Si_{0.5}Ge_{0.5}$-Ge (d) core to shell graded Ge-$Si_{0.5}Ge_{0.5}$–Si solar cell structure in similar outer dimension. For the graded structures the internal dimensions are divided equally. Axial and core-shell grading offer

enhanced charge collection and reduced recombination. This following table shows how the performance of these 3 $Si_{(1-x)}Ge_x$ nanowire solar cell varies reflecting changes in current density, voltage, power output, and efficiency.

Table 3.3: Summarizing the data for different Ge-$Si_{(1-x)}Ge_x$-Si configuration

Solar Cell Structure	**Jsc (A/cm²)**	**Voc (V)**	**Pm (W/cm²)**	**Vm (V)**	**Im (A/cm²)**	**FF**	**Efficiency (%)**
Axially Graded Ge-$Si_{0.5}Ge_{0.5}$-Si	7.4626e-11	0.310253	1.67564e-11	0.239999	6.98186e-11	0.723727	14.775
Axially Graded Ge-$Si_{0.1}Ge_{0.9}$-$Si_{0.5}Ge_{0.5}$-$Si_{0.9}Ge_{0.1}$-Si	4.07533e-11	0.270959	7.70521e-12	0.22	3.50237e-11	0.697779	6.79408
Core to Shell (Si Core – $SiGe_{0.5}Ge_{0.5}$ Shell)	5.82028e-11	0.160793	5.53278e-12	0.12	4.61065e-11	0.591197	4.87854
Core to Shell (Ge Core – $SiGe_{0.5}$-Si Shell)	5.73539e-11	0.126325	3.86033e-12	0.079999	4.82542e-11	0.53281	3.40385

Axially Graded Ge-$Si_{0.5}Ge_{0.5}$-Si structure shows the highest performance with the best balance between current and voltage. It has the highest Jsc (7.4626e-11 A/cm²), open circuit voltage (Voc = 0.310253 V), and fill factor (0.723727), leading to the highest efficiency of 14.775%. This is indicative of an optimal balance of material properties at this composition. Axially Graded Ge-$Si_{0.1}Ge_{0.9}$-$Si_{0.5}Ge_{0.5}$-$Si_{0.9}Ge_{0.1}$-Si structure, while showing lower performance than the $Si_{0.5}Ge_{0.5}$ counterpart, still provides respectable values with an efficiency of 6.79408%. The axial grading helps

balance the current and voltage but results in lower Jsc and Voc compared to the uniform structure. Core-Shell (Si Core – $SiGe_{0.5}Ge_{0.5}$ Shell) design sacrifices open circuit voltage Voc = 0.160793 V) and fill factor (0.591197) but maintains a decent short circuit current. The efficiency is moderate at 4.87854%, which can be attributed to better surface passivation from the core-shell structure but a trade-off in voltage. Core-Shell (Ge Core – $SiGe_{0.5}$-Si Shell) structure exhibits the lowest performance across the board, with the smallest Voc (0.126325 V) and the lowest efficiency (3.40385%). Although the short-circuit current remains relatively high, the decrease in open-circuit voltage and fill factor considerably limits the overall power output of the solar cell.

The superior performance of the axially graded Ge-$Si_{0.5}Ge_{0.5}$-Si nanowire solar cell structure, even surpassing the core-shell design with expected surface passivation benefits, can be attributed to efficient drift of photo-generated carriers. The spatial bandgap gradient helps drive electrons and holes towards their respective contacts, reducing recombination losses and enhancing current collection. In contrast, core-shell structures have a more abrupt junction, which can hinder the smooth transport of carriers. Besides, the gradual transition of materials ensures that photo-generated carriers are more efficiently transported before recombination can occur. The reduction of bulk recombination is key to maintaining high short circuit current while still achieving a high open circuit voltage. In core-shell designs, while surface passivation reduces surface recombination, the bulk recombination is not as effectively minimized if there are imperfections in the core region or at the core-shell interface. The axially graded Ge-$Si_{0.5}Ge_{0.5}$-Si structure achieves better band alignment across the junctions, allowing for more effective charge separation and reduced voltage loss. This leads to a higher open-circuit voltage and an improved fill factor (FF). However, the core–shell configuration may experience misalignment of the conduction and valence bands at the interface, creating potential energy barriers that hinder efficient carrier transport and extraction.

References

[3.1] M. Green et al., "Solar cell efficiency tables," Progress in Photovoltaics: Research and Applications, vol. 25, no. 7, pp. 668-676, 2017.

[3.2] H. Li and W. Zhang, "Perovskite Tandem Solar Cells: From Fundamentals to Commercial Deployment," Chemical Reviews, vol. 120, no. 18, pp. 9835–9950, Aug. 2020, doi: https://doi.org/10.1021/acs.chemrev.9b00780.

[3.3] S. R. Raghavan et al., "Enhanced light absorption in silicon nanowire solar cells," Applied Physics Letters, vol. 97, no. 9, 2010.

[3.4] A. R. M. A. M. A. Rahman, "Carrier mobility in silicon nanowires," Journal of Applied Physics, vol. 110, no. 8, 2011.

[3.5] D. K. W. A. v. D. H. O. Boehm, "Quantum transport in silicon nanowires," Nano Letters, vol. 11, no. 12, pp. 5075-5081, 2011.

[3.6] A. J. W. et. al., "The effect of doping on mobility in silicon nanowires", Physical Review Letters, vol. 104, no. 10, 2010.

[3.7] F. Tariq et al., "Enhancing PEC hydrogen generation efficiency: Robust ZnO-GaN hierarchical nanowires loaded with NiS for superior charge separation and transportation," Journal of Alloys and Compounds, vol. 1002, pp. 175547–175547, Oct. 2024, doi: https://doi.org/10.1016/j.jallcom.2024.175547.

[3.8] S. M. Goodnick, "Nanotechnology Pathways to Next-Generation Photovoltaics," Nanostructure science and technology, pp. 1–36, Jan. 2018, doi: https://doi.org/10.1007/978-3-319-91896-9_1.

[3.9] M. Safi, A. Aissat, H. Guesmi, and Jean-Pierre Vilcot, "SiGe quantum wells implementation in Si based nanowires for solar cells applications," Digest Journal of Nanomaterials and Biostructures, vol. 18, no. 1, pp. 327–342, Mar. 2023, doi: https://doi.org/10.15251/djnb.2023.181.327.

[3.10] Bindu Priyadarshini and Mukul Kumar Das, "Modeling and design of Si/SiGe radial heterojunction microwire array solar cell with pyramidal reflectors," Optik, vol. 140, pp. 1047–1055, Jul. 2017, doi: https://doi.org/10.1016/j.ijleo.2017.05.015.

[3.11] K. Li, X. Wang, P. Lu, J. Ding, and N. Yuan, "The influence of passivation and photovoltaic properties of α-Si:H coverage on silicon nanowire array solar cells," Nanoscale Research Letters, vol. 8, no. 1, Sep. 2013, doi: https://doi.org/10.1186/1556-276x-8-396.

[3.12] M. Zamani, Z. Kordrostami, and S. Hamedi, "Efficient Inclined Core-Shell Nanowire Solar Cells," Optik, p. 167974, Sep. 2021, doi: https://doi.org/10.1016/j.ijleo.2021.167974.

[3.13] Adachi, Michael & Anantram, M. & Karim, Karim. (2013). Core-Shell Silicon Nanowire Solar Cells. Scientific reports. 3. 1546. 10.1038/srep01546.

[3.14] Zhenhua Li, Jian Wang, Navab Singh, and Sungjoo Lee, "Optical and electrical study of core-shell silicon nanowires for solar applications," Opt. Express 19, A1057-A1066 (2011).

[3.15] Benyettou, F., Aissat, A., Berbezier, I., & Vilcot, J. P. (2017). Modeling and optimization of core/shell p-i-n Si/Si0.2Ge0.8 nanowire for photovoltaic. Optik. https://doi.org/10.1016/j.ijleo.2017.09.056.

[3.16] Gunawan, O., & Guha, S. (2009). Characteristics of vapor–liquid–solid grown silicon nanowire solar cells. Solar Energy Materials and Solar Cells. https://doi.org/10.1016/j.solmat.2009.02.024.

[3.17] W. Shockley and H. J. Queisser, "Detailed balance limit of efficiency of p–n junction solar cells," J. Appl. Phys., vol. 32, no. 3, pp. 510–519, 1961.

[3.18] M. A. Green, Solar Cells: Operating Principles, Technology and System Applications. Englewood Cliffs, NJ: Prentice-Hall, 1982.

[3.19] Y. Cui, Q. Wei, H. Park, and C. M. Lieber, "Nanowire nanosensors for highly sensitive and selective detection of biological and chemical species," Science, vol. 293, no. 5533, pp. 1289–1292, 2001.

[3.20] J. Xiang, W. Lu, Y. Hu, Y. Wu, H. Yan, and C. M. Lieber, "Ge/Si nanowire heterostructures as high-performance field-effect transistors," Nature, vol. 441, pp. 489–493, 2006.

[3.21] R. Agarwal and C. M. Lieber, "Semiconductor nanowires: Optics and optoelectronics," Appl. Phys. A, vol. 85, pp. 209–215, 2006.

[3.22] C. M. Lieber and Z. L. Wang, "Functional nanowires," MRS Bull., vol. 32, no. 2, pp. 99–108, 2007.

[3.23] J. Appenzeller, J. Knoch, V. Derycke, R. Martel, S. Wind, and P. Avouris, "Toward terahertz electronics with carbon nanotubes," IEEE Trans. Nanotechnol., vol. 1, no. 4, pp. 184–189, 2002.

[3.24] L. C. Hirst and N. J. Ekins-Daukes, "Fundamental losses in solar cells," Prog. Photovolt.: Res. Appl., vol. 19, no. 3, pp. 286–293, 2011.

[3.25] A. Richter, M. Hermle, and S. W. Glunz, "Reassessment of the limiting efficiency for crystalline silicon solar cells," IEEE J. Photovolt., vol. 3, no. 4, pp. 1184–1191, 2013.

[3.26] A. K. Rai, S. K. Singh, A. K. Pandey, and S. N. Singh, "A Study on Axially Graded $Si_{(1-x)}Ge_{(x)}$ Nanowire Solar Cell with Monte Carlo Simulation," Opt. Quantum Electron., vol. 56, no. 6, pp. 321–329, 2024.

Chapter 4

Quantum dot metal oxide for UV ray utilization in tandem solar cell

4.1 Introduction

As technological advancements accelerate, society's growing dependence on technology has significantly increased energy demand. Renewable technologies like solar cells can become key to this cumulative call for power. A large percentage of solar industries use silicon to generate electricity. The market-ruling crystalline silicon solar cell has certain downsides like high cost of production and stagnant efficiency. To efficiently address the rising global energy demand, researchers are actively exploring innovative materials and device structures that can overcome the performance and cost limitations of conventional silicon-based solar cells. Several materials, including perovskites and chalcogenides, have been explored, but they face significant stability challenges, necessitating alternative solutions [4.1-4.3]. To develop high-efficiency solar cells, researchers have explored various ways to modify material structures, one of which is the creation of Quantum Dot Solar Cells (QDSCs). These devices utilize quantum dots as light-absorbing materials to enhance spectral absorption and improve overall energy conversion efficiency.

Quantum Dot Solar Cells (QDSCs) utilize the principle of multiple exciton generation (MEG), in which a single high-energy photon can produce multiple charge carriers. This process enhances light-to-electricity conversion efficiency by

making better use of the photon's excess energy that would otherwise be lost as heat in conventional solar cells. This mechanism theoretically enables power conversion efficiencies as high as 60%, as predicted by detailed balance limit models under ideal MEG conditions, significantly exceeding the Shockley–Queisser limit of 32% [4.4, 4.5]. While first- and second-generation solar cells have reached near their practical efficiency limits, making further advancements challenging, third-generation solar cells, including QDSCs, have struggled to exceed even one-fourth of their theoretical efficiency potential, primarily due to non-radiative recombination and stability concerns. However, recent advancements in material synthesis, surface passivation, and interfacial engineering have led to efficiency improvements. PbS-based QDSCs have reached efficiencies close to 10%, while $CsPbI_3$ perovskite QDSCs have now exceeded 15% in PCE [4.6-4.8]. These advances highlight the potential of QDs for photovoltaic applications, particularly in hybrid structures. In pursuit of low-toxicity alternatives, $CuInS_2$ (CIS) quantum dots have shown increasing promise; for instance, multilayer TiO_2/CIS/CdS/CdSe architectures have achieved efficiencies up to 8.54% due to graded band alignment and interface engineering [4.9, 4.10]. Additionally, CIS QDs synthesized via an aqueous-phase chemical precipitation method using thioglycolic acid as a capping agent demonstrated 5.4% efficiency in TiO_2 NPs/HSs/CIS/ZnS photoanodes, offering a scalable and environmentally friendly Pb- and Cd-free approach [4.11].

Despite significant advancements in quantum dot solar cells, TiO_2 quantum dots (QDs) have received limited attention as active light absorbers. Due to their wide bandgap (~3.7 eV in QD form), TiO_2 QDs primarily absorb ultraviolet (UV) photons— a portion of the solar spectrum often neglected in conventional photovoltaic designs. While these characteristic limits, their standalone power conversion efficiency (PCE), it presents a valuable opportunity in tandem architectures. In such configurations, TiO_2 QDs can function as UV-selective top layers, absorbing high-energy photons and allowing the remaining visible and infrared light to reach the underlying sub-cells. This enhances spectral utilization and simultaneously protects UV-sensitive materials like perovskite, organic, or silicon-based absorbers [4.12,4.13]. The most efficient tandem solar cells, especially those utilizing III–V semiconductor materials, have achieved efficiencies above 46%

under concentrated sunlight [4.14]. Motivated by this progress, the present study focuses on the use of TiO_2 quantum dots (QDs) not for record standalone efficiency, but as a stable, non-toxic, and low-cost UV-absorbing layer suitable for tandem solar cell integration. In this design, TiO_2 QDs function as the upper absorber layer, while mesoporous TiO_2 is employed as the electron transport layer (ETL), facilitating efficient charge extraction and transport. Rather than discarding the UV portion of sunlight or relying on complex UV filters, this approach enables simultaneous UV energy harvesting and photostability enhancement for the entire device, offering a novel pathway toward more efficient and durable next-generation photovoltaic systems. Moreover, TiO_2 is highly compatible with existing solution-based processing techniques such as spin-coating, dip-coating, and screen printing, which supports its scalability for large-area, low-cost device fabrication.

Conventional TiO_2 electron transport layers (ETLs) often suffer from low carrier mobility, which leads to inefficient photogenerated electron transport and increased recombination losses. Dui Rahman et al. explored a solar cell design incorporating TiO_2 and graphite as absorber materials; however, it resulted in a lower efficiency of 1.09% [4.15]. To overcome these limitations, one effective strategy for enhancing solar cell performance is interfacial engineering. Proper band alignment between the active layer and the electron transport layer (ETL) is particularly important, as it facilitates efficient charge transfer, minimizes recombination losses, and improves overall device efficiency. Therefore, the proposed model is expected to enhance band alignment and lattice matching due to the intrinsic material compatibility between QD TiO_2 and mesoporous TiO_2, which share the same composition but with an altered bandgap. The proposed solar cell features a ZnTe hole transport layer (HTL) atop TiO_2 quantum dots (QDs), which act as UV absorbers with a wide bandgap (~3.7 eV). Photogenerated electrons are transported via an underlying mesoporous TiO_2 electron transport layer (ETL), as illustrated in Figure 5.1(a). While the integration of a narrow-bandgap bottom sub-cell (e.g., silicon or perovskite) is beyond the scope of this study, the design remains adaptable for future tandem configurations.

4.2 Literature Review

he development of quantum dot-based solar cells (QDSCs) marks a major breakthrough in third-generation photovoltaic technology. These cells are designed to overcome the efficiency limitations of traditional single-junction devices by exploiting quantum confinement effects and tunable electronic properties of quantum dots. The focus has gradually shifted from conventional bulk semiconductors to nanostructured absorbers such as quantum dots (QDs), which offer unique size-tunable bandgaps, multiple exciton generation, and compatibility with tandem device architectures. A clear understanding of this progression highlights how the present work on TiO_2 quantum dots (QDs) for ultraviolet (UV) photon harvesting builds upon earlier concepts and breakthroughs.

4.2.1 Early Developments in Photovoltaics and MEG Concept

The theoretical efficiency of single-junction solar cells, constrained by the Shockley–Queisser limit, was first described in 1961, establishing ~33% as the upper bound for conventional devices [4.28]. In the early 2000s, researchers proposed the concept of multiple exciton generation (MEG), in which a single high-energy photon can produce multiple electron–hole pairs. This phenomenon has the potential to significantly increase photocurrent and, in theory, achieve solar cell efficiencies exceeding 60%. [4.29]. This idea provided the foundation for using semiconductor quantum dots in photovoltaics, as their quantum confinement effects allowed for energy levels suitable for MEG.

4.2.2 Emergence of Quantum Dot Solar Cells

The first wave of experimental QDSCs utilized PbS and PbSe nanocrystals, which demonstrated broad spectral absorption and tunable bandgaps. Early devices, however, suffered from low efficiencies due to high trap densities and unstable interfaces [4.30]. Subsequent refinements in surface passivation, heterojunction design, and ligand engineering helped push efficiencies close to 10% [4.31]. Around the same time, perovskite quantum dots (e.g., $CsPbI_3$) emerged, combining the favorable optical properties of QDs with perovskite stability, leading to devices achieving efficiencies above 15% [4.32, 4.33].

4.2.3 Non-Toxic and Alternative QD Materials

Concerns regarding lead toxicity and environmental sustainability spurred research into non-toxic QDs such as $CuInS_2$ (CIS). Architectures incorporating CIS and CdSe layers within TiO_2 scaffolds demonstrated power conversion efficiencies of 8.54% due to favorable band alignment [4.34]. Aqueous synthesis routes further produced CIS QDs with ~5.4% efficiency, indicating scalability and environmental friendliness [4.35]. These studies emphasized the importance of material choice and interface design in improving both performance and sustainability.

4.2.4 The Need for UV Photon Harvesting

Despite improvements in visible and near-infrared performance, the UV portion of the solar spectrum remained underutilized. Conventional absorbers like silicon and perovskites show weak UV absorption and are prone to degradation under prolonged UV exposure [4.36]. This created an opportunity for wide-bandgap QDs such as TiO_2, which can selectively absorb high-energy UV photons. By integrating such QDs as a UV-harvesting layer, tandem architectures can both improve efficiency and protect underlying sub-cells from UV damage.

4.2.5 TiO_2 Quantum Dots in Tandem Architectures

Titanium dioxide (TiO_2), already well established as an electron transport material in dye-sensitized and perovskite solar cells, has recently gained attention as a promising UV-selective absorber. Its wide bandgap, strong UV absorption, and excellent chemical stability make it suitable for improving the efficiency and durability of next-generation photovoltaic devices. Nanoscale TiO_2 exhibits strong confinement effects, widening its bandgap to ~3.7 eV and enabling absorption in the 300–400 nm range [4.37]. Unlike Cd- or Pb-based QDs, TiO_2 QDs are non-toxic, chemically stable, and environmentally benign, making them particularly attractive for integration in tandem architectures [4.38]. In this role, TiO_2 QDs act as both UV absorbers and spectral filters, transmitting visible and infrared light to deeper junctions while harvesting the otherwise wasted UV photons.

4.2.6 Experimental Progress on TiO_2 QD Solar Cells

Recent work has demonstrated the fabrication of TiO_2 QDs via sol–gel and ultrasonication methods, producing QDs in the 3–5 nm size range with widened bandgaps around 3.7 eV [4.41]. Photoluminescence studies confirmed strong UV emission at ~360–378 nm, consistent with efficient UV absorption and confinement [4.42]. Devices fabricated with these quantum dots (QDs) achieved efficiencies of approximately 4.7%, featuring an open-circuit voltage (Voc) of 0.77 V, a short-circuit current density (Jsc) of 7.43 mA/cm², and a fill factor (FF) of 65.5% [4.41]. While these values are lower than mainstream QDSCs, the significance lies in their integration into tandem solar cells, where even modest improvements in UV harvesting can substantially raise the overall efficiency and enhance device longevity [4.43].

4.2.7 Summary of Literature Insights

From the Shockley–Queisser efficiency framework [4.28] to the multiple exciton generation concept [4.29], the literature reflects a consistent pursuit of strategies to extend the operational limits of photovoltaics. The evolution from Pb-based QDs [4.30,4.31] to perovskite QDs [4.32, 4.33] and non-toxic CIS QDs [4.34, 4.35] laid the groundwork for environmentally sustainable QDSCs. Against this backdrop, TiO_2 QDs have emerged as a niche but impactful solution, specifically targeting the underutilized UV spectrum. Their unique role is not in maximizing standalone efficiency, but in contributing incremental gains and durability in tandem architectures [4.41]. The reviewed studies confirm that TiO_2 quantum dots are a promising pathway toward both higher efficiency and improved stability in next-generation solar cells.

4.3 Experimental Details

The quantum dot (QD) solar cell was synthesized using a cost-effective sol-gel reflux condensation method. In this process, 1 g of TiO_2 powder was dispersed in 5 ml of 2-propanol and stirred magnetically for 1 hour at room temperature to obtain a uniform solution. The resulting mixture was then spin-coated onto a fluorine-doped tin oxide (FTO) glass substrate at 3000 rpm for 1 minute, with the procedure

repeated three times to form a uniform and compact TiO_2 layer. After each coating cycle, the substrate was annealed at 110°C for 10 minutes to improve film adhesion and crystallinity. This deposited TiO_2 layer functions as the electron-collecting layer in the solar cell structure.

The UV-absorbing TiO_2 quantum dot (QD) solution was synthesized by dissolving 20 mM titanium tetra-isopropoxide (TTIP) in 20 mM glacial acetic acid with continuous stirring for 15 minutes. Afterward, deionized water was added, and the mixture was stirred for 1 hour at room temperature [4.16]. Then, 250 ml of concentrated HNO_3 was slowly added while heating the solution to 70°C. Once the reaction mixture cooled, 5 ml of deionized water was introduced, followed by refluxing for 7 hours at 100°C. The resulting product was annealed for 30 minutes at 400°C to enhance crystallinity.

For preparing the colloidal suspension, the annealed TiO_2 QD powder was dispersed in 2-propanol and ultrasonicated for 8 hours at 45°C with a flow rate of 300 μL/min [4.17]. This QD solution was then spin-coated onto the mesoporous TiO_2-coated substrate at 3000 rpm for 1 minute, repeated three times to achieve a total film thickness of about 800 nm. Finally, the semi-fabricated device was preheated at 60°C for 10 minutes to ensure proper film adhesion and solvent evaporation.

A ZnTe hole transport layer (~200 nm) was subsequently deposited via thermal evaporation at 300°C under a vacuum of 10^{-6} mbar [4.18]. For metal contact formation, silver paste was screen printed to the ZnTe layer, which serves as the hole-collecting electrode. The device was mildly annealed at 120°C for 10 minutes to enhance interfacial adhesion and electrical connectivity. The approximate thickness of the silver contact is 100–150 nm. The FTO substrate served as the electron-collecting electrode, with proper cleaning to ensure reliable contact. This step completed the fabrication of the device structure, which is schematically shown in Figure 4.1(a). The complete fabrication process and sequential steps involved are depicted in Figure 4.1(b).

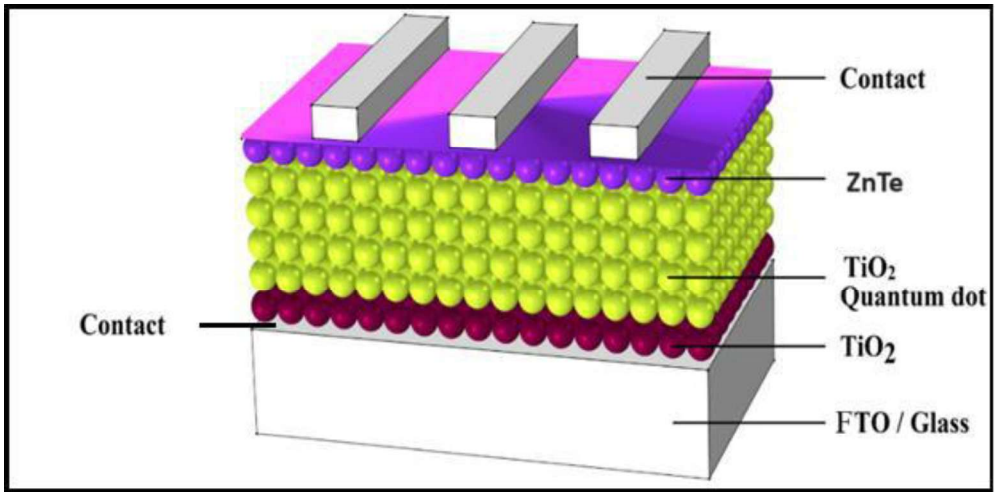

Figure 4.1(a): Schematic illustration of the proposed structure

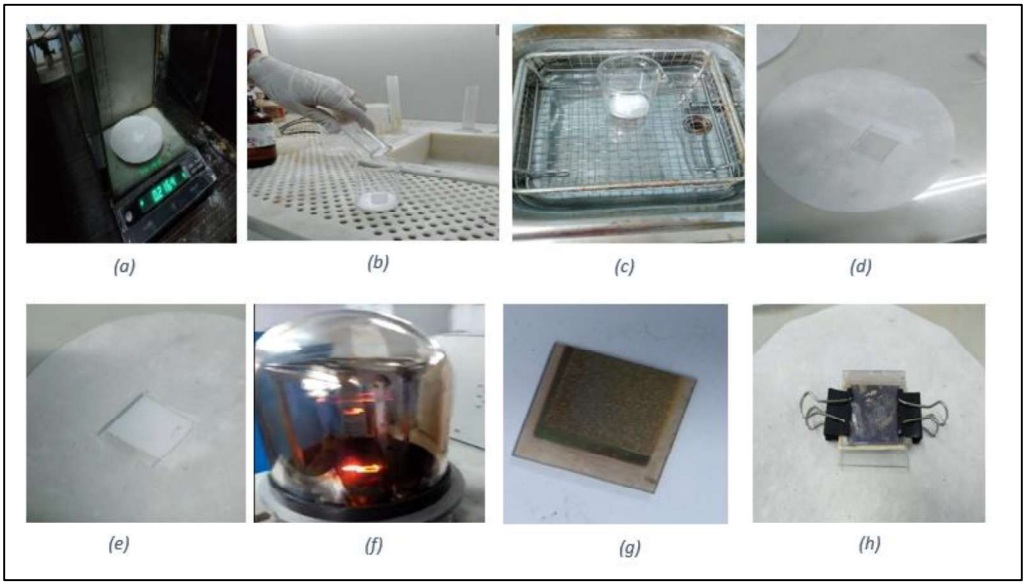

Figure 4.1(b): The fabrication process: (a) Weighing the precursor materials(b), the precursor solution is mixed (c), Ultra sonification of solution (d)Masking of the sample (e)The QD-coated substrate (f) Thermal deposition of ZnTe (g) After deposition of ZnTe. (h) Final assembly.

4.4 Device Physics

Solar efficiency is affected by several factors, including our inability to utilize the entire spectrum of light for electricity production, generation of trap states, charge recombination, and lattice mismatch that facilitates point defects. When developing

a photovoltaic solar cell, the primary goal is to optimize the efficiency-to-cost ratio. Tandem solar cells help to solve this problem to some extent. TiO_2, a broad bandgap material, absorbs the UV range of the spectrum, improving the cell's effectiveness while minimizing expense, compared to the currently used silicon solar cell, which is a narrow bandgap material covering the infrared to the visible light spectrum. The proposed structure can be a suitable candidate for the upper part of a tandem solar cell [4.19]. Quantum dot solar cells adhere to the operational guidelines established by the multiple electron generation. When a bulk semiconductor absorbs one photon, it triggers a transition of electrons moving from the valence band into the conduction band, which has a higher energy level, but if the bulk semiconductor is not paired with another component or a p-n junction is not formed, the electron will instead relax to the lowest of the conduction band, resulting in wasted heat as shown in Fig. 4.2(a) and 4.2(b). This occurs because the energy levels in bulk semiconductors are very tightly separated, and the energy released corresponds to infrared energy. Unlike in QD, the electron, after absorption of a photon, may be exited to LUMO 1. Energy loss in relaxation is sufficient to be in the range of visible light, which gets reabsorbed by the neighbouring electron, and the energy of this visible light is high enough to excite the electron, as shown in Fig. 4.2(b). Multiple generations will only occur if the energy state is distinct enough to produce energy equivalent to photon energy [4.20].

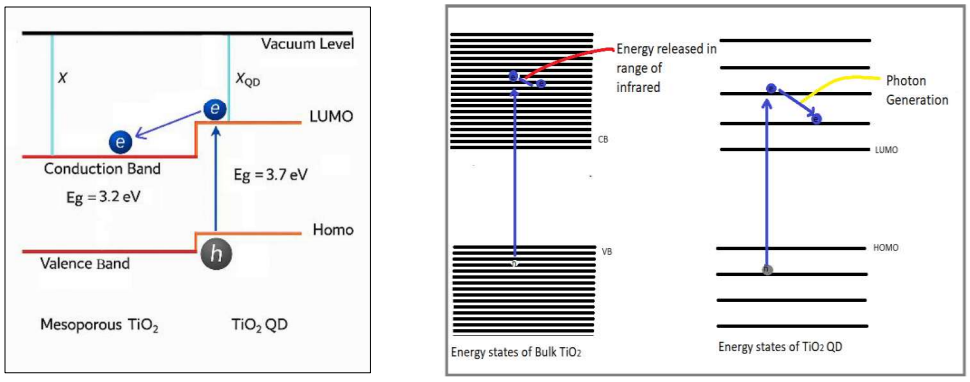

(a) *(b)*

Figure. 4.2(a) Band alignment of TiO_2 mesoporous and TiO_2 QD (b) Energy state of bulk and QD nanomaterials

In contrast to QD, an electron can leave LUMO 1 after it has absorbed a photon, and the very high energy loss that occurs during relaxation puts it within range of visible light. The neighbouring electron will then reabsorb this visible light, and the energy of this visible light is sufficient to activate the electron.

4.4 Result and discussion

The tandem solar cell design leverages the complementary absorption properties of ZnTe and TiO_2 quantum dots (QDs) to enhance overall efficiency. The ZnTe layer effectively absorbs high-energy photons in the ultraviolet (UV) to green region, ensuring efficient utilization of the higher-energy portion of the solar spectrum. This absorption is critical as it harnesses photons that have higher energy levels, thereby contributing significantly to the power conversion efficiency (PCE). Meanwhile, the TiO_2 QDs layer primarily absorbs UV energy and some visible rays, further boosting the efficiency in the high-energy region. The combined absorption characteristics of these two layers ensure a broad coverage of the solar spectrum from the UV to the green area. Additionally, their transparency in the near-infrared region—above 550 nm for ZnTe and above 400 nm for TiO_2 QDs allows lower-energy photons to pass through to the underlying bottom layer [4.21].

This synergy maximizes the use of the entire solar spectrum, leading to higher overall efficiency. Quantum dots (QDs) inherently possess a high density of surface defects, a recombination site for charge carriers. This characteristic can significantly impact the performance of QD-based solar cells. In our study, the interfaces between ZnTe, TiO_2 QDs, and mesoporous TiO_2 play a significant part in the overall device performance. Poor interface quality can lead to substantial efficiency losses due to increased recombination of charge carriers. Specifically, our device's reduced J_{sc} and overall PCE can be attributed to inefficient charge separation at the ZnTe/TiO_2 QD interface. This suggests that the interfacial engineering between these layers needs to be optimized to minimize recombination losses and enhance charge transport [4.22]. Table 4.1 shows the performance of TiO_2 quantum dot (QD) layers as both the interlayer and absorber layer. The V_{oc} of 0.77 V indicates a reasonably good potential difference generated by the cell. However, while moderate, the J_{sc} value of 7.43 mA/cm² points towards potential inefficiencies in the charge production and

collection. The fill factor (FF) of 65.51% indicates moderate charge carrier collection efficiency but also suggests room for improvement in reducing resistive losses within the cell. The fabricated quantum dot (QD) solar cell achieved a power conversion efficiency (PCE) of 4.68%, which was determined using the following formula:

$$\mathrm{PCE}(\%) = \left(\frac{V_{oc} \times J_{sc} \times FF}{P_{in}}\right) \times 100 \quad (4.1)$$

Table 4.1: Performance parameters of fabricated QD solar cell

Interlayer	Absorber Layer	Voc (V)	Jsc (mA/cm²)	FF(%)	PCE(%)
TiO_2 QD	TiO_2 QD	0.77	7.43	65.51%	4.68%

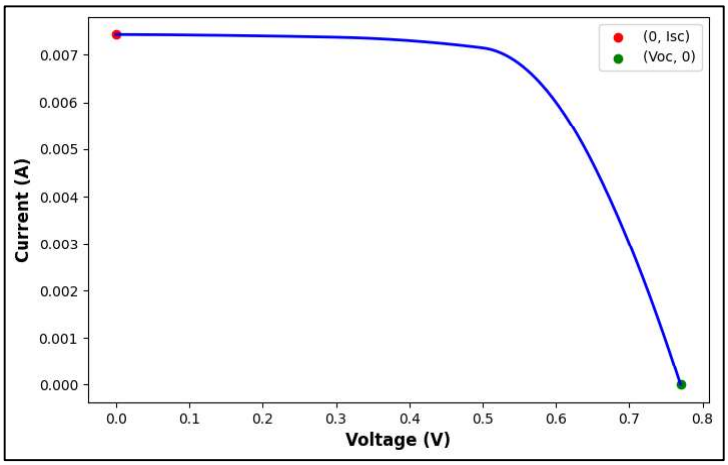

Figure 4.3: IV curves of TiO_2 QD generated using MATLAB-Simulink

In Figure 4.1(a), the schematic diagram of the proposed model shows the device structure consisting of a TiO_2 quantum dot (QD) layer deposited on mesoporous TiO_2, followed by a hole collector layer formed on the surface of the QD layer. This configuration enables effective light absorption, charge separation, and carrier transport within the solar cell. It has been reported that forming heterojunctions with metal oxides can improve the device's general performance. Figure 4.3 shows the I-V characteristics of the proposed model, which is plotted using MATLAB

Simulink. SEM investigations clarified the shape and size distribution of the TiO_2 and mesoporous TiO_2 nanopowder.

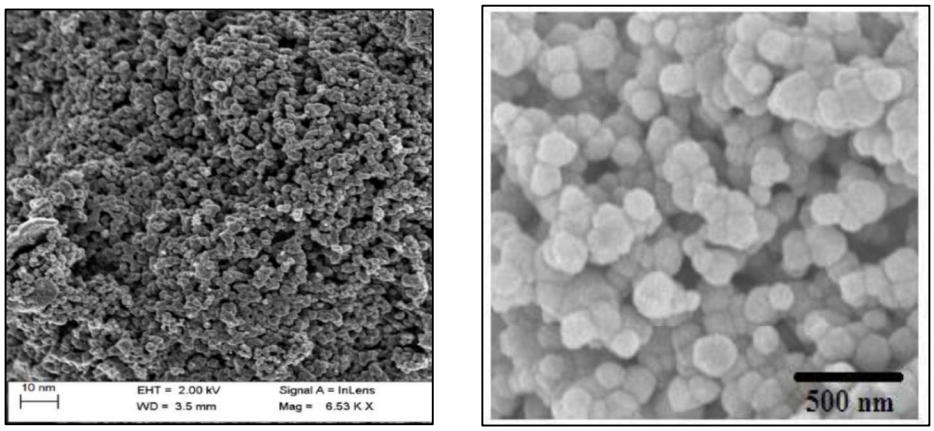

(a) *(b)*

Figure. 4.4 Scanning Electron Microscope image of (a) modified TiO_2 quantum dot (b) mesoporous TiO_2 [4.23]

Figure 4.4(a) is an SEM image of TiO_2 QD, taken at a higher magnification of 65.3 KX with a scale bar of 10 nm, which provides a more detailed view of the particles. It confirms the quantum dot structure of TiO_2, with an average size of 3–4 nm and a highly porous morphology. This type of structure enhances charge transport, as discussed in the experimental section. The rough surface texture observed at this magnification can further enhance the catalytic properties, which are advantageous for photovoltaic and photocatalytic applications. This account shows that sol-gel and ultrasonication are simple and environmentally friendly methods for synthesizing pure QDs of TiO_2 in phases. The quantum dots (QDs) exhibit an exceptionally high surface-to-volume ratio due to their nanoscale dimensions, enhancing their efficiency in applications where increased surface interaction plays a critical role in optimizing performance. Figure 4.4(b) depicts the SEM image of mesoporous TiO_2 particles with a scale bar of 500 nm, confirming their relatively small dimensions, with the majority of particles measuring below 100 nm in diameter. The nanoparticles exhibit a predominantly spherical morphology with a tendency to aggregate, a characteristic commonly observed in nano powders due to their high surface energy and strong interparticle van der Waals interactions. The uniformity in particle size suggests a

controlled synthesis process, resulting in a consistent product. The smooth surface texture of the particles indicates well-crystallized TiO_2, which is beneficial for applications requiring high photocatalytic activity and efficient electron transport in solar cells. The fabrication process yielded TiO_2 nanoparticles in various forms. Ultrasonication plays a crucial role in achieving different particle dimensions and is one of the fastest and most cost-effective techniques for processing nanomaterials. The sonification time can be increased for further size reduction, maintaining the same temperature and flow rate. It is also noted that ultra-sonification produces cavitation. When a fluid's pressure goes below the vapor pressure, it forms bubbles. Shear stresses rupture bubbles, causing small shockwaves that weaken particles over a specific time. Vibrational frequencies create small cracks in sections, causing fracturing particles into smaller sizes. It is also noticed that the sizes of QD particles are not the same instead, there is variation from 3nm to 5 nm on average. The surface defects produced in QD are more than mesoporous TiO_2, as relevant from SEM images; the sonification process could also generate this. It has been reported that if the processing temperature is increased from 45° C to 60° C, the possible defects can be reduced to a significant extent [4.24]. Besides the size of particles, band alignment is also an essential prerequisite for developing optoelectronic devices with heterojunction. It typically controls the movement of charge trajectories through the device. The conduction band of the ETL layer must be at a lower energy than the LUMO of QD, or the electron affinity of ETL must be greater than QD and HTL's. The bandgap (Eg) of the QD TiO_2 (Eg) can be calculated using the Effective Mass Approximation (EMA) equation, and it has been estimated as 3.7eV.

$$\mathrm{Eg(QD)} = \mathrm{Eg(bulk)} + \frac{\hbar}{2R^2}\left(\frac{1}{m_e} + \frac{1}{m_h}\right) - \frac{3.6e^2}{4\pi\in R^2} \qquad (4.2)$$

Where Eg(bulk) is bandgap of TiO_2(3.2 eV), R is the size of QD TiO_2, $\hbar$ is the reduced Plank's constant having value 6.58×10^{-16}, m_e is the effective mass of electron(9.1×10^{-31} kg), m_h is the effective mass of hole, e is charge of electron(1.6×10^{-19}) and $\in$ is dielectric constant(9.4), R is the radius that corresponds to the particle size, which was experimentally determined from SEM and XRD measurements of the synthesized quantum dots. While this method provides a reasonable theoretical estimation, experimental validation through

techniques such as UV-Vis absorption spectroscopy (Abs) and ultraviolet photoelectron spectroscopy (UPS) would be required for precise measurement.

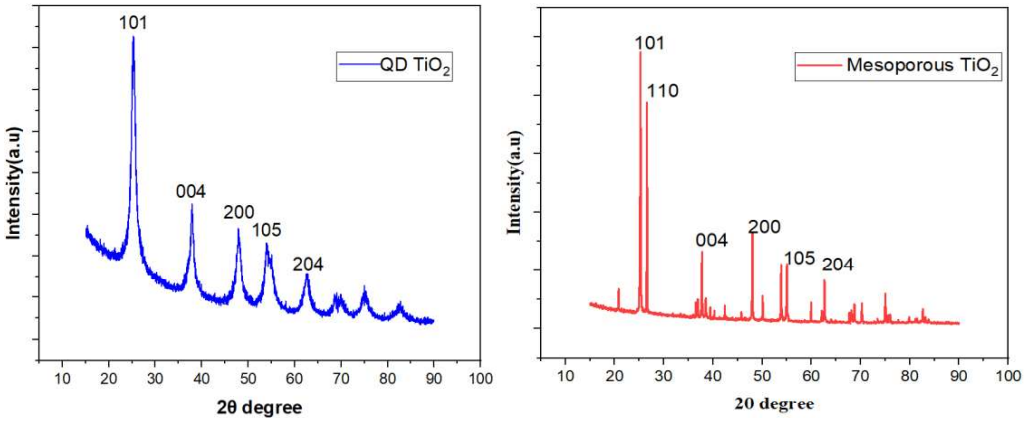

(i) *(ii)*

Figure. 4.5(a): XRD plot of (i) TiO_2 quantum dot (ii) mesoporous TiO_2 [4.23]

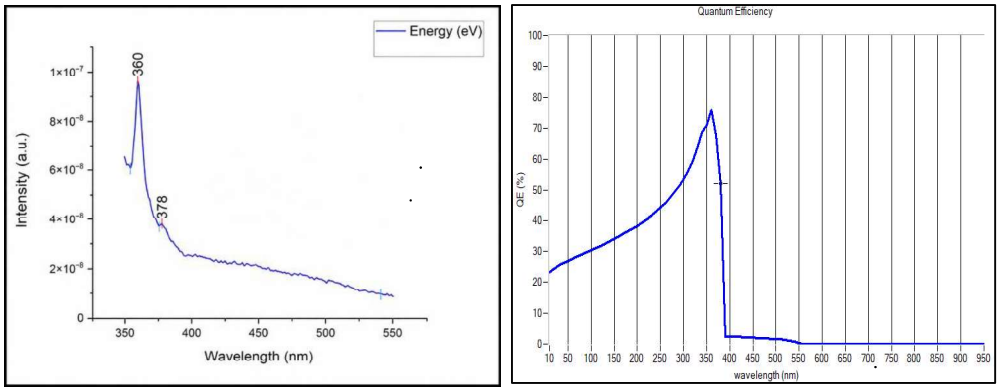

(i) *(ii)*

Figure. 4.5(b): PL spectra of (i) TiO_2 quantum dot (ii) Quantum Efficiency (QE) spectrum of the fabricated quantum dot (QD) solar cell

QD and nanoparticle sizes can also be studied using an X-ray diffraction (XRD) pattern. Figure 4.5(*a*)(*i*) and Figure 4.5(a)(*ii*) show the XRD pattern of TiO_2 QD and TiO_2 mesoporous. The particle size of TiO_2 QDs was estimated using Scherrer's equation applied to XRD data. The Scherer equation is as follows:

$$D = \frac{k\lambda}{\beta\cos\theta} \qquad (4.3)$$

Here, k is a dimensionless shape factor of value 0.9, λ is the wavelength of the X-ray, θ denotes Bragg angle at half maximum intensity, and β is breadth at half peak height of an XRD line. While this method provides a reasonable approximation of crystallite size, it does not account for factors such as agglomeration or variations in particle shape. The average size of TiO_2 QD is calculated as 5.02 nm at peak position (2θ) at 25.28˚,37.86˚, 47.95˚, 54.38˚,69.50˚ and 105.59. The XRD pattern provided likely corresponds to anatase TiO_2 quantum dots, given the peak positions and their broadening. The XRD data is compared with the JCPDS card data for anatase (JCPDS No. 21-1272) and rutile (JCPDS No. 21-1276), which confirm that the observed peaks align well with the expected diffraction patterns of TiO_2. The broadened peaks in Figure 4.5(a)(*i*) occur due to small particle sizes. The XRD pattern predominantly matches one phase (e.g., anatase), which indicates high phase purity. Anatase TiO_2 boasts superior electron mobility, facilitating efficient electron transport from quantum dots to electrodes, thereby reducing recombination losses. Its conduction band aligns well with the energy levels of many quantum dots, promoting efficient electron injection and charge separation. The high surface area of anatase TiO_2 provides more active sites for quantum dot attachment, which increases light absorption and enhances the generated photocurrent.

Additionally, Anatase TiO_2 is chemically stable and resistant to photo corrosion, ensuring long-term durability and consistent performance of QDSCs. Its structure supports efficient charge separation and electron extraction, reducing recombination rates and improving quantum efficiency. Furthermore, anatase TiO_2 enhances light scattering within the solar cell, increasing the optical path length and chances of light absorption by quantum dots. It is versatile and compatible with a wide range of quantum dots, allowing optimization for different spectral ranges and applications. Surface modifications of anatase TiO_2 improve the binding and stability of quantum dots, enhancing overall solar cell performance. In Figure 4.5(a)(*ii*), the pattern indicates the presence of both anatase and rutile phases of TiO_2. The key peaks observed at approximately 25°, 27°, 37°, 48°, 55°, and 62° match well with the (101), (110), (004), (200), (105), and (204) planes of anatase, and the (110) plane of rutile, respectively. The relatively sharp peaks suggest that the TiO_2 particles are well-

crystallized and not in the nanometre size typical of quantum dots. Using the Scherrer equation with an assumed FWHM of 0.1° for the peak at 25°, the estimated crystallite size is approximately 83.4 nm, indicating larger particles, and The average particle size of the mesoporous TiO_2 was determined to be approximately 64.5 nm. This mixed-phase composition of anatase and rutile TiO_2 can be advantageous for solar cell applications, as anatase offers high photocatalytic activity. In contrast, rutile provides better stability and a higher refractive index. Larger TiO_2 particles can enhance electron transport by providing better connectivity between grains and reducing charge recombination losses, thereby improving the overall efficiency of the solar cell [4.25].

The electrical performance of the fabricated TiO_2 quantum dot (QD) solar cell is strongly affected by the size and morphology of the quantum dots, as confirmed by SEM and XRD analyses. Average crystallite size of ~5.02 nm and the narrow particle size range of 3–5 nm promotes quantum confinement, which widens the bandgap to ~3.7 eV and enables selective UV absorption. The high surface-to-volume ratio of these nanostructures facilitates efficient exciton generation and separation, while the mesoporous structure improves light scattering and provides interconnected pathways for charge carrier transport. These structural advantages contribute to effective charge extraction and reduced recombination, supporting the observed short-circuit current density (7.43 mA/cm²) and fill factor (65.51%). Moreover, the relatively uniform particle distribution minimizes interfacial barriers, improving carrier mobility and reducing energy losses. Although minor variations in size may introduce trap states, the controlled synthesis conditions help maintain crystallinity and suppress defect formation. Thus, the particle size distribution and surface architecture of TiO_2 QDs play a critical role in achieving stable and efficient photovoltaic performance in the proposed device structure.

Figure 4.5(b)(*i*) shows the photoluminescence (PL) spectrum of TiO_2 quantum dots (QDs). The spectrum exhibits two key peaks: the primary emission at 360 nm and a secondary emission at 378 nm. The primary peak at 360 nm corresponds to the high-energy UV emission characteristic of the quantum dots' bandgap, indicating an efficient absorption and re-emission of UV light. This property is particularly

advantageous in tandem solar cells, where the top cell, typically a wide-bandgap material, absorbs higher energy photons and transmits lower energy photons to the bottom narrow-bandgap material. The secondary peak at 378 nm suggests the presence of additional emission features, possibly due to surface states or defect states within the TiO_2 QDs. The gradual decrease in intensity beyond these peaks indicates a lower emission at longer wavelengths. The strong UV absorption and emission characteristics of TiO_2 quantum dots (QDs), indicated by peaks at 360 nm and 378 nm, enhance energy transfer processes in tandem solar cells and enable better utilization of the solar spectrum, thereby improving overall efficiency. However, the peak observed at 378 nm, which likely corresponds to defect-related states, underscores the need for precise defect control to reduce non-radiative recombination losses and maintain high device performance. The PL spectrum underscores the potential of TiO_2 QDs to significantly contribute to the performance enhancement of tandem solar cells through effective UV light absorption and emission [4.24, 4.26-4.27].

The Quantum Efficiency plot shown in Figure 4.5(b, *ii*) were recorded across the spectral range of 300–800 nm under steady-state conditions at room temperature. To ensure accuracy, multiple scans were averaged, and experimental inconsistencies due to light fluctuations and sample alignment were minimized. The plot supports the photoluminescence spectrum of TiO_2 quantum dots by confirming their high efficiency in converting UV light into electrical energy. The strong alignment between the quantum efficiency (QE) peak at 360 nm and the photoluminescence (PL) emission peak confirms the effectiveness of TiO_2 quantum dots (QDs) in boosting the UV light response, thereby enhancing the performance of tandem solar cells. This improved UV absorption and conversion capability is crucial for maximizing the efficiency and performance of tandem solar cells, making TiO_2 QDs a valuable component in these advanced photovoltaic systems.

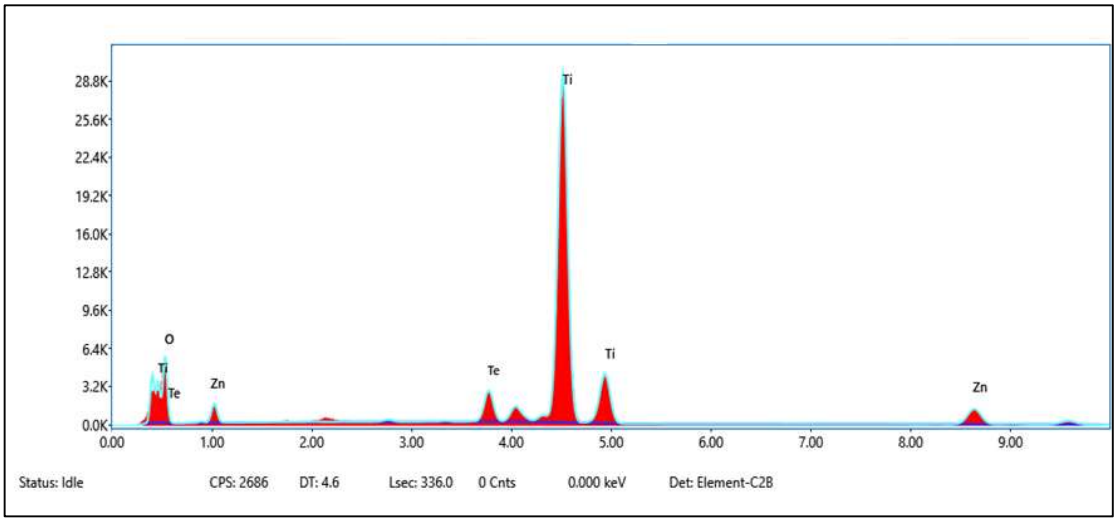

Figure 4.5(c): Energy-dispersive X-ray spectroscopy (EDS) spectrum of the fabricated quantum dot (QD) solar cell

Figure 4.5(c) presents the Energy Dispersive X-ray Spectroscopy (EDS) spectrum of the fabricated sample, showing distinct elemental peaks corresponding to oxygen (O), zinc (Zn), tellurium (Te), and titanium (Ti). The most intense peak appears at approximately 4.5 keV, confirming that titanium is the dominant element in the sample composition. The presence of oxygen suggests the sample contains oxides, such as titanium dioxide (TiO_2). Zinc is identified by peaks around 1.0 keV and 8.6 keV, indicating its presence, potentially in the form of zinc telluride (ZnTe). Tellurium peaks are observed around 3.7 keV and 4.3 keV, suggesting the sample includes tellurium compounds.

Compared to well-established quantum dot systems such as CdS/CdSe and $CuInS_2$-based structures, the TiO_2 QD-based device in this work exhibits a distinct design philosophy and functionality. While co-sensitized multilayer photoanodes like TiO_2 NCs/TiO_2 HSs/CIS/CdS/CdSe(Xmin)/ZnS have achieved higher efficiencies up to 8.54% through band alignment engineering and co-passivation strategies they primarily operate in the visible region and require complex layer stacking and toxic materials like Cd or In. In contrast, the use of non-toxic, stable, and scalable TiO_2 QDs offers a compelling route to enhancing overall tandem cell performance by capturing UV photons that most absorbers neglect. It also provides an additional benefit of photostability and protection for underlying absorber layers. Furthermore,

unlike CdSe or CIS QDs which require strict synthesis conditions or surface treatments, the TiO_2 QDs in this study were synthesized using a low-cost, environmentally friendly sol-gel approach [4.9, 4.11].

Reference

[4.1] Yang, S., Fu, W., Zhang, Z., Chen, H., Li, C., "Recent advances in perovskite solar cells: efficiency, stability and lead-free perovskite." Journal of Materials Chemistry A, 2017, DOI: 10.1039/C7TA00366H (RSC Publishing).

[4.2] Chen, Y., Zhang, M., Li, F., Yang, Z. "Recent Progress in Perovskite Solar Cells: Status and Future." Coatings, 2023. DOI: 10.3390/coatings13030644 (MDPI).

[4.3] Wang, Z. "Recent progress in perovskite solar cells: material science." in Science China Chemistry, 2021. DOI: 10.1007/s11426-021-9978-6 (Springer).

[4.4] Song, J.H., Jeong, S. "Colloidal quantum dot based solar cells: from materials to devices" in Nano Convergence 4, 21 (2017), DOI: https://doi.org/10.1186/s40580-017-0115-0.

[4.5] M. C. Beard, "Multiple exciton generation in semiconductor quantum dots," J. Phys. Chem. Lett., vol. 2, no. 11, pp. 1282–1288, 2011.

[4.6] Sargent et al. (2015). "Colloidal Quantum Dot Photovoltaics: The Rise and Fall of a Research Field." Nano Letters, 15(2), 842–848. https://doi.org/10.1021/nl504086v

[4.7] Sargent et al. (2020). "Recent Advances in Colloidal Quantum Dot Solar Cells: Challenges and Opportunities." Advanced Functional Materials, 30(29), 2005930. https://doi.org/10.1002/adfm.202005930

[4.8] Sargent et al. (2021). "Colloidal Quantum Dot Optoelectronics: Progress and Challenges." Nature Communications, 12, 20749. https://doi.org/10.1038/s41467-020-20749-1

[4.9]. Karkhaneh, A., Marandi, M., "Facile fabrication of quantum dot–sensitized solar cells with multilayer TiO2 NCs/TiO2 HSs/CIS/CdS/CdSe(Xmin)/ZnS photoanode and modification of light scattering and co-sensitization for higher efficiencies", emergent mater. (2024). https://doi.org/10.1007/s42247-024-00705-1

[4.10].J. B. Baxter and E. S. Aydil, "Nanowire-based dye-sensitized solar cells," Appl. Phys. Lett., vol. 86, no. 5, p. 053114, 2005.

[4.11]. Atefeh Karkhaneh, Maziar Marandi, "Modified synthesis of CuInS2 nanoparticles for enhancement of the efficiency of corresponding quantum dot-sensitized solar cells: a simplified aqueous approach" Emergent Materials, 10.1007/s42247-024-00987-5.

[4.12] Sahu, A.; Garg, A.; Dixit, A., "A review on quantum dot sensitized solar cells: Past, present and future towards carrier multiplication with a possibility for higher efficiency" in Sol. Energy 2020, 203, 210–239.

[4.13] Pandey, R.; Khanna, A.; Singh, K.; Patel, S.K.; Singh, H.; Madan, J., "Device simulations: Toward the design of >13% efficient PbS colloidal quantum dot solar cell", in Sol. Energy 2020, 207, 893–902.

[4.14] Tanabe, K. "A Review of Ultrahigh Efficiency III-V Semiconductor Compound Solar Cells: Multijunction Tandem, Lower Dimensional, Photonic Up/Down Conversion and Plasmonic Nanometallic Structures", Energies 2009, 2, 504-530. DOI: https://doi.org/10.3390/en20300504.

[4.15] Rahman, D.Y., Rokhmat, M., Yuliza, E. et al., "New design of potentially low-cost solar cells using TiO2/graphite composite as photon absorber", in Int J Energy Environ Eng 7, 289–296 (2016), DOI: https://doi.org/10.1007/s40095-016-0213-5.

[4.16] Sofia Javeda, Mohammad Islam, Mohammad Mujahida, "Synthesis and Characterization of TiO2 Quantum Dots by Sol Gel Reflux Condensation Method", in October 2018, Ceramics International 45(2) 45(2), DOI:10.1016/j.ceramint.2018.10.163.

[4.17] Weimin Yang, Huafang Yang, Wenhao Ding, Bing Zhang, Le Zhang, Lixi Wang, Mingxun Yu, Qitu Zhang, "High quantum yield ZnO quantum dots synthesizing via an ultrasonication microreactor method", Ultrasonics Sonochemistry, Volume 33, 2016, Pages 106-117, ISSN 1350-4177, DOI: https://doi.org/10.1016/j.ultsonch.2016.04.020.

[4.18] K. M. U. Rehman, X. Liu, M. Riaz, Y. Yang, S. Feng, M. W. Khan, A. Ahmad, M. Shezad, Z. Wazir, Z. Ali, K. M. Batoo, S. F. Adil, M. Khan and E. H. Raslan, "Fabrication and characterization of Zinc Telluride (ZnTe) thin films grown on glass

substrates", Phys. B, 2019, 560, 204 —207, DOI: https://doi.org/10.1016/j.physb.2019.02.043.

[4.19] Y. Zhang, M. Gu, N. Li, Y. Xu, X. Ling, Y. Wang, S. Zhou, F. Li, F. Yang, K. Ji, J. Yuan and W. Ma, "Realizing solution-processed monolithic PbS QDs/perovskite tandem solar cells with high UV stability", J. Mater. Chem. A, 2018, 6, 24693 DOI: 10.1039/C8TA09164A

[4.20] Wang, H., & Fu, Q., "Recent advances in perovskite quantum dot-based tandem solar cells." In 2020, Nano Energy, 68, 104303, DOI: 10.1016/j.nanoen.2019.104303.

[4.21] Deepak Suthar, Sakshi Chuhadiya, Ritika Sharma, Himanshua and M. S. Dhaka, "An overview on the role of ZnTe as an efficient interface in CdTe thin film solar cells: a review", in Mater. Adv., 2022,3, 8081-8107, https://doi.org/10.1039/D2MA00817C.

[4.22] Weyde M. M. Lin, Nuri Yazdani, Olesya Yarema, Maksym Yarema, Mengxia Liu, Edward H. Sargent, Thomas Kirchartz and Vanessa Wood, "Recombination Dynamics in PbS Nanocrystal Quantum Dot Solar Cells Studied through Drift–Diffusion Simulations" in ACS Applied Electronic Materials ACS Appl. Electron. Mater. 2021, 3, 1, 1, 4977–4989, DOI: https://doi.org/10.1021/acsaelm.1c00787.

[4.23] Komal Kumari, Tapas Chakrabarti, Subir Kumar Sarkar, Metal oxide nanoparticles as an electron-transport layer in perovskite solar cell", Optical Materials,Volume 142, 2023,114047,ISSN 0925-3467, https://doi.org/10.1016/j.optmat.2023.114047.

[4.24] Y. Tu, J. Wu, M. Zheng, J. Huo, P. Zhou, Z. Lan, J. Lin and M. Huang, "TiO2 quantum dots as superb compact block layers for high-performance CH3NH3PbI3 perovskite solar cells with an efficiency of 16.97%", in Nanoscale, 2015,7, 20539-20546, DOI: https://doi.org/10.1039/C5NR05563F.

[4.25] Morris Hotsenpiller, P. A., Bolt, J. D., Farneth, W. E., Lowekamp, J. B. & Rohrer, G. S., "Orientation dependence of photochemical reactions on TiO2 surfaces", in J. Phys. Chem. B 102, 3216–3226 (1998).

[4.26] A. Andruszkiewicz, X. Zhang, M. B. Johansson, L. Yuan and E. M. J. Johansson, "Perovskite and quantum dot tandem solar cells with interlayer modification for improved optical semitransparency and stability", in Nanoscale, 2021, 13, 6234 DOI: https://doi.org/10.1039/D0NR08375E.

[4.27] C. Ding, Y. Zhang, F. Liu, Y. Kitabatake, S. Hayase, T. Toyoda, R. Wang, K. Yoshino, T. Minemoto and Q. Shen, "Understanding charge transfer and recombination by interface engineering for improving the efficiency of PbS quantum dot solar cells", Nanoscale Horiz., 2018, 3, 417-429, DOI: https://doi.org/10.1039/C8NH00030A.

[4.28] W. Shockley and H. J. Queisser, "Detailed balance limit of efficiency of p–n junction solar cells," *J. Appl. Phys.*, vol. 32, no. 3, pp. 510–519, 1961.

[4.29] M. C. Beard, "Multiple exciton generation in semiconductor quantum dots," *J. Phys. Chem. Lett.*, vol. 2, no. 11, pp. 1282–1288, 2011.

[4.30] J. H. Song and S. Jeong, "Colloidal quantum dot based solar cells: from materials to devices," *Nano Converg.*, vol. 4, p. 21, 2017.

[4.31] E. H. Sargent *et al.*, "Colloidal quantum dot photovoltaics: the rise and fall of a research field," *Nano Lett.*, vol. 15, no. 2, pp. 842–848, 2015.

[4.32] E. H. Sargent *et al.*, "Recent advances in colloidal quantum dot solar cells: challenges and opportunities," *Adv. Funct. Mater.*, vol. 30, no. 29, p. 2005930, 2020.

[4.33] E. H. Sargent *et al.*, "Colloidal quantum dot optoelectronics: progress and challenges," *Nat. Commun.*, vol. 12, p. 20749, 2021.

[4.34] J. B. Baxter and E. S. Aydil, "Nanowire-based dye-sensitized solar cells," *Appl. Phys. Lett.*, vol. 86, no. 5, p. 053114, 2005.

[4.35] A. Karkhaneh and M. Marandi, "Modified synthesis of $CuInS_2$ nanoparticles for enhancement of the efficiency of corresponding quantum dot-sensitized solar cells: a simplified aqueous approach," *Emerg. Mater.*, 2025.

[4.36] A. Sahu, A. Garg, and A. Dixit, "A review on quantum dot sensitized solar cells: past, present and future towards carrier multiplication with a possibility for higher efficiency," *Sol. Energy*, vol. 203, pp. 210–239, 2020.

[4.37] Y. Tu *et al.*, "TiO_2 quantum dots as superb compact block layers for high-performance $CH_3NH_3PbI_3$ perovskite solar cells with an efficiency of 16.97%," *Nanoscale*, vol. 7, pp. 20539–20546, 2015.

[4.38] R. Pandey *et al.*, "Device simulations: toward the design of >13% efficient PbS colloidal quantum dot solar cell," *Sol. Energy*, vol. 207, pp. 893–902, 2020.

[4.39] K. Tanabe, "A review of ultrahigh efficiency III–V semiconductor compound solar cells: multijunction tandem, lower dimensional, photonic up/down conversion and plasmonic nanometallic structures," *Energies*, vol. 2, pp. 504–530, 2009.

[4.40] Y. Zhang *et al.*, "Realizing solution-processed monolithic PbS QDs/perovskite tandem solar cells with high UV stability," *J. Mater. Chem. A*, vol. 6, p. 24693, 2018.

[4.41] A. Jana, K. Kumari, B. Gupta, and S. K. Sarkar, "Quantum dot metal oxide for UV ray utilization in tandem solar cell," *Opt. Quantum Electron.*, vol. 57, no. 339, 2025.

[4.42] K. Kumari, T. Chakrabarti, and S. K. Sarkar, "Metal oxide nanoparticles as an electron-transport layer in perovskite solar cell," *Opt. Mater.*, vol. 142, p. 114047, 2023.

[4.43] D. Suthar *et al.*, "An overview on the role of ZnTe as an efficient interface in CdTe thin film solar cells: a review," *Mater. Adv.*, vol. 3, pp. 8081–8107, 2022.

Chapter 5

A Crossbar Architecture based System (CAS) as Hydrogen Gas sensing platform

5.1. Introduction:

Gas sensing has become crucial in various real-life circumstances ranging from domestic arenas to industrial complexes in the field of health, food, chemical, and automation to name a few. Besides, the area is provided with more impetus for maintaining environmental norms, censoring pollution, and exploring scientific investigations [5.1-5.5]. For satisfying the future demand for sustainable energy sources, hydrogen has emerged as an attractive choice due to its highest specific energy content with a yield of about 122 kJ/g, eco-friendly and renewable characteristics [5.6, 5.7]. It is also employed in fuel cell production, petroleum refining, generators, nuclear reactors, and so on. If employed, green-hydrogen technology can foster decarbonization and attain the economic evolution that will emphasize sustainable development.

Despite all these magnificent features, hydrogen is extremely flammable and explosive because of low ignition energy, low boiling point, and broader flammable span with air–fuel ratio from 0.14 to 10 [5.8-5.11]. In particular, the detection of hydrogen gas is considered to be an important research front rapid detection of gas leakage is a necessity [5.12]. Hence, it is of utmost importance to create highly selective, rapid sensing, low-cost, energy efficient, and scalable hydrogen sensors for fast detection even at a low concentration.

Over the past few decades, field effect transistor (FET) based hydrogen gas sensors have been widely explored and are high in demand. Attributes like low-power consumption, better on-chip integration, good sensitivity, and capability of detecting weakly adsorbed molecules make FET-based gas sensors a promising choice. The first FET hydrogen sensor was proposed in 1975 by Lundstrom et.al. [5.13] where Palladium was considered as the sensing gate electrode. The results presented in this study show that a palladium-gate MOS transistor can effectively operate as a hydrogen sensor, demonstrating a sensitivity of around 10 ppm of hydrogen in air and exhibiting a reasonable response time when operated at 150°C. Following up, various FET structures have been proposed for hydrogen sensing. In 2008, M. Safari et.al. proposed an SOI-based MOSFET hydrogen sensor with a platinum gate electrode [5.14]. They modeled the dipole created at the interface of Pt/SiO_2 as a capacitor to capture the effect of adsorbed hydrogen gas on the platinum surface at different pressures. In this study, the authors presented an analytical approach to monitor changes in the threshold voltage and formulated an equation to predict its variation in a MOSFET-based gas sensor under different hydrogen gas pressures. Owing to their superior sensitivity and lower power consumption compared to conventional MOSFETs, Tunnel Field-Effect Transistor (TFET)-based gas sensors have also been extensively investigated in recent years. In 2012, D. Sarkar et.al. proposed a TFET hydrogen sensor that exhibited 10000 times better sensitivity in comparison to the MOSFET counterpart [5.15]. Jaya Madan and Rishu Chaujar studied a hetero-dielectric TFET as a hydrogen gas sensor that leverages the band-to-band tunneling phenomenon [5.16]. Their findings revealed that at a pressure of 1×10^{-10} Torr, the sensitivity of a conventional Tunnel Field-Effect Transistor (TFET) is approximately 626 times greater than that of a conventional MOSFET, highlighting the superior detection capability of TFET-based gas sensors. Gate-All-Around (GAA) FETs are also demonstrated for hydrogen gas sensing. S. Mokkapati et.al. studied a junctionless (JL) GAA nanowire gas sensor with a palladium gate material [5.17]. Their work focussed on low-power hydrogen sensing for a range of ambient temperatures (250-450 K) at various gas pressures. They achieved a threshold voltage sensitivity of ~100 mV and current sensitivity of ~40 for 10^{-10} Torr hydrogen gas pressure. Y. Pratap el. al focussed on exploring the impact of

geometrical parameters of a GAA JL FET on its sensitivity [5.18]. Their conclusion was that the Gate-All-Around (GAA) Junctionless Transistor (JLT) exhibits superior sensitivity compared to the inversion mode GAA MOSFET. By incorporating the Gate-All-Around (GAA) structure, the sensor's sensitivity is further enhanced by nearly three times compared to the conventional TFET. This improvement results from the superior electrostatic control offered by the cylindrical GAA geometry, which enables better modulation of the channel potential.

Furthermore, at the same hydrogen pressure of 1×10^{-10} Torr, the High-Dielectric (HD) GAA-TFET demonstrates a remarkable increase in sensitivity — approximately 3.5×10^{4} times higher than the conventional MOSFET, 56 times higher than the conventional TFET, and 30 times higher than the standard GAA-TFET, respectively. Recently, in 2021, H.D. Sehgal et.al proposed a junctionless fin field effect transistor (JL-FinFET) based hydrogen sensor where threshold voltage sensitivity was found to be 0.53 V at 10^{-10} Torr with 40 nm fin height and 50 nm channel thickness [5.19]. Other FET architectures like trench gate MOSFET [5.20] and polarity-controlled FET [5.21] have also been used for hydrogen gas sensors.

Hydrogen sensors can be broadly categorized into several types, including catalytic, electrochemical, resistance-based, work function-based, and optical sensors [5.22, 5.23]. Among them, the micromachined thermoelectric hydrogen sensor (μ-THS), developed for use in hydrogen refueling stations, exhibits a linear response over a wide hydrogen concentration range in air—from 10 ppm to 4%. Additionally, amperometric hydrogen sensors have been reported to detect hydrogen concentrations ranging from 5 ppm (in argon) up to 100%, demonstrating their wide applicability. Moreover, thin films of palladium-coated Mg–Ni alloys have been investigated for room-temperature hydrogen detection, effectively covering a detection range between 10 ppm and 10%, showing strong potential for low-power, ambient-condition operation. Work-function based detection method is more advantageous as it can detect as low as 5 ppm of hydrogen gas. The main principle of such sensors is the work-function variation when gas molecules are adsorbed over the surface. For this method of detection, metal-semiconductor Schottky diodes (MSD) and metal-oxide-semiconductor field effect transistors (MOSFET) are

popular choices. In hydrogen-sensitive MOS structures, hydrogen atoms diffuse through the metal layer and adsorb at the metal–oxide interface. At this interface, the adsorbed hydrogen atoms become polarized, forming a dipole layer that modifies the metal work function and shifts the energy levels at the metal–insulator interface.Typically, palladium (Pd) and platinum (Pt) are the most commonly used materials for hydrogen gas sensing due to their high catalytic activity and strong hydrogen absorption capability. However, other materials such as iridium (Ir) [5.24], palladium–silver (Pd–Ag) alloys [5.25], and palladium–chromium (Pd–Cr) composites [5.26] have also been explored as gate electrodes in metal–insulator–semiconductor (MIS) configurations to enhance sensor performance and stability. However, sensors that rely on a single device are often prone to measurement inaccuracies due to several factors:

a) Unstable response over time,

b) Lack of reproducibility between measurements, and

c) Challenges in maintaining high resolution across a wide range of sample concentrations.

These limitations highlight the need for advanced sensor architectures or array-based systems to achieve greater accuracy and reliability [5.27]. Such errors can be plunged significantly by interpreting multiple measurement data from a single sensor. A faster approach is the use of an array of multiple sensors [5.28] which is even able to cater as a real-time detector of multiple gases [5.29]. The crossbar architecture gas sensors have been reported with two perpendicularly intersecting sets of wires with a sensing device placed at each intersecting point [5.27]. Thus, the crossbar architecture is deployed in memristor-based memory to utilize the advantage of very high-density composition. SnO_2-based sensors array has proved to be commercially viable for detecting multiple organic samples [5.30, 5.31].

With the promotion of the Internet of Things (IoT), the requirement for miniaturized gas sensors has amplified manyfold with the prime requirement of scalability, and reliability with extremely low power consumption [5.32- 5.33]. To meet such requirements without compromising sensitivity, selectivity, and reliability, hydrogen gas sensors based on the metal-semiconductor Schottky devices can be proved to be promising candidates. When the array is exposed to the gas, the work function of the sensing electrode changes based on the pressure of the gas

molecules, impacting the current conduction. In this manner, the crossbar architecture can be put to efficient use as a gas sensor using change in work function [5.27, 5.28]. However, Sneak path current (SPC) is one of the unavoidable phenomena in crossbar array configuration [5.34, 5.40] which are unsought current paths in crossbar that result in degraded read accuracy and overall flawed performance in sensor application [5.27].

In this work, we have proposed a crossbar-based architecture for gas sensing applications. The main motivation is to design a system with the capability to detect gas molecules at different footprints. With this crossbar architecture, we can witness how the output current distribution changes for different at different gas pressure. This is because of its capability to incorporate the slightest current response of the gas molecules at different pressures during voltage sweep. Moreover, such architecture can provide a considerable solution to detect different gas molecules which have very close characteristics.

5.2 Literature Review

5.2.1 Early Developments in Hydrogen Gas Sensors

Hydrogen sensing has been a research priority since the 1970s, largely due to hydrogen's promise as a clean energy carrier alongside its extreme flammability. The earliest milestone was the demonstration of a palladium-gated MOSFET hydrogen sensor by Lundström *et al.* in 1975 [5.56]. This device showcased that palladium, due to its unique catalytic properties, could selectively adsorb and dissociate hydrogen molecules, thereby altering the work function and modulating transistor characteristics. It achieved sensitivities in the order of 10 ppm at elevated temperatures, laying the groundwork for MOSFET-based hydrogen detectors.

5.2.2 Transition to Advanced FET Architectures

Subsequent decades saw refinements in MOSFET hydrogen sensors. In 2008, Safari *et al.* modeled platinum-gated SOI MOSFETs as hydrogen sensors, using capacitive dipole models to relate threshold voltage shifts with gas adsorption [5.57]. While MOSFETs provided robust platforms, their sensitivity was limited. To address this, tunnel field-effect transistors (TFETs) emerged as ultra-sensitive alternatives. In 2012, Sarkar and Banerjee demonstrated that TFET-based hydrogen sensors could

outperform MOSFETs by several orders of magnitude in sensitivity due to their band-to-band tunneling mechanism [5.58]. Further progress came from hetero-dielectric TFETs (Madan and Chaujar, 2016), gate-all-around nanowire FETs [5.59], and junctionless FinFETs [5.60], each architecture improving gate controllability, reducing leakage, and enabling lower detection limits under varying pressures and temperatures.

5.2.3 Diversification of Hydrogen Sensor Technologies

Alongside FET-based sensors, other approaches matured. Catalytic sensors, electrochemical detectors, and resistive metal-oxide sensors became common for industrial safety and environmental monitoring [5.61, 5.62]. Work-function-based detectors using Schottky diodes and MOS capacitors, especially with palladium and platinum electrodes, gained prominence for their ability to detect hydrogen concentrations down to a few ppm. Materials innovation further expanded the palette: Pd–Ag and Pd–Cr alloys, iridium contacts, and Mg–Ni thin films were introduced to improve selectivity and stability [5.63-5.65]. Despite progress, single-device architectures suffered from reproducibility issues, noise susceptibility, and limited scalability.

5.2.4 Emergence of Sensor Arrays and Crossbar Architectures

To overcome the shortcomings of single-sensor devices, the concept of sensor arrays gained traction in the 2010s. Multi-element arrays allowed averaging of responses, redundancy for error minimization, and multiplexed detection of multiple gases [5.66, 5.67]. Crossbar architectures, originally developed for high-density memory, were adapted to gas sensing by embedding sensing elements at each wire junction. This approach enabled massively parallel, scalable, and miniaturized sensor systems with potential for IoT-driven applications [5.68], [5.69]. However, the key challenge that emerged was sneak-path currents (SPC), which degraded sensing accuracy in dense arrays [5.70].

5.2.5 Toward Crossbar-Based Hydrogen Sensors

The growing emphasis on IoT, low-power electronics, and real-time gas monitoring in the 2020s has reinforced the need for compact, reliable hydrogen sensing platforms

[5.71]. Leveraging crossbar arrays provides unique advantages: spatial voltage distribution enables many-to-many mapping between reference and sensing states, inherently boosting sensitivity and robustness. Recent simulation frameworks, including TCAD and hydrogen adsorption models, have been used to capture Schottky barrier modulation at palladium electrodes and predict crossbar-level performance trends. Key insights show that interconnect resistance, electrode work function shifts, and array size directly govern voltage/current distributions and sensitivity metrics, providing critical design rules for scalable fabrication.

Synthesis: The trajectory of hydrogen gas sensors has evolved from single-device palladium MOSFETs in the 1970s [5.56] to advanced FET families (SOI MOSFETs, TFETs, FinFETs, and GAA FETs) [5.57-5.60], and finally to array-based platforms exploiting crossbar architectures [5.66-5.70]. While early sensors established hydrogen detection as viable, crossbar-based architectures now represent the frontier by combining scalability, IoT integration, and enhanced sensitivity—a transition clearly embodied in the 2024 study of Jana *et al.* on CAS-based hydrogen gas sensing platforms [5.71].

5.3. Proposed fabrication recipe:

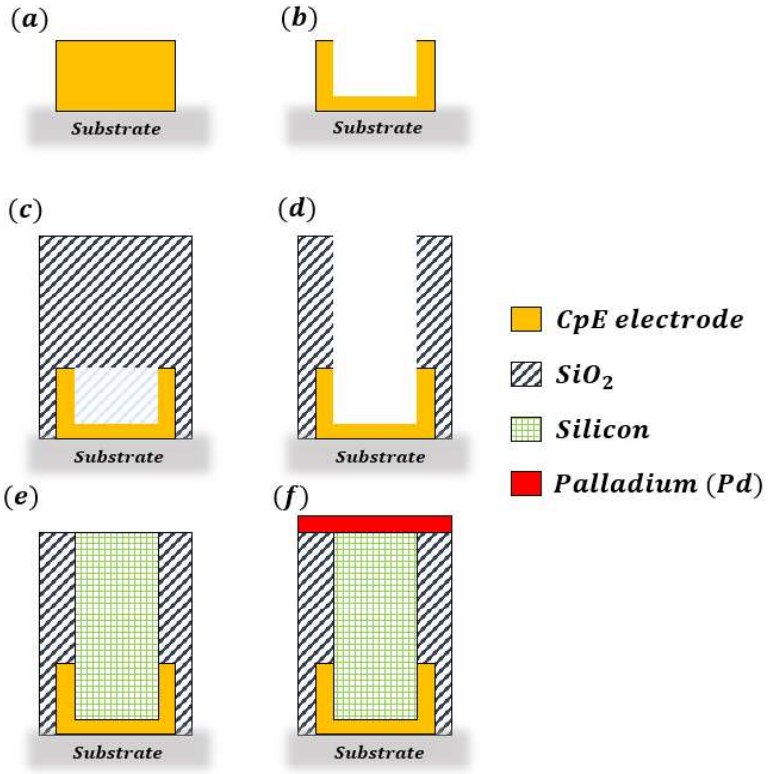

Fig 5.1: Proposed fabrication methodology of the single sensing device which is integrated into a crossbar network.

For the experimental implementation of the proposed architecture, we have proposed the following fabrication steps which may spur future experimental works. The steps are as follows:

(i) Vertical and horizontal copper electrode lines, each with a thickness of 2 nm, are deposited on the surface of a clean silicon wafer through precise patterning using nanolithography, followed by electron beam evaporation. This process ensures accurate alignment and uniform electrode formation essential for the crossbar architecture. Several strategies have been developed to form nanostructures electrochemically. It is one of the promising techniques to fabricate nanowire sensor arrays [5.41-5.44].

(ii) Each cell of the sensor array (composed of charge-plasma electrode (CpE)/crystalline silicon/ sensing electrode (SE)) is fabricated simultaneously at the

point of intersection of copper lines. 12 nm thick and 14 nm wide composed of charge-plasma electrode (CpE) layer is deposited on the intersection of each copper grid via a layer-by-layer chemical deposition technique [5.45].

(iii) A trench of 10 nm depth and 10 nm broad is created in the (CpE) region via dry etching.

(iv) Crystalline silicon is grown into the trench of CpE via an oxidation control technique. To obtain the desired height and diameter of 25 nm and 10 nm respectively, double oxidation is carried out. The first oxidation will be at 900° C and the second at 1000° C temperature [5.46].

(v) Surface of the silicon pillar will be masked using a nanolithography process so that the entire structure can be isolated from each other via an isolation layer (SiO_2). Lithography at the nanoscale can be achieved using a negative-tone photoresist that contains a radical photo-initiator capable of being excited through two-photon absorption. This technique allows precise patterning with sub-100 nm resolution, enabling the fabrication of complex nanostructures while minimizing exposure damage and enhancing spatial control.[5.47].

(vi) Isolation layer of Silicon dioxide is deposited on the entire structure, by plasma-enhanced chemical vapor deposition (PECVD). A gas mixture of nitrous oxide (N_2O) and silane should be used in PECVD [5.48].

(vii) Photo resist is removed from the surface of the silicon pillar and sensing electrode of 2 nm thickness is deposited on the surface of crystalline silicon by UPD (Under potential deposition) [5.49]. UPD is an electrochemical process to deposit a single layer of atoms onto a surface.

(viii) Again negative-tone photoresist is deposited on the entire surface including the side walls of sensing electrode and except the upper part of sensing electrode (it will be masked).

(ix) Counter electrode lines of copper (2 nm thickness) will be deposited electrochemically. These lines will join all cells together.

(x) After the deposition of copper lines, the photoresist will be etched from the surface of the isolation layer as well as from the side walls of sensing electrode. Generally, propylene glycol monomethyl ether acetate (PGMEA) is used to remove the negative-tone photoresist.

There are several steps at which the variability induced during fabrication can impact the proposed sensor network performance. Although it is difficult to estimate all the factors through which discrepancy may creep in, some points are listed below:
(a) *Wordline and Bitline fabrication*: During the deposition of interconnect metals to create wordlines and bitlines, the thickness of the electrode is a critical parameter that directly affects the resistance of the interconnects. Thinner electrodes increase resistance, leading to greater voltage drops and power losses, while thicker electrodes reduce resistance but may cause fabrication challenges such as step coverage issues or increased parasitic capacitance. Therefore, optimizing electrode thickness is essential to balance electrical performance, fabrication feasibility, and device reliability. As can be seen from our simulation framework, the variation in interconnect resistance can cause changes in the sensitivities of the individual devices in the proposed network. Moreover, due to variability in metal deposition, the interconnect resistance may not be consistent over the entire interconnect, thus the sensitivity can get impacted.
(b) *Sensing device fabrication*: The variability in the fabrication of a single device can usher in stochasticity in the sensitivity of a single device which will reflect on the conductance of the sensing devices in the proposed crossbar network causing variation in the readout current, subsequently system sensitivity.
(c) *Readout circuity*: Although not addressed in this manuscript, the readout circuit will play a vital role in determining both the readout current and the overall sensitivity of the sensor system. The circuit's design influences signal amplification, noise performance, and linearity—factors that are essential for accurate detection and reliable measurement in crossbar-based sensing architectures. Thus, fabrication-wise variability in the readout circuit will cause stochasticity in the network sensitivity.

5.4. Simulation Methodology:

5.4.1 Hydrogen Gas Model:

The hydrogen (H_2) gas sensing mechanism is primarily based on the adsorption and dissociation of hydrogen molecules on the palladium (Pd) electrode surface [5.35]. During this process, hydrogen molecules dissociate into atomic hydrogen, and some of these atoms diffuse into the metal layer, forming dipoles at the metal–

semiconductor interface. These interfacial dipoles modify the local work function and influence the electrical characteristics of the device, enabling hydrogen detection. Consequently, the work function of the metal changes.

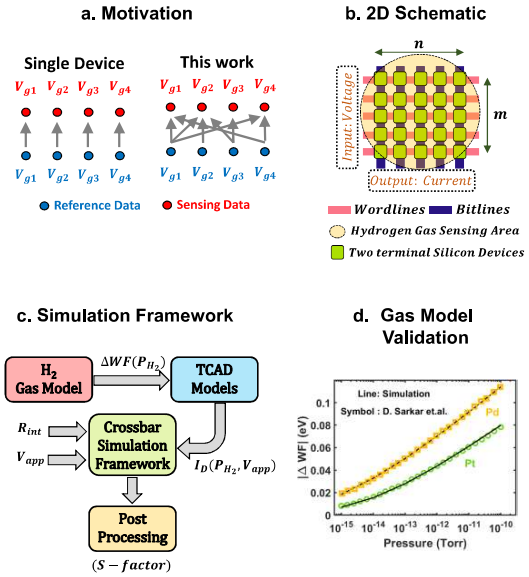

Figure 5.2: The crossbar architecture for hydrogen sensing: (a) Motivation for the crossbar network. For a single sensor device, we can perform one-to-one sensing between reference data (with no gas) and sensing data (with gas). However, with a crossbar network, due to inherent spatial voltage distribution, we can obtain many-to-many mapping between reference and sensing data. (b) Crossbar architecture schematic for the proposed system with all components. (c) Simulation framework of this work including all the models. (d) Validation of the gas model with previously reported study [5.15]

For analytical formalism of the work function change due to gas molecules, first, we calculate the flux of the gas (ψ), given by:

$$\psi = \frac{P}{\sqrt{2\pi m_g K_B T}} \tag{5.1}$$

where P is the gas pressure, m_g is gas molecular mass, K_B is Boltzmann constant and T is temperature. For all the analysis in this study, we have considered room temperature. It is mentioned in [5.36] that hydrogen adsorption on the Palladium surface is a second-order process. Thus, hydrogen coverage on the surface (θ_S) can be obtained from the second-order Langmuir isotherm as:

$$\theta_S = \frac{\sqrt{\frac{2\psi s_0}{N_s v_d}}\, e^{\frac{\Delta H_d}{2K_B T}}}{\left(1 + \sqrt{\frac{2\psi s_0}{N_s v_d}}\, e^{\frac{\Delta H_d}{2K_B T}}\right)} \tag{5.2}$$

where s_0 is sticking parameter initially, N_s represents adsorption site concentration on the surface, ΔH_d is desorption energy and v_d is a constant. Using the hydrogen coverage on the surface in equation (5.2), we can obtain hydrogen coverage at the interface (θ_I) by solving the following equation as mentioned in [5.52]:

$$\theta_S = \frac{1}{1 + e^{\frac{-(\Delta H_S - \Delta H_I)}{K_B T}} \left(\frac{1}{\theta_I} - 1\right)} \tag{5.3}$$

where ΔH_S and ΔH_I are the heat of adsorption per H atoms on the surface and interface respectively. Now, ΔH_I follows the Tempkin Isotherm [5.52] and it can be expressed as: $\Delta H_I = \Delta H_{I0}(1 - \alpha\theta_I)$. Here, ΔH_{I0} is initial heat of adsorption per H atoms and α can be represented as $\alpha = \frac{q\mu N_i}{\varepsilon \Delta H_{I0}}$, where q is the charge of an electron, μ is the effective dipole constant, N_i is adsorption site concentration at the interface and ε is permittivity. The ultimate change in workfunction of Palladium with hydrogen gas pressure is given by:

$$\Delta WF = -\left(\frac{\theta_I N_i \mu}{\varepsilon}\right) \tag{5.4}$$

To validate this set of equations (5.1-5.4), we have plotted the final work function variation from equation (5.4) with that provided in [5.15] for both Palladium and Platinum (see Figure. 5.2d) and they have an excellent match.

5.4.2. Technology Computer-Aided Design (TCAD) Models:

For simulating the proposed device structure, the SILVACO ATLAS TCAD simulation tool was utilized [5.37]. To consider the Schottky contact, we have considered the finite surface recombination velocity (FSRV) method by mentioning the *surf.rec* command in the contact statement. Moreover, we have incorporated the Universal Schottky Tunneling model (UST) to account for the tunneling of the majority of carriers through the metal-semiconductor interface [5.38]. For mobility,

we have used the Lombardi mobility model (CVT) for incorporating mobility variation with carrier concentrations and electric fields. SRH and AUGER models are also invoked for minority carrier recombination. Band-gap narrowing effect has been considered. For carrier statistics, Fermi-Dirac mode is activated. Lastly, the drift-diffusion model is primarily used to capture the transport mechanism.

For validation, we have calibrated our simulation setup with experimental results [5.50], which are shown in Figure. 5.3b. It can be seen that our simulation models capture the Schottky effect and are in good agreement with the previously reported experimental results. This adds confidence to our TCAD simulation framework.

5.4.3 Crossbar Simulation Model:

The crossbar simulation model comprises two sections: The voltage distribution part and the Current distribution part [5.39]. As the current–voltage characteristics of the two-terminal silicon devices are inherently non-linear, an iterative approach was employed to compute the current through each device within the crossbar array. A look-up table (LUT) was constructed using the device current values obtained from TCAD simulations under various applied bias conditions and different hydrogen gas pressures. This LUT serves as a reference for accurately modelling the current distribution and overall sensing behaviour of the crossbar system. The voltage distribution across the crossbar has been calculated based on the following equation [5.51]:

$$V_{ij} = \frac{1 + \sum_{k=j+1}^{n}\left(G_{ik} * \sum_{i=j+1}^{k}\frac{1}{g_l}\right)}{1 + \sum_{k=1}^{n}\left(G_{ik} * \sum_{i=j+1}^{k}\frac{1}{g_l}\right)} \times (V_{in}\alpha_i) \tag{5.5}$$

where i and j are the row and column indices for a $m\ x\ n$ crossbar array. G_{ij} is the conductance of the two terminal silicon devices at the $(i,j)^{\text{th}}$ grid point while g_l is the interconnect conductance between two adjacent sensor devices. The device currents corresponding to the finally converged voltage distribution are evaluated and plugged into the final output current (I) equation, which is given below:

$$I(i,j) = \beta_j * \sum_i I_{Device_{ij}} \quad (5.6)$$

where I_{Device} is the current obtained from LUT with the final voltage distribution.

It is to be noted that α_i (in equation 5.5) and β_j (in equation 5.6) are row and column-specific sneak path parameters. As mentioned in [5.51], these parameters are estimated from Kirchhoff's law (KCL & KVL) equations with an average conductance of the constituting devices. Although these are approximation parameters, they provide a better computational time advantage while maintaining similar accuracy to traditional Kirchhoff's law.

5.5 Result and Discussion:

A single sensing device geometry has been shown in Fig. 5.3(a). A 10 nm undoped silicon (Si) film has been considered as the conducting material. The total length of the Si film is 25 nm. A charge plasma electrode (CpE) has been included to modulate the carrier concentration in the device. Workfunction of this electrode has been kept fixed at 4 eV throughout the study. Palladium is considered to be the sensing electrode (SE). Based on the pressure of the gas molecules, the work function of this electrode changes which impacts the current conduction. Fig. 5.3(b) shows the calibration results of the TCAD simulation framework with the previously reported experimental results. For understanding the device physics of the single sensing cell, the energy-band diagram is shown in Fig. 5.3(c). For higher work functions of the sensing electrode, it can be seen that the Schottky barrier height is decreasing at the right end. This indicates that in cases with a higher work function, fewer charge carriers participate in current conduction at a given applied bias, resulting in reduced overall current flow through the device. This effect has been reflected in the current-voltage characteristics which are shown in Fig. 5.3(d). For a higher work function of SE, we see that the current reduces and requires a larger voltage to saturate. For comparison, we have provided Table 5.2 which shows the performance of the proposed device in comparison to previously reported data.

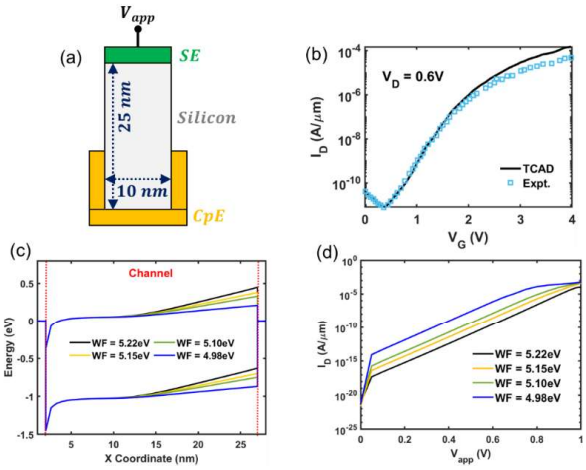

Fig 5.3. Single device characterization: *(a) Schematic of the dual-electrode (sensing electrode (SE) & charge-plasma electrode (CpE)) silicon film (b) Calibration results of the TCAD simulation framework with previously reported experimental results [5.50] neuro (c) Energy band diagrams and (d) Current-voltage characteristics of the proposed device for different SE workfunctions.*

One of the most important parameters to analyze for a crossbar array is the voltage distribution. In Figure 5.4, we have shown the voltage distribution study of the proposed crossbar sensor system for various conditions. Normalized voltage variation is shown in Fig. 5.4(a-c) which is calculated by

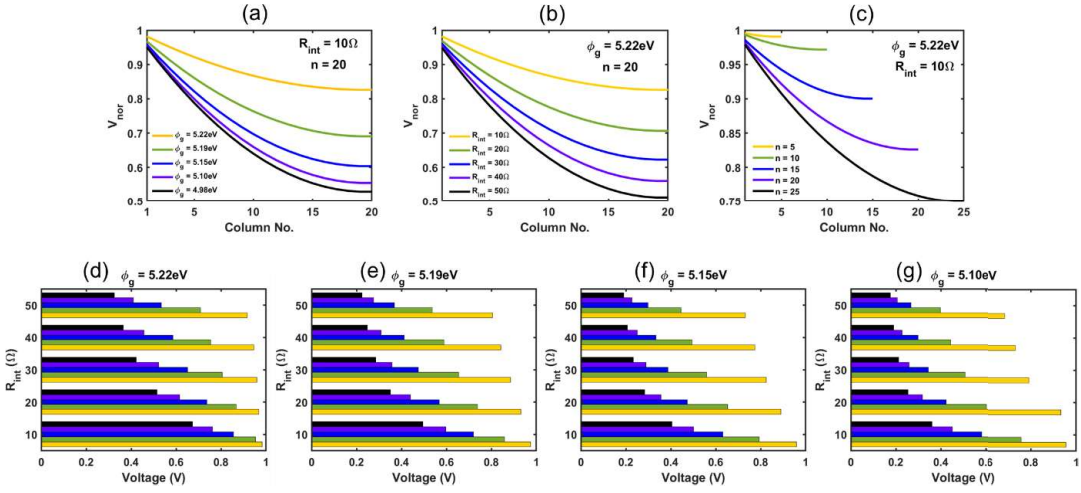

Fig 5.4. Voltage distribution: *Normalized voltages are plotted for (a) different sensing electrode workfunctions at interconnect resistance (R_{int}) of 10Ω and array number (n) of 20. (b) different interconnect resistances at pristine sensing electrode (ϕ_g = 5.22 eV) and array number (n) of 20. (c) different array numbers at interconnect resistance (R_{int}) of 10Ω and the pristine sensing electrode. Mean array voltages for different interconnect resistances with sensing electrode workfunction of (d) 5.22 eV (e) 5.19 eV (f) 5.15 eV (g) 5.10 eV. It is to be noted that in (d-g) yellow, green, blue, violet, and black coloured bars represent the cases with array sizes of 5×5, 10×10, 15×15, 20×20, and 25×25 respectively. Array number (n) means an array size of (n × n) has been considered.*

Table 5.1. *Mean currents for different* (R_{int}, ϕ_g *and* $Array\ size$)

		Array Size			
		10 × 10		20 × 20	
R_{int} (Ω)	10	0.4994	0.1018	0.0130	0.0040
		0.0637	0.1105	0.0040	0.0081
	20	0.0181	0.0033	0.0011	0.0005
		0.0025	0.0046	0.0007	0.0018
	30	0.0038	0.0007	0.0003	0.0002
		0.0006	0.0013	0.0003	0.0011

.($\phi_g = 5.22\ eV$ $\phi_g = 5.19\ eV$ $\phi_g = 5.15\ eV$ $\phi_g = 5.10\ eV$)

normalizing the voltage along a row with the input voltage of that row. It can be seen that for a fixed interconnect resistance (R_{int}=10Ω) and array number (n=20), the normalized voltage decreases with a decrease in sensing electrode work function (ϕ_g) (see Fig. 5.4(a)). In other words, higher gas pressure leads to a decrease in the normalized voltage of the proposed system. The reason can be attributed to the higher conductance of the sensing cells at a lower sensing electrode work function as can be seen from Fig. 5.3(d). Since lower normalized voltage is associated with higher sneak paths in the crossbar array, we can conclude that at higher gas pressure the array will be more prone to sneak path issues. Keeping ϕ_g constant at 5.22 eV (pristine condition) and n = 20, when interconnect resistances are varied from 10Ω to 50Ω, the normalized voltage is found to decrease (see Fig. 5.4(b)). Quantitively, along the 20th column, the normalized voltage has reduced by 37.8% for R_{int} = 50Ω in comparison to R_{int} = 10Ω case. Similar analysis has been done for different array sizes as well while keeping R_{int}, ϕ_g constant at 10Ω & 5.22 eV respectively. A higher array size leads to more paths for sneak current flow in the crossbar which will lead to lesser normalized voltage. This trend has been captured in Fig. 5.4(c). Another key figure of merit for the crossbar architecture is the mean voltage across the array. This parameter represents the average potential difference experienced by the individual devices within the crossbar and provides insights into the uniformity of bias distribution, power consumption, and overall sensing efficiency of the system.

From the mean voltages plotted in Fig. 5.4(d-g), we can deduce several trends which are crucial in understanding the proposed sensor system. Firstly, for every sensing electrode work function, we see that mean voltage decreases with higher interconnect resistance (a trend that has been seen in normalized voltages as well). The impact of 113ntercomnect resistance increases with a decrease in ϕ_g as the array becomes more prone to sneak currents in higher ϕ_g condition. Secondly, we can notice mean voltages decrease at higher sensing electrode work functions (ϕ_g). Thirdly, mean voltages are higher for smaller array sizes, for instance, the yellow bars (array size of 5×5) in Fig. 5.4(d-g) are always higher than black bars (25×25) for every interconnect resistance and sensing electrode work function. For smaller array sizes, the IR drop across the crossbar reduces considerably, and thus the voltages across all the nodes increase. Moreover, the sneak paths increase in a larger array which contributes to the lowering of node voltages in a crossbar. These trends will help us to better understand the current distribution in the crossbar in subsequent sections.

Figure 5.5 exhibits the current distribution in the crossbar array for different interconnect resistances, sensing electrode work functions, and array sizes. From all

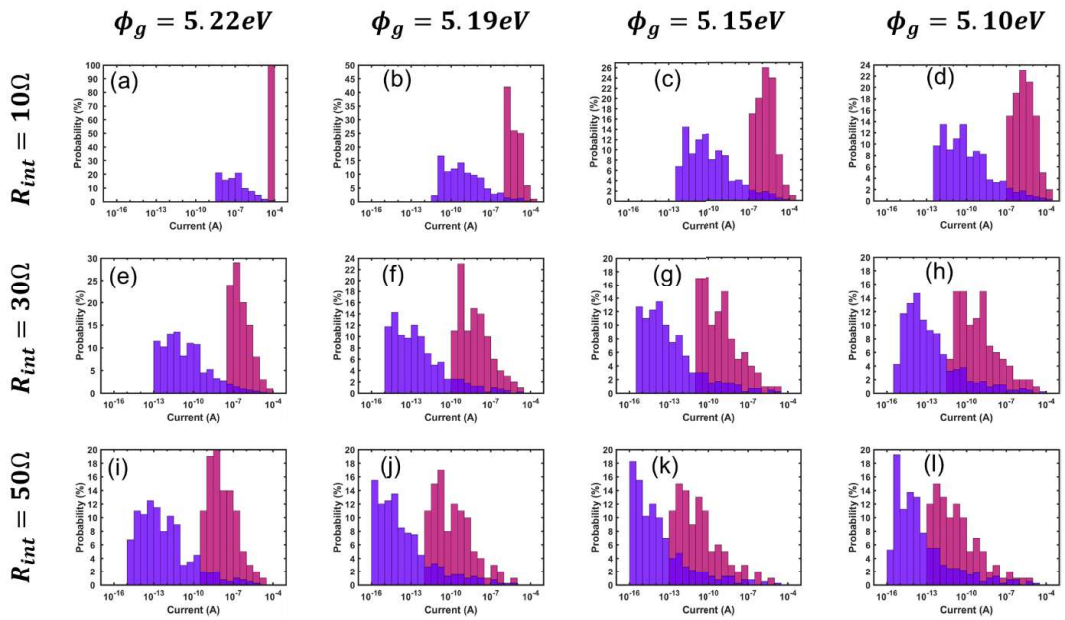

Fig 5.5. Current histograms: *(a-l) Current distribution in the crossbar sensor system for different interconnect resistances (R_{int}) and sensing electrode workfunctions (ϕ_g). In all these histogram plots, pink bars are for a 10×10 array and purple ones are for a 20×20 array.*

of the distributions, it can be noticed that the spread of the current histogram increases with the array size. A higher spread of current histogram leads to overlapping of current levels for a certain sensing electrode work function with that of the pristine condition. For lower ϕ_g, the current distribution is observed to spread more due to the higher conductance of the sensing electrode. This can be better understood from the node voltage distribution which is discussed in the previous section. Quantitively, it has been found that the mean current values for ϕ_g = 5.22 eV, 5.19 eV, and 5.15 eV in a 10×10 array setup with $R_{int} = 10\Omega$ are 0.5×10^{-4} A, 0.1×10^{-4} A and 0.06×10^{-4} A respectively. In other words, there is a reduction of 80% and 88% in mean currents for cases ϕ_g = 5.19 eV & 5.15 eV w.r.t. pristine condition (ϕ_g = 5.22 eV). For the cases with $R_{int} = 20\Omega$ and $R_{int} = 30\Omega$, the reduction percentages slow down to 86% and 82% for ϕ_g = 5.15 eV. In a 20×20 array setup, the mean currents are always lower for all ϕ_g as can be seen in Table 5.1. We can capture two general trends from Table 5.1: (1) With an increase in R_{int}, mean current decreases, and (2) With an increase in array size, mean

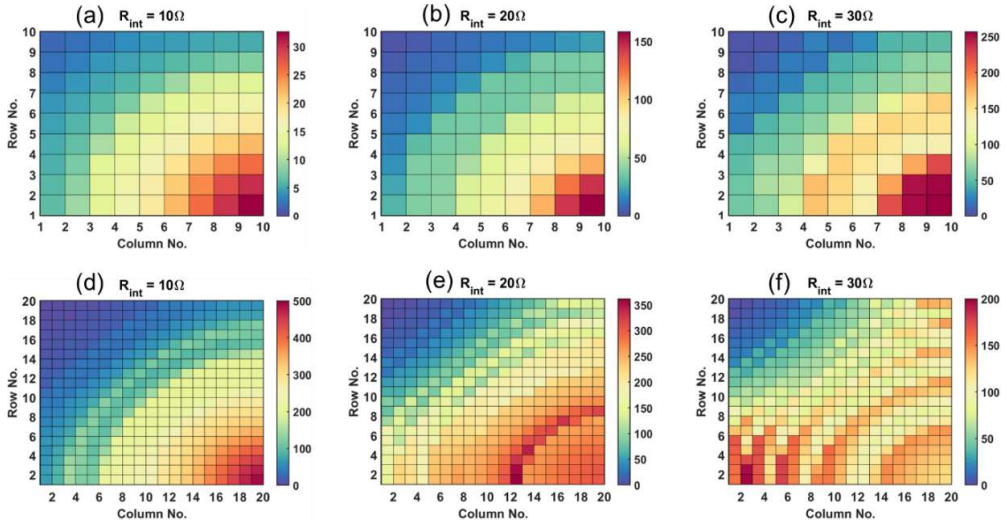

Fig 5.6. Sensitivity heatmaps: *Sensitivity heatmaps are shown for very low-pressure condition ($\phi_g = 5.19\ eV$) in (a-c) 10x10 array and (d-f) 20×20 array setups with interconnect resistance (R_{int}) of (a,d) 10Ω, (b,e) 20Ω and (c,f) 30Ω. The colour bars on the right of each plot show sensitivity values.*

current decreases for all ϕ_g. These are implied in the voltage distribution as well. However, a counterintuitive observation can be made by looking at the mean current variation with the reduction in ϕ_g. From previous discussions, we can understand that with a lower ϕ_g, the conductance of the sensing cell increases which leads to more voltage degradation in the crossbar. This should lead to a lower mean current but we can notice in Table 5.1, the mean current is higher for ϕ_g = 5.10 eV in comparison to ϕ_g = 5.15 eV & 5.19 eV cases. Furthermore, the mean current in ϕ_g = 5.15 eV is equal to that in ϕ_g = 5.19 eV for $R_{int} = 10\Omega$ and even higher than the later for $R_{int} = 20\Omega \,\&\, 30\Omega$. In the crossbar, two different processes are operating which results in above mentioned counterintuitive observations. First, lower ϕ_g will lead to a higher voltage drop. Secondly, cell conductance increases with lower ϕ_g. Now, the mean current for lower ϕ_g can be higher than that of higher ϕ_g when the current corresponding to the lower node voltage for low ϕ_g the case is greater than the current corresponding to higher node voltage in high ϕ_g cases. Next, we have chosen two cases to explain this phenomenon: (i) *array size of 10×10 with* $R_{int} = 10\Omega$ – the mean voltages for ϕ_g = 5.15 eV & 5.10 eV are 0.79V and 0.757V respectively (see Figure 5.4). The corresponding current values for these voltages are obtained as $1 \times 10^{-6}\ A$ and $3 \times 10^{-6}\ A$ (from Figure 5.3(d)). (ii) *array size of 20×20 with* $R_{int} = 30\Omega$ – the mean voltages for ϕ_g = 5.15 eV & 5.10 eV are 0.29V and 0.26V respectively (see Figure 5.4). The corresponding current values for these voltages are obtained as $1 \times 10^{-13}\ A$ and $1.4 \times 10^{-13}\ A$ (from Figure 5.3(d)). From the above two cases, we see that average voltage reduces for lower ϕ_g but the current increases. These variations have a significant impact on system sensitivity and provide design guidelines for the proposed sensor system which are discussed in the next section.

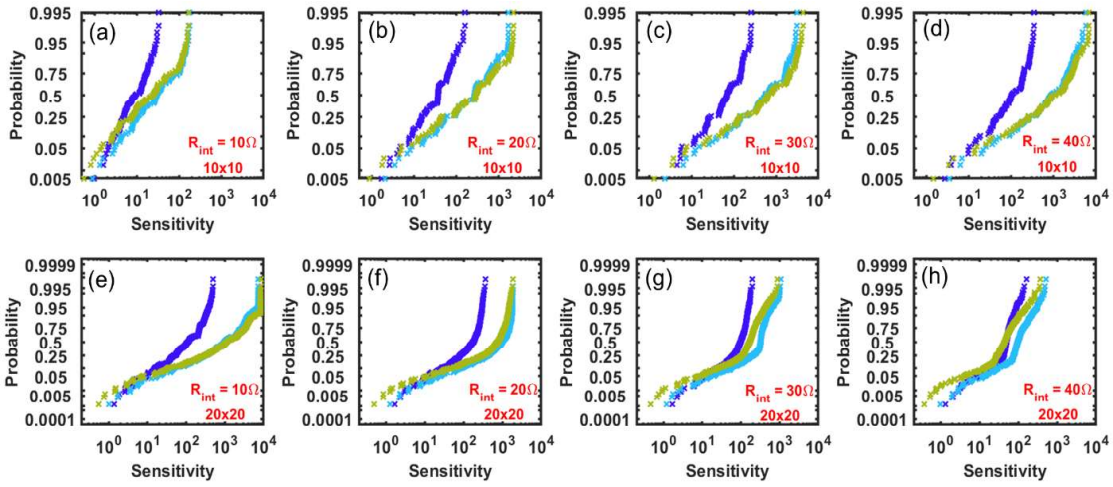

Fig 5.7. Probability distribution: *The sensitivity metric distribution of all sensors in the proposed crossbar architecture in (a-d) 10×10 array and (e-h) 20×20 array with interconnect resistance varied from 10Ω to 40Ω in steps of 10Ω. The dark blue, sky blue, and green curves are for* ϕ_a *= 5.19 eV, 5.15 eV and 5.10 eV respectively*

In this work, the sensitivity metric at every junction of the crossbar has been calculated as the ratio of current flowing through the sensing device at the junction without gas condition to that with gas condition ($\frac{I_{no\ gas}}{I_{gas}}$).

Figure 5.6 shows the spatial variation of sensitivity metric for different interconnect resistances of (a,d) 10Ω, (b,e) 20Ω and (c,f) 30Ω in a 10×10 (a-c) & 20×20 (d-f) array setups. It is to be noted that Figure 5.6 is for the sensitivity of the proposed sensor system at ϕ_g = 5.19 eV. For a particular interconnect resistance, the sensitivity increases with an increase in array size. With a larger array, the voltage distribution becomes more distinct for different gas pressures. This leads to higher fluctuations of the currents and subsequently sensitivity increases. As we move from lower to higher interconnect resistance cases for a particular array size, we see that the sensitivity increases for a 10×10 array but for a 20×20 array, it reduces. The reason can be attributed to lower crossbar currents for the pristine condition at a higher array size due to larger voltage distortion. The currents at no gas condition decrease faster than that with a gas condition, and the sensitivity metric reduces, and that trend can be observed in Figure 5.6(d-f). While for the 10×10 array, the no gas condition currents do not drop so much. Thus, we see the sensitivity increase in this case. Furthermore, the spatial variation shows that the sensitivity is lower along starting columns in comparison to the later ones. For optimizing the crossbar

metrics, a statistical analysis has been done based on the sensitivity metric distributions with different crossbar parameters which are interconnect resistances and array sizes.

The distribution plots in Figure 5.7 help us to understand the pattern of sensitivity distribution in a crossbar architecture for different parametric conditions. For instance, in a 10×10 array setup (Figure 5.7(a-d)), the peak sensitivity increases for all the gas pressures. The reverse trend can be observed for the 20x20 array setup (Figure 5.7(e-h)). In a 20×20 array, with an increase in interconnect resistances, the distributions for ϕ_g = 5.15eV & 5.10 eV shift leftward meaning the sensitivity decreases. The curve for ϕ_g = 5.19 eV also moves towards the left but the rate of change is small in comparison to the other two cases. It can be noticed that for R_{int} = 20 to 40Ω, the probability of lower sensitivity is higher for ϕ_g = 5.10 eV in comparison to that for ϕ_g = 5.15 eV. In the 10×10 array condition, we can observe a monotonous trend for sensitivity in all gas pressures. It is to be noted that although the probability distribution overlap between two gas pressure conditions, the spatial distribution or sensitivity pattern is unique in each condition (this can be seen in Figure 5.6). Hence, for the proposed crossbar system, we have to characterize the sensitivity in two ways: (i) *peak sensitivity* and (ii) *sensitivity spatial variation.* Considerable peak sensitivity difference between different gas pressure conditions along with uniqueness in the spatial distribution of sensitivity metric is the ideal combination. Accounting these two factors into consideration, we can conclude that a lower array size ($\leq 10 \times 10$) with interconnecting resistance between 20-50Ω can be seen as an optimal solution.

TABLE 5.2: Comparison between the scaling effect on sensitivity in our work and that of previously reported studies

References	Transport Mode	Channel Dimensions		Drain Current (I_D) Sensitivity
		Length (l_g) (nm)	Thickness (t_{CH}) (nm)	
Silicon MOSFET [5.53]	DD	50	20	2.08 ($\Delta WF = 50\ meV$) 4.56 ($\Delta WF = 100\ meV$)
GAA Silicon FET [5.53]	DD	20	20 (diameter)	5.96 ($\Delta WF = 50\ meV$) 33.1 ($\Delta WF = 100\ meV$)
JL GAA Silicon FET [5.54]	DD	40	10 (diameter)	7.17 ($\Delta WF = 50\ meV$) 38.80 ($\Delta WF = 100\ meV$)
Silicon CG-NWFET [5.55]	DD	50	10 (diameter)	7.08 ($\Delta WF = 50\ meV$) 37.26 ($\Delta WF = 100\ meV$)
InGaAs CG-NWFET [5.55]	DD	50	10 (diameter)	7.30 ($\Delta WF = 50\ meV$) 40.51 ($\Delta WF = 100\ meV$)
GAA NW JL FET [5.17]	DD	50	12 (diameter)	12 ($\Delta WF = 50\ meV$) 38 ($\Delta WF = 100\ meV$)
JL FinFET [5.19]	DD	50	$H_{fin} = 40$ $T_{fin} = 15$	1.4 ($\Delta WF = 50\ meV$) 4.95 ($\Delta WF = 100\ meV$)
Our Work	**DD**	**25**	**10**	**~ 10 ($\Delta WF = 50\ meV$)** **~ 50 ($\Delta WF = 100\ meV$)**

References:

[5.1] Hong, S.; Wu, M.; Hong, Y.; Jeong, Y.; Jung, G.; Shin, W.; Park, J.; Kim, D.; Jang, D.; Lee, J.H. FET-type gas sensors: A review. Sens.Actuators B Chem. 2021, 330, 129240.

[5.2] Dai, J.; Ogbeide, O.; Macadam, N.; Sun, Q.; Yu,W.; Li, Y.; Su, B.L.; Hasan, T.; Huang, X.; Huang,W. Printed gas sensors. Chem. Soc. Rev. 2020, 49, 1756–1789.

[5.3] Majhi, S.M.; Mirzaei, A.; Kim, H.W.; Kim, S.S.; Kim, T.W. Recent advances in energy-saving chemiresistive gas sensors: A review. Nano Energy 2021, 79, 105369.

[5.4] Bag, A.; Lee, N.E. Gas sensing with heterostructures based on two-dimensional nanostructured materials: A review. J. Mater. Chem. C 2019, 7, 13367–13383.

[5.5] Akbari-Saatlu, M.; Procek, M.; Mattsson, C.; Thungström, G.; Nilsson, H.E.; Xiong, W.; Xu, B.; Li, Y.; Radamson, H.H. Silicon nanowires for gas sensing: A review. Nanomaterials 2020, 10, 2215.

[5.6] Axelsson, L.; Franzén, M.; Ostwald, M.; Berndes, G.; Lakshmi, G.; Ravindranath, N.H. Perspective: Jatropha cultivation in southern India: Assessing farmers' experiences. Biofuels Bioprod. Biorefining 2012, 6, 246–256.

[5.7] Hosseini, S.E.;Wahid, M.A. Hydrogen production from renewable and sustainable energy resources: Promising green energy carrier for clean development. Renew. Sustain. Energy Rev. 2016, 57, 850–866.

[5.8] Verhelst, S.;Wallner, T. Hydrogen-fueled internal combustion engines. Prog. Energy Combust. Sci. 2009, 35, 490–527.

[5.9] Chitragar, P.R.; Shivaprasad, K.V.; Nayak, V.; Bedar, P.; Kumar, G.N. An experimental study on combustion and emission analysis of four cylinder 4-stroke gasoline engine using pure hydrogen and LPG at idle condition. Energy Procedia 2016, 90, 525–534.

[5.10] Das, L.M. Hydrogen-fueled internal combustion engines. Compend. Hydrog. Energy 2016, 3, 177–217.

[5.11] Liu, F.S.; Hao, L.J.; Heitz, P.B. Technical status quo and development prospect of hydrogen IC engine. Automot. Eng. 2006, 28, 621–625.

[5.12] Kim, S.-e.; Lee, K.; Kang, C.; Jung, S. Tracer Gas Test and CFD Analysis of Semiconductor Gas Box for Flammable Gas Leakage. Energies 2022, 15, 8166. https://doi.org/10.3390/en15218166

[5.13] Lundström, S. Shivaraman, C. Svensson, and L. Lundkvist, "A hydrogen–sensitive MOS field–effect transistor", Appl. Phys. Lett. 26, 55 (1975); https://doi.org/10.1063/1.88053

[5.14] M Gholizadeh, M Safari Hasanabadi, A. Salehi, "Modelling and simulation of MOSFET gas sensor with platinum gate for hydrogen detection", Sensors and Actuators B141 (2009).1-6

[5.15] Sarkar, Deblina & Banerjee, Kaustav. (2012). Proposal for tunnel-field-effect-transistor as ultra-sensitive and label-free biosensors. Applied Physics Letters. 100. 10.1063/1.3698093.

[5.16] Jaya Madan, Rishu Chaujar, 'Palladium Gate All Around - Hetero Dielectric -Tunnel FET based highly sensitive Hydrogen Gas Sensor' , https://doi.org/10.1016/j.spmi.2016.09.050

[5.17] S. Mokkapati, N. Jaiswal, M. Gupta and A. Kranti, "Gate-All-Around Nanowire Junctionless Transistor-Based Hydrogen Gas Sensor," in IEEE Sensors Journal, vol. 19, no. 13, pp. 4758-4764, 1 July1, 2019, doi: 10.1109/JSEN.2019.2903216.

[5.18] Pratap, Y., Kumar, M., Kabra, S. *et al.* Analytical modeling of gate-all-around junctionless transistor based biosensors for detection of neutral biomolecule species. *J Comput Electron* 17, 288–296 (2018). https://doi.org/10.1007/s10825-017-1041-4

[5.19] H. D. Sehgal, Y. Pratap, M. Gupta, S. Kabra and P. Pal, "Comparative Analysis of Junctionless FinFET and Inverted Mode FinFET as Phosphine (PH3) Gas Sensor," 2020 5th International Conference on Devices, Circuits and Systems (ICDCS), 2020, pp. 193-197, doi: 10.1109/ICDCS48716.2020.243579.

[5.20] Kumar, Ajay. (2020). Palladium-based trench gate MOSFET for highly sensitive hydrogen gas sensor. Materials Science in Semiconductor Processing. 120. 105274. 10.1016/j.mssp.2020.105274.

[5.21] Rani, A.; DiCamillo, K.; Khan, M.A.H.; Paranjape, M.; Zaghloul, M.E. Tuning the Polarity of $MoTe_2$ FETs by Varying the Channel Thickness for Gas-Sensing Applications. *Sensors* 2019, *19*, 2551. https://doi.org/10.3390/s19112551

[5.22] Chachuli, Siti & Hamidon, Mohd Nizar & Mamat, Shuhazlly & Ertuğrul, Mehmet & Abdullah, Nor. (2018). A Hydrogen Gas Sensor Based on TiO2 Nanoparticles on Alumina Substrate. Sensors. 18. 2483. 10.3390/s18082483.

[5.23] Hubert, T.; Boon-Brett, L.; Black, G.; Banach, U. Hydrogen sensors—A review. Sens. Actuators B Chem. 2011, 157, 329–352.

[5.24] Padma, R. & Lakshmi, Prasanna & Reddy, M. & Rajagopal Reddy, Varra. (2013). Electrical and structural properties of Ir/Ru Schottky rectifiers on n-type InGaN at different annealing temperatures. Superlattices and Microstructures. 56. 64–76. 10.1016/j.spmi.2012.12.016.

[5.25] Chao Liu, Yulong Zhang, Jiaxin Wu, Hailu Dai, Chengjian Ma, Qinfang Zhang, Zhigang Zou, Ag-Pd alloy decorated ZnIn2S4 microspheres with optimal Schottky barrier height for boosting visible-light-driven hydrogen evolution, Journal of Materials Science & Technology, Volume 114, 2022, Pages 81-89, ISSN 1005-0302, https://doi.org/10.1016/j.jmst.2021.12.003.

[5.26] Zhang, X., Liu, B., Gao, L. *et al.* Near-ideal van der Waals rectifiers based on all-two-dimensional Schottky junctions. *Nat Commun* 12, 1522 (2021). https://doi.org/10.1038/s41467-021-21861-6

[5.27] Adeyemo, A., Mathew, J., Jabir, A. *et al.* Efficient sensing approaches for high-density memristor sensor array. *J Comput Electron* 17, 1285–1296 (2018). https://doi.org/10.1007/s10825-018-1176-y

[5.28] Fine, G.F., et al.: Metal oxide semi-conductor gas sensors in environmental monitoring. Sensors 10(6), 5469–5502 (2010)

[5.29] Fujishima, A., Rao, T.N., Tryk, D.A.: Titanium dioxide photocatalysis. J. Photochem. Photobiol. C 1(1), 1–21 (2000)

[5.30] Garzella, C., Comini, E., Tempesti, E., Frigeri, C., Sberveglieri, G.: TiO_2 thin films by a novel sol–gel processing for gas sensor applications. Sens. Actuators B: Chem. 68(1), 189–196 (2000)

[5.31] Long, Zhenghao & Xu, Xiaojie & Yang, Wei & Hu, Mingxiang & Shtansky, Dmitry & Golberg, Dmitri & Fang, Xiaosheng. (2019). Cross-Bar SnO2-NiO Nanofiber-Array-Based Transparent Photodetectors with High Detectivity. Advanced Electronic Materials. 6. 10.1002/aelm.201901048.

[5.32] Fahad, H.M.; Shiraki, H.; Amani, M.; Zhang, C.; Hebbar, V.S.; Gao,W.; Ota, H.; Hettick, M.; Kiriya, D.; Chen, Y.Z.; et al. Room temperature multiplexed gas sensing using chemical-sensitive 3.5-nm-thin silicon transistors. Sci. Adv. 2017, 3, e1602557.

[5.33] Banerjee, A.; Khan, S.U.H.; Broadbent, S.; Bulbul, A.; Kim, K.H.; Noh, S.; Looper, R.; Mastrangelo, C.H.; Kim, H. Molecular bridge-mediated ultralow-power gas sensing. Microsyst. Nanoeng. 2021, 7, 1–11.

[5.34] Chen, Ying-Chen & Lin, Chao-Cheng & Chang, Yao-Feng. (2021). Post-Moore Memory Technology: Sneak Path Current (SPC) Phenomena on RRAM Crossbar Array and Solutions. Micromachines. 12. 50. 10.3390/mi12010050.

[5.35] Mohammadi MM, Kumar A, Liu J, Liu Y, Thundat T, Swihart MT. Hydrogen Sensing at Room Temperature Using Flame-Synthesized Palladium-Decorated Crumpled Reduced Graphene Oxide Nanocomposites. ACS Sens. 2020 Aug 28;5(8):2344-2350. doi: 10.1021/acssensors.0c01040. Epub 2020 Aug 17. PMID: 32786377.

[5.36] Johansson, M. & Skúlason, Egill & Nielsen, Gunver & Murphy, Shane & Nielsen, R.M. & Chorkendorff, Ib. (2010). Hydrogen adsorption on palladium and palladium hydride at 1bar. Surface Science. 604. 718-729. 10.1016/j.susc.2010.01.023.

[5.37] https://www.eng.buffalo.edu/~wie/silvaco/atlas_user_manual.pdf

[5.38] Bashir, Faisal & Alharbi, Abdullah & Loan, Sajad. (2017). Electrostatically doped DSL schottky barrier MOSFET on SOI for low power applications. IEEE Journal of the Electron Devices Society. PP. 1-1. 10.1109/JEDS.2017.2762902.

[5.39] Tang, Zhensen & Wang, Yao & Chi, Yaqing & Fang, Liang. (2018). Comprehensive Sensing Current Analysis and Its Guideline for the Worst-Case Scenario of RRAM Read Operation. Electronics. 7. 224. 10.3390/electronics7100224.

[5.40] M. E. Fouda, A. M. Eltawil and F. Kurdahi, "Modeling and Analysis of Passive Switching Crossbar Arrays," in IEEE Transactions on Circuits and Systems I: Regular Papers, vol. 65, no. 1, pp. 270-282, Jan. 2018, doi: 10.1109/TCSI.2017.2714101.

[5.41] Minhee Yun, Nosang V. Myung, Richard P. Vasquez, Choonsup Lee, Erik Menke, and Reginald M. Penner ,"Electrochemically Grown Wires for Individually

Addressable Sensor Arrays"Nano Letters 2004 4 (3), 419-422 DOI: 10.1021/nl035069u.

[5.42] B. Zhang, Y.-Y. Weng, X.-P. Huang, M. Wang, R.-W. Peng, N.-B. Ming, B. Yang, N. Lu, and L. Chi, "Creating in-plane metallic-nanowire arrays by corner-mediated electro deposition," Adv. Mater. 21, 3576–3580 (2009). https://doi.org/10.1002/adma.200900730 , Google Scholar Crossref, ISI

[5.43] Chou, S.Y., Krauss, P.R. and Renstrom, P.J. (1996) Imprint Lithography with 25-Nanometer Resolution. Science, 272, 85-87. http://dx.doi.org/10.1126/science.272.5258.85.

[5.44] Yue, F.; Ngin, T. S.; Hailin, G. Sensors and Actuators B1996, 32, 33.

[5.45] Sawsan M.S. Haggag, A.A.M. Farag, Mohamed E. Mahmoud,Layer-by-layer chemical deposition technique for thin film assembly of deposited nano-sized magnesium(II)–5,7-dinitro-8-hydroxyquinolate: Characterization and spectral–optical–electrical properties, Polyhedron, Volume 30, Issue 16,2011, Pages 2723-2732. https://doi.org/10.1016/j.poly.2011.08.002.

[5.46] Shujun Ye, Kikuo Yamabe, Tetsuo Endoh,Precise fabrication of uniform sub-10-nm-diameter cylindrical silicon nanopillars via oxidation control", Volume 198,ISSN 1359-6462, https://doi.org/10.1016/j.scriptamat.2021.113818.

[5.47] Stocker, M., Li, L., Gattass, R. et al. Multiphoton photoresists giving nanoscale resolution that is inversely dependent on exposure time. Nature Chem 3, 223–227 (2011). https://doi.org/10.1038/nchem.965.

[5.48] Daniel Amkreutz,Natalie Preissler,Cham Thi-Trinh,Martina Trahms,Paul Sonntag,Rutger, Schlatmann,Bernd Rech," Influence of the precursor layer composition and deposition processes on the electronic quality of liquid phase crystallized silicon absorbers". https://doi.org/10.1002/pip.2953

[5.49] Yan, X. J.; Xiong, H. Y.; Bai, Q. G.; Frenzel, J.; Si, C. H.; Chen, X. T.; Eggeler, G.; Zhang, Z. H. Atomic layer-bylayer construction of Pd on nanoporous gold via underpotential deposition and displacement reaction. RSC Adv. 2015, 5, 19409–19417.

[5.50] R. Jhaveri, V. Nagavarapu and J. C. S. Woo, "Asymmetric Schottky Tunneling Source SOI MOSFET Design for Mixed-Mode Applications," in IEEE Transactions on Electron Devices, vol. 56, no. 1, pp. 93-99, Jan. 2009, doi: 10.1109/TED.2008.2008161.

[5.51] Y. Liao et al., "A Compact Model of Analog RRAM With Device and Array Nonideal Effects for Neuromorphic Systems," in IEEE Transactions on Electron Devices, vol. 67, no. 4, pp. 1593-1599, April 2020, doi: 10.1109/TED.2020.2975314.

[5.52] Lars-Gunnar Ekedahl, Mats Eriksson, and Ingemar Lundström Accounts of Chemical Research 1998 31 (5), 249-256 DOI: 10.1021/ar970068s

[5.53] R. Gautam, M. Saxena, R. S. Gupta and M. Gupta, "Gate-All-Around Nanowire MOSFET With Catalytic Metal Gate For Gas Sensing Applications," in IEEE Transactions on Nanotechnology, vol. 12, no. 6, pp. 939-944, Nov. 2013, doi: 10.1109/TNANO.2013.2276394

[5.54] Chaujar, R., Yirak, M.G. Sensitivity Investigation of Junctionless Gate-all-around Silicon Nanowire Field-Effect Transistor-Based Hydrogen Gas Sensor. Silicon 15, 609–621 (2023). https://doi.org/10.1007/s12633-022-02242-0

[5.55] N.K. Singh, A. Raman, S. Singh, N. Kumar, A novel high mobility In1-xGaxAs cylindrical-gate-nanowire FET for gas sensing application with enhanced sensitivity, Superlattices and Microstructures (2017), doi: 10.1016/j.spmi.2017.07.001

[5.56] I. Lundström, M. Shivaraman, C. Svensson, and L. Lundkvist, "A hydrogen-sensitive Pd-gate MOS transistor," *Appl. Phys. Lett.*, vol. 26, no. 2, pp. 55–57, 1975.

[5.57] L. Safari, M. Mojarradi, and H. R. Zare, "Modeling of platinum-gated SOI MOSFET as hydrogen gas sensor," *IEEE Sens. J.*, vol. 8, no. 12, pp. 2038–2044, 2008.

[5.58] S. Sarkar and K. Banerjee, "A tunnel field-effect transistor (TFET)-based hydrogen sensor with enhanced sensitivity," *IEEE Trans. Electron Devices*, vol. 59, no. 4, pp. 962–969, 2012.

[5.59] R. Madan and R. Chaujar, "Hetero-dielectric double-gate TFET hydrogen gas sensor," *Superlattices Microstruct.*, vol. 94, pp. 123–133, 2016.

[5.60] R. Chaujar and A. Madan, "Junctionless FinFET hydrogen gas sensor: modeling and performance analysis," *J. Comput. Electron.*, vol. 15, no. 4, pp. 1217–1225, 2016.

[5.61] N. Barsan and U. Weimar, "Conduction model of metal oxide gas sensors," *J. Electroceram.*, vol. 7, pp. 143–167, 2001.

[5.62] C. Wang, L. Yin, L. Zhang, D. Xiang, and R. Gao, "Metal oxide gas sensors: sensitivity and influencing factors," *Sensors*, vol. 10, no. 3, pp. 2088–2106, 2010.

[5.63] K. I. Gaskell, P. C. Ricci, and M. L. Hitchman, "Hydrogen detection using Pd–Ag thin films," *Thin Solid Films*, vol. 515, no. 14, pp. 5684–5688, 2007.

[5.64] T. Hübert, L. Boon-Brett, G. Black, and U. Banach, "Hydrogen sensors – A review," *Sens. Actuators B: Chem.*, vol. 157, no. 2, pp. 329–352, 2011.

[5.65] S. Hüfner and M. B. Fischer, "Hydrogen storage and sensing with Mg–Ni thin films," *J. Alloys Compd.*, vol. 509, pp. S481–S484, 2011.

[5.66] P. C. Collins, K. B. Jinesh, and H. Mizuta, "Gas sensing with nanowire sensor arrays," *Nanotechnology*, vol. 19, p. 215501, 2008.

[5.67] E. Comini, G. Faglia, and G. Sberveglieri, "ZnO nanostructures: Low-temperature growth and gas sensing properties," *Acta Mater.*, vol. 54, no. 2, pp. 379–384, 2006.

[5.68] J. F. Gibbons, W. C. Chien, and S. K. Banerjee, "Crossbar architectures for high-density integration," *Proc. IEEE*, vol. 96, no. 2, pp. 230–247, 2008.

[5.69] K. K. Likharev and D. B. Strukov, "CMOL: Devices, circuits, and architectures," *Proc. IEEE*, vol. 97, no. 10, pp. 1741–1754, 2009.

[5.70] S. Kim, M. Jeong, and J. H. Ahn, "Analysis of sneak path currents in crossbar memory arrays and mitigation techniques," *IEEE Electron Device Lett.*, vol. 31, no. 5, pp. 503–505, 2010.

[5.71] A. Jana, K. Kumari, B. Gupta, and S. K. Sarkar, "A crossbar architecture-based system (CAS) as hydrogen gas sensing platform," *Nanotechnology*, vol. 35, no. 1, p. 015501, 2024.

Chapter 6

Graded SiGe Channel Dielectric Modulated Tunnel FET Bio Sensor: Proposal and Comparative Analysis

6.1 Introduction

In recent years, the demand for high-performance biosensors has grown significantly, driven by the need for sensitive and reliable detection methods in healthcare, environmental monitoring, and food safety. Researchers have been exploring innovative device architectures and materials to enhance sensor performance. Biosensors can be classified based on their transduction mechanisms, including electrochemical biosensors (e.g., genic sensors), electronic biosensors (such as various FETs like MOSFETs, ISFETs, and TFETs), and gravimetric biosensors (thermal and acoustic sensors) [6.1]. Among these, electronic biosensors stand out for their established fabrication technologies, CMOS compatibility, and integrability with standard ICs. Field-Effect Transistors (FETs) are particularly attractive for label-free detection due to their scalability, cost-effectiveness, and ability to integrate sensors and measurement systems on a chip [6.2-6.3].

Tunnel Field-Effect Transistors (TFETs) are promising candidates for biosensors, offering advantages like lower subthreshold swing (SS), reduced ambipolar characteristics, and high sensitivity through tunneling mechanisms [6.4-6.8]. Scaling to sub-10 nm demands alternative channel, source, and pocket materials to meet IRDS drive current limits [6.9]. Germanium (Ge), with its low bandgap and high hole mobility, is a strong candidate [6.10-6.11]. As a pseudo-direct bandgap

material, Ge offers enhanced band-to-band tunneling (BTBT) efficiency compared to Si [6.12]. Kim et al. demonstrated that Si-Ge-Si TFETs outperform Si-Si-Si and Ge-Ge-Ge counterparts due to optimized tunneling resistance and reduced ambipolarity at the Ge/Si heterojunctions [6.13]. However, pure Ge-based devices face challenges such as lattice mismatch with Si and integration complexities [6.14].

Graded SiGe channels address these challenges by maximizing transconductance and improving performance [6.15]. Early SiGe FETs with SiO_2 insulation and $TiSi_2$ Schottky gates mitigated gate leakage and enhanced hole mobility through spacer layers [6.16]. Advances like hybrid SiGe-channel CMOS and SiGe-based FINFETs achieved high speeds and scalability for 10 nm nodes [6.17-6.18]. $Si_{0.8}Ge_{0.2}$ and $Si_{0.5}Ge_{0.5}$ graded channels demonstrated improved ON currents, reduced OFF currents, and better SS compared to Si-based devices [6.19-6.20]. However, vertical grading faces limitations in scalability and stability, constrained by critical layer thickness and defect formation [6.15,6.21-6.22]. Recently, Lee et al. fabricated a CMOS-compatible gate-all-around SiGe TFET with high Ge content ($Si_{0.2}Ge_{0.8}$) and achieved remarkable SS and low leakage current [6.23].

To overcome performance degradation from defects and ambipolarity, this study proposes a Graded SiGe Tunnel Field-Effect Transistor (Gr.SiGe-TFET) biosensor. By incorporating graded SiGe layers in a Ge-SiGe-Si configuration, the structure addresses key TFET challenges, ensuring high sensitivity and stable performance. Shih et al. showed graded Si/Ge TFETs optimize tunneling barriers for ON/OFF switching and suppress short-channel effects in sub-10 nm devices, but scaling challenges persist with ambipolarity [6.24]. This study proposes an ultrathin biosensor using a Gr.SiGe-TFET highlighting its advantages in label-free biomolecule detection.

6.2 Literature Review

6.2.1 Early Developments in Biosensors

The demand for biosensors has steadily increased over the past few decades, with applications spanning healthcare, environmental monitoring, and food safety. Early

biosensors were based on electrochemical principles, capable of detecting enzymatic or molecular interactions by converting chemical reactions into electrical signals [6.34]. However, these traditional devices faced challenges in terms of sensitivity, selectivity, and scalability. The advent of semiconductor-based biosensors, particularly those employing field-effect transistors (FETs), marked a significant advancement due to their compatibility with CMOS technology, scalability, and ability to achieve label-free detection [6.35, 6.36].

6.2.2 Emergence of Tunnel Field-Effect Transistors (TFETs) in Biosensing

FET-based biosensors evolved from MOSFETs and ISFETs to more advanced devices that could address the limitations of conventional transistors. In this context, tunnel field-effect transistors (TFETs) emerged as promising biosensing platforms. TFETs offered superior electrostatic control, lower subthreshold swing (SS), and higher sensitivity through band-to-band tunneling (BTBT), making them attractive for detecting biomolecules at ultra-low concentrations [6.37-6.39]. Early analytical models of dielectric-modulated TFET biosensors demonstrated label-free detection of biomolecules by exploiting variations in dielectric permittivity within the sensing cavity [6.38, 6.39]. Kanungo *et al.* later provided comparative performance studies, confirming that TFET-based biosensors outperform short-gate or MOS-based devices in terms of sensitivity [6.40].

6.2.3 SiGe Materials and Graded Channels in Transistor Design

The drive toward sub-10 nm nodes necessitated exploration of alternative channel and source materials. Germanium (Ge) gained attention for its low bandgap and high hole mobility, offering improved tunneling efficiency compared to silicon [6.43, 6.44]. Initial studies showed that Si–Ge–Si heterojunction TFETs outperformed pure Si- or Ge-based structures, as the heterojunction reduced ambipolarity and optimized tunneling resistance [6.45, 6.46]. However, lattice mismatch and integration challenges limited the practical adoption of pure Ge channels [6.47].

To overcome these drawbacks, graded SiGe channels were introduced. By gradually varying the germanium mole fraction, graded channels improved electrostatic

control, maximized transconductance, and reduced defect formation [6.48]. Early implementations using SiGe FETs with spacer layers and Schottky gates showed reductions in gate leakage and improvements in hole mobility [6.49]. With further refinements, hybrid SiGe CMOS and SiGe FinFETs achieved high speed and scalability suitable for advanced technology nodes [6.50, 6.51]. Experimental works confirmed that devices such as $Si_{0.8}Ge_{0.2}$ and $Si_{0.5}Ge_{0.5}$ channels could deliver higher ON currents, lower OFF currents, and improved SS compared to conventional Si devices [6.52, 6.53]. However, vertically graded layers faced limitations due to critical thickness constraints and defect formation [6.54, 6.55].

6.2.4 Advances in TFET Biosensor Architectures

Recent efforts focused on optimizing TFET biosensors by incorporating advanced materials and structural engineering. For instance, Lee *et al.* demonstrated gate-all-around SiGe TFETs with high Ge content ($Si_{0.2}Ge_{0.8}$), achieving excellent SS and reduced leakage [6.56]. Meanwhile, Shih and Chien highlighted the benefits of graded SiGe heterojunctions for short-channel TFETs, demonstrating suppression of ambipolarity and optimization of tunneling barriers [6.57]. In biosensing contexts, dielectric modulation using cavities filled with biomolecules of varying permittivity (e.g., biotin, keratin, gelatin) allowed direct correlation of device electrical characteristics with molecular properties [6.58].

6.2.5 Comparative Insights and Current Research Directions

The progression from abrupt heterojunction TFETs (Ge–Ge–Si, Ge–Si–Si) to graded SiGe structures marks a crucial improvement in biosensor design. Abrupt heterostructures often suffered from large tunneling resistance, strain-induced defects, and limited electrostatic control. In contrast, graded SiGe configurations (Ge–Gr.SiGe–Si) provided smoother band transitions, minimized lattice mismatch, and reduced defect density. Simulation-driven studies using ATLAS Silvaco confirmed that graded channels yielded superior Ion/Ioff ratios, tunneling current efficiency, and dielectric sensitivity, particularly for biomolecules with higher permittivity values.

Synthesis: The literature shows a clear trajectory from conventional electrochemical biosensors [6.34] toward CMOS-compatible FET biosensors [6.35, 6.36], and subsequently toward TFET-based platforms exploiting band-to-band tunneling [6.37- 6.40]. The introduction of SiGe channels [6.46], followed by graded SiGe architectures [6.48- 6.53], resolved key performance bottlenecks by improving tunneling efficiency, defect tolerance, and dielectric sensitivity. Today, graded SiGe TFET biosensors represent the frontier, combining advanced materials with dielectric modulation to achieve high sensitivity, selectivity, and scalability for next-generation biomedical applications [6.56- 6.58].

6.3 Device structure, Theoretical foundation, Simulation Aspects

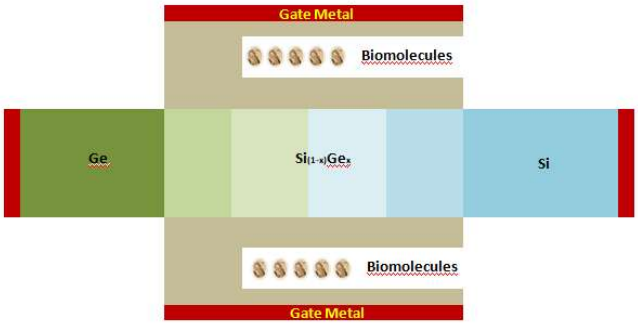

(a)

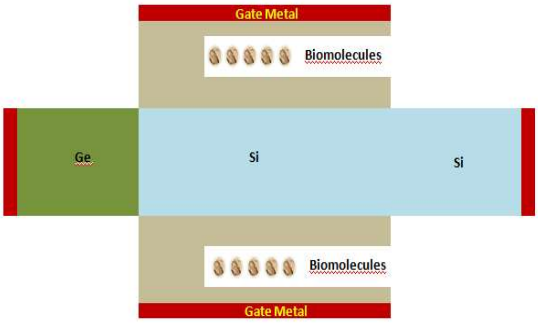

(b)

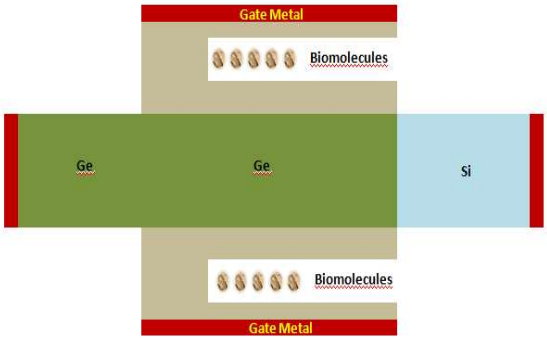

(c)

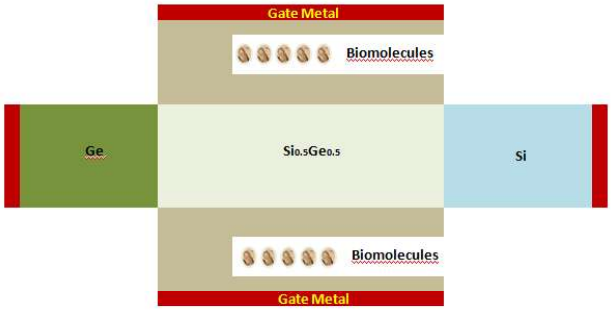

(d)

Fig. 6.1. (a) schematic picture of proposed graded channel TFET biosensor (b) Ge-Si-Si, (c) Ge-Ge-Si, (d) Ge-$Si_{0.5}Ge_{0.5}$-Si structures for comparative analysis

A schematic presentation of the device structure is given in Figure 6.1. The Parameters employed in the proposed device for modeling and simulation purposes are given in Table 6.1.

Table 6.1: Parameters utilized in the proposed device for modeling and simulation purposes

Parameters	**Value**
Source Length	10 nm
Intrinsic Channel Length	40 nm
Drain Length	10 nm
Thickness of Channel (t_{SiGe})	10 nm
Thickness of oxide layer (t_{ox})	1 nm
Device width (W)	20 nm

Work function of the gate metal (φm)	4.45 eV
Source region Concentration	$10^{20}(p)$
Intrinsic Chennel Concentration	$10^{16}(p)$cm-3
Drain Pocket Concentration	$10^{14}(p)$cm-3
Drain region Concentration	$10^{18}(n)c$m-3

For the device shown in figure 6.1, the 2-D Poisson equation is as follows:

$$:\frac{\partial^2\varphi(x.y)}{\partial x^2}+\frac{\partial^2\varphi(x.y)}{\partial y^2}=\frac{qn}{\epsilon_{ch}}, \quad \text{i=1,2,3,4, 5 as regions depicted in figure 6.1} \tag{6.1}$$

$\varphi(x.y)$ is the two-dimensional potential, n and q are the carrier density and charge, ϵ_{ch} is the dielectric permittivity.

From figure 6.1, the region *i* denotes the different region in the channel by Young's Parabolic approximation

$$\varphi_i(x,y)=\varphi_{s,i}(x)+ya_{1i}(x)+y^2a_{2i}(x) \quad \text{i=1,2,3,4,5} \tag{6.2}$$

Where $\varphi_i(x,y)\ is$ 2-D potential profile, $a_i(x)$ is one dimensional potential along length. To calculate $a_0, a_{1i}\ and\ a_{2i}$ we apply the boundary conditions as: -

1) $at\ y=0, \varphi_i(x,y)=\varphi_{s,i}(x)$
2) $\left.\frac{\partial\varphi_i(x,y)}{\partial y}\right|_{y=0}=a_{1i}(x)$ (6.3)
3) $\left.\frac{\partial\varphi_i(x,y)}{\partial y}\right|_{y=t(Si_{(1-mfi)}Ge_{(mfi)})}=a_{1i}(x)+2t_{Si_{(1-mfi)}Ge_{(mfi)}}a_{2i}(x)$

$\varphi_{s,i}(x)$ is the surface potential, $t\left(Si_{(1-mfi)}Ge_{(mfi)}\right)$ is the thickness of the graded channel. *'mfi'* denotes the Germanium mole fraction in Silicon in each region. Solving,

$$a_{2i}(x) = \frac{C_{ox}[V_{GS}-V_{fbi}-\varphi_{s,i}]}{t_{Si_{(1-mfi)}Ge_{(mfi)}}\epsilon_{Ge/Si_{(1-mfi)}Ge_{(mfi)}}}, a_{1i}(x) = \frac{-C_{ox}[V_{GS}-V_{fbi}-\varphi_{s,i}]}{t_{Si_{(1-mfi)}Ge_{(mfi)}}\epsilon_{Ge/Si_{(1-mfi)}Ge_{(mfi)}}} \quad (6.4)$$

V_{GS} is the gate to source voltage, V_{fbi} is the flat-band voltage corresponding to every region, ϵ is the permittivity. C_{ox} is the oxide capacitance. Now 1-D equation takes the form,

$$\frac{\partial^2\varphi_{s,i}(x)}{\partial x^2} - \frac{\varphi_{s,i}(x)-(V_{GS}-V_{fbi})}{\lambda_i^2} = \frac{qN_i}{\epsilon_{Ge/Si_{(1-mfi)}Ge_{(mfi)}}} \quad (6.5)$$

λ_i is the characteristics length given by, $\lambda_i = \sqrt{\frac{t_{Ge/Si_{(1-mfi)}Ge_{(mfi)}}\epsilon_{Si_{(1-mfi)}Ge_{(mfi)}}}{2C_{HfO2}}}$ (6.6)

Here, $2/\pi$ is multiplied in the denominator to consider fringing field effects.

The general solution of the above differential equation,

$$\varphi_{S,i}(x) = \alpha_i \exp\left(\frac{x}{\lambda_i}\right) + \beta_i \exp\left(-\frac{x}{\lambda_i}\right) + \sigma_i, \text{ where, } \sigma_i = V_{GS} - V_{fb,i} - \frac{qN_i}{\epsilon_{Ge/Si_{(1-mfi)}Ge_{(mfi)}}}\lambda_i^2, \quad (6.7)$$

In this study, we have simulated four distinct TFET structures to analyze their performance as biosensors: Ge-SiGe graded-Si (denoted as Ge_Gr.SiGe_Si), Ge-Si-Si, Ge-Ge-Si, and Ge-$Si_{0.5}Ge_{0.5}$-Si, as shown in figure 6.1(a,b,c,d) respectively. Each structure represents a unique approach to enhancing tunneling efficiency and sensitivity to dielectric modulation. The Ge-Ge-Si configuration utilizes a heterojunction with abrupt transitions, while the Ge-Si-Si structure incorporates a conventional Si drain. The Ge-$Si_{0.5}Ge_{0.5}$-Si design introduces an intermediate SiGe layer for smoother bandgap alignment, and the Ge-SiGe graded-Si structure employs a graded composition to minimize lattice mismatch and optimize band-to-band tunneling. These structures are modeled to explore their potential for high-sensitivity biosensing, focusing on their dielectric modulation response and overall electrostatic control. To analyze the device characteristics, ATLAS Silvaco had been applied in the simulation. Along with local BTBT model, FD statistics, DD carrier transport, SRH recombination model, bandgap narrowing are employed. Kane's mode is used to calculate Band to band tunneling generation rate at uniform electric

field where [6.13] P is considered 2.5 for indirect tunneling and calibrated [6.23]. For the simulation environment, we have considered dielectric constant values (k=2,4,6,9,12) corresponding to biomolecules such as Biotin, Ferro-cytochrome, Bacteriophage T7, Keratin, and Gelatin [6.25].

From fabrication aspect, the arrangement can be grown on a silicon substrate followed by the layers of graded SiGe and SiO_2 for gate oxide, respectively. From a fabrication aspect, the possible fabrication process begins with SOI substrates, where initial characterization using nano-beam and X-ray diffraction confirms minimal strain. Selective epitaxial growth methods are generally used for the formation of SiGe and Si layers with specific grading profiles. Ultrahigh vacuum chemical vapor deposition (UHV-CVD) is employed for selective epitaxial growth [6.26]. Subsequently, gate dielectric is generally formed via rapid thermal oxidation. Dopants at source/drain are implanted followed by activation with rapid thermal annealing where cavities can be etched out by buffered HF. The development of materials with precise compositional is achieved such as chemical vapor deposition, metal-assisted vapor-liquid-solid (VLS) growth techniques, laser ablation with thermal evaporation and dynamic shadowing deposition [6.27-6.32]. Experimentally, the lower heat conductivity of $Si/Si_{1-x}Ge_x$ superlattices (SLs) with compositional gradients has been observed both in theory and in practice [6.33]. Zhang et al showed through MD simulations that the heat conductivity of compositionally graded SiGe nanowires (NWs) can decrease by as much as 57% when contrasted with SiGe NWs featuring sharp interfaces [6.27]. They introduced a compositional gradient ranging from 90% to 50% and 10% to 50% in the area near the SiGe interface.

6.3 Results and Discussion

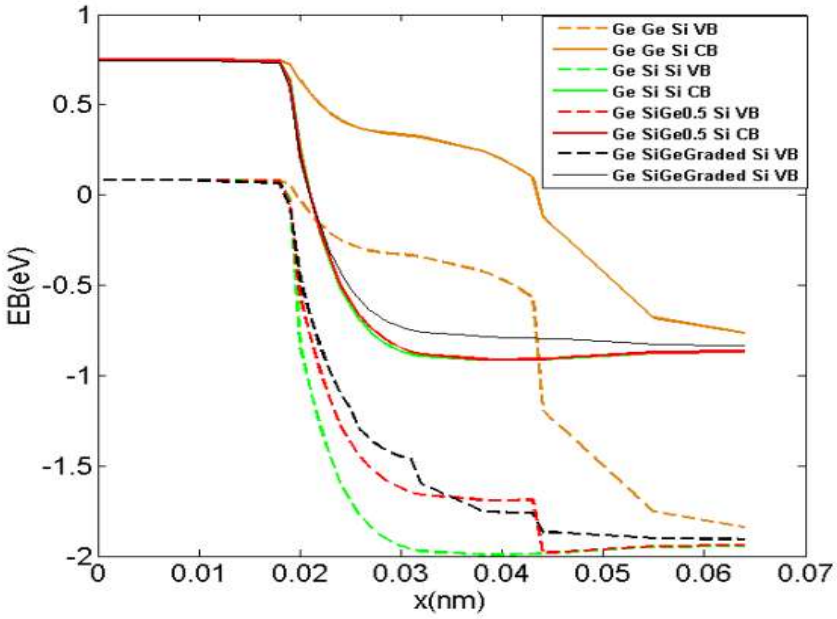

Figure 6.2: Energy band diagram of the proposed Graded SiGe channel Dielectric Modulated Tunnel FET BioSensor

In the context of the Graded SiGe channel Dielectric Modulated Tunnel FET BioSensor, the energy band diagram (Figure 6.2) reveals significant variations in tunneling distance based on different configurations. The Ge-Ge-Si configuration offers the highest tunneling distance due to the substantial bandgap difference between the Ge source and the Si drain, which creates a more substantial *Energy band* barrier for electrons to tunnel through. In contrast, configurations such as Ge_Gr.SiGe_Si, Ge-$Si_{0.5}Ge_{0.5}$-Si, and Ge-Si-Si exhibit shorter tunneling distances. This is because the graded SiGe layers and the intermediate $Si_{0.5}Ge_{0.5}$ layer in these configurations provide a more gradual transition in the energy band, reducing the overall potential barrier height and width. Consequently, the electrons encounter a narrower and less abrupt barrier, facilitating easier tunneling. The Ge-Si-Si structure, while also having a significant bandgap difference, presents a relatively moderate tunneling distance compared to Ge-Ge-Si due to the direct Ge to Si transition without the intermediate graded layer, resulting in a different tunneling

profile. The varied tunneling distances directly impact the device's performance, affecting the ON-state current and the overall efficiency of the TFET BioSensor.

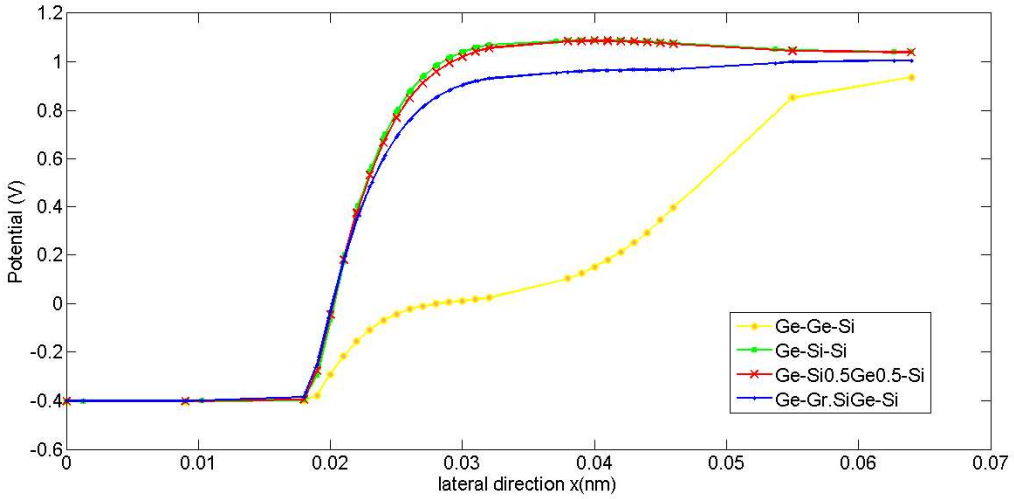

Figure 6.3: Potential Energy Curves for Different Semiconductor Structures

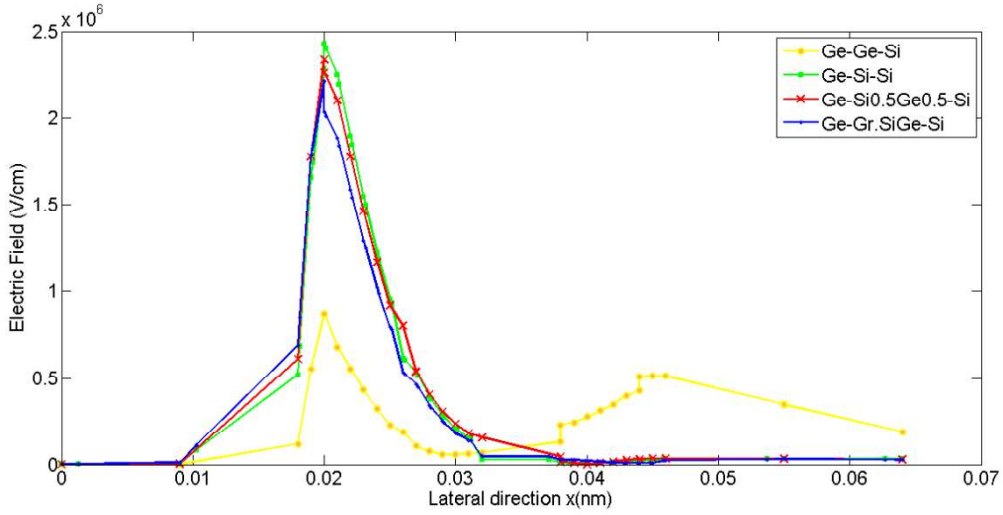

Figure 6.4: Electric field distribution in TFETs showing the impact of different semiconductor structures

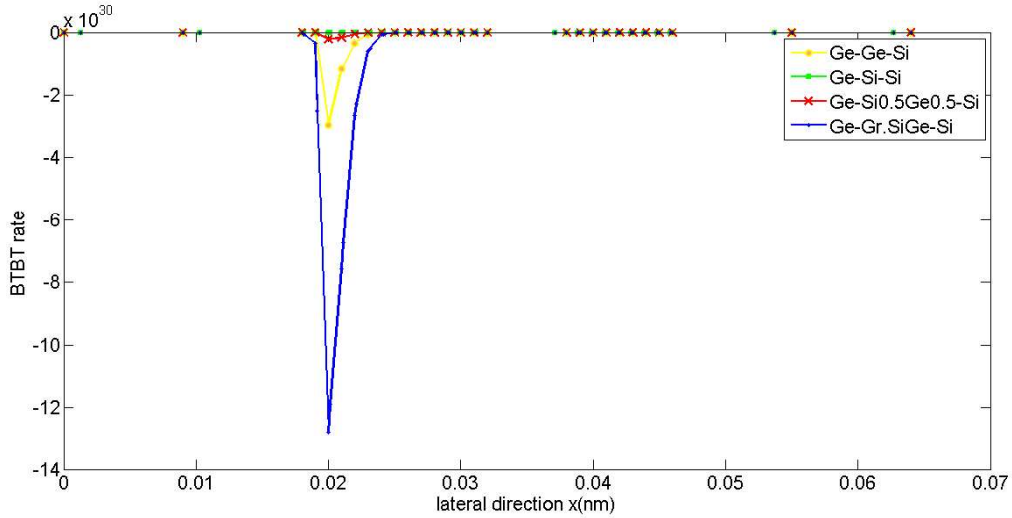

Figure 6.5: BTBT plot comparing the tunneling current at the source side for various configurations using the local tunneling model

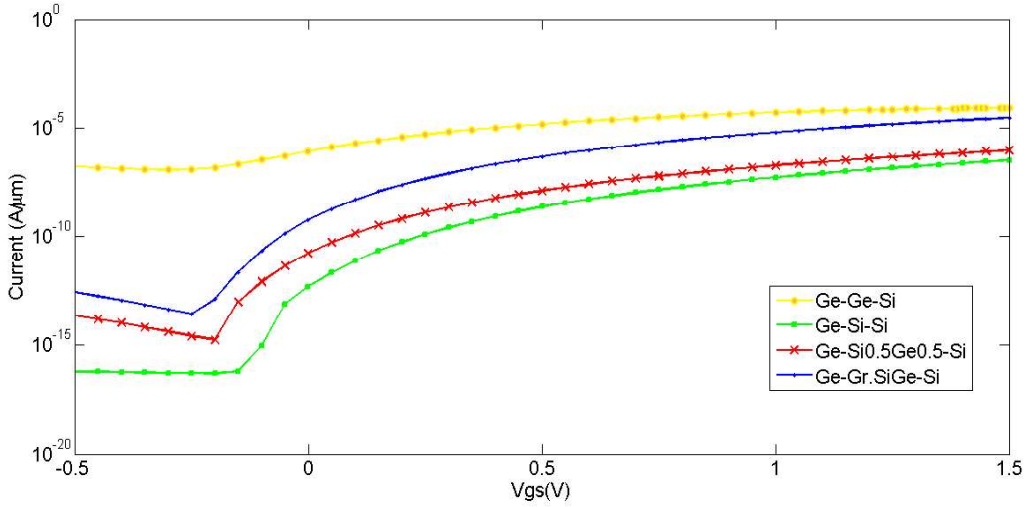

Figure 6.6: Current drain voltage graph illustrating the trade-offs between Ion/Ioff ratio, ambipolarity, and on-current for various SiGe graded structures

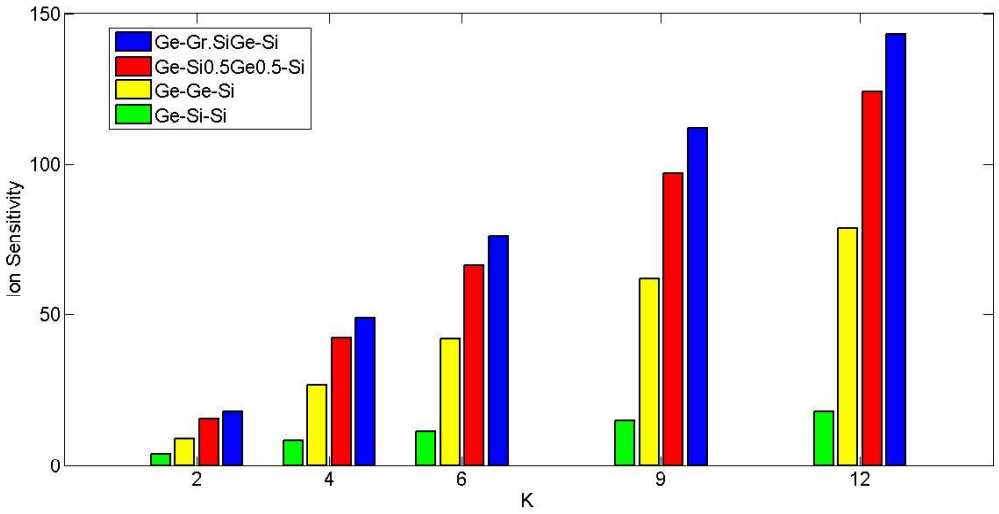

Figure 6.7: Comparison of Ion sensitivity between Ge-Ge-Si, Ge-Si-Si, Ge- $Si_{0.5}Ge_{0.5}$-Si, and Ge_Gr.SiGe_Si - models as a function of biosensor permittivity

The potential energy curves in Figure 6.3 illustrate the variations across different semiconductor interfaces, highlighting their impact on strain relaxation and defect dynamics. The Ge-Ge-Si structure shows a smoother potential rise due to similar lattice constants but struggles with managing strain and defects, affecting performance. In contrast, the Ge-Si-Si and Ge-$Si_{0.5}Ge_{0.5}$-Si structures exhibit sharp potential changes, resulting in high strain, lattice mismatch, and a greater propensity for threading dislocations (TDs) and other defects. The Ge_Gr.SiGe_Si structure, with its gradual Ge mole fraction transition, effectively reduces lattice mismatch and strain, minimizing defects and improving the crystal quality of the Ge-$Si_{0.5}Ge_{0.5}$-Si channel layer.

Figure 6.4 shows the electric field distribution across different structures, with the sharpest increase near the source for Ge-Si-Si, enhancing tunneling but increasing defect risks. The Ge_Gr.SiGe_Si structure displays a smoother electric field profile, reducing lattice mismatch and strain, thus lowering defect density, and improving reliability. This balance makes the Ge_Gr.SiGe_Si structure particularly advantageous for integrating high-mobility SiGe channels in advanced devices, enabling better performance and scalability.

A comparative analysis in figure 6.5 shows the rate of increase in BTBT follows the sequence: Ge-Si-Si, Ge-$Si_{0.5}Ge_{0.5}$-Si, Ge-Ge-Si, and Ge_Gr.SiGe_Si. The Ge-Si-Si configuration exhibits the steepest increase in BTBT due to its abrupt transition, which creates a significant potential barrier that enhances tunneling rates. In the Ge-Ge-$Si_{0.5}Ge_{0.5}$-Si -Si and Ge-Ge-Si configurations, intermediate SiGe layers smooth the potential transition, reducing the tunneling barrier and moderating the BTBT rate compared to Ge-Si-Si. The Ge_Gr.SiGe_Si structure further improves tunneling efficiency due to its gradual potential variation, enhancing the process more effectively.

The current drain voltage graph in figure 6.6 reveals that the Ge-Si-Ge structure has the lowest Ion/Ioff ratio, indicating poor on-off current differentiation. The Ge-Si-Si structure, while exhibiting the lowest ambipolarity, fails to produce significant on-current due to less effective carrier transport. In contrast, the Ge-$Si_{0.5}Ge_{0.5}$-Si structure shows higher ambipolarity but also higher on-current, as the presence of Ge enhances carrier mobility, increasing current. The Ge_Gr.SiGe_Si structure strikes a balance by optimizing the Ion/Ioff ratio, providing improved performance with an increase in ambipolarity similar to the Ge-$Si_{0.5}Ge_{0.5}$-Si structure. This optimization is attributed to the graded SiGe layer, which effectively manages strain and reduces defects, facilitating better tunneling and carrier transport, thereby enhancing TFET operation.

In figure 6.7, the Ion sensitivity of the proposed biosensor structures was evaluated for dielectric constants (k=2,4,6,9,12), with the results highlighting distinct performance trends. The Ge-Ge-Si structure exhibited moderate sensitivity, with values of 8.97, 26.58, 42.02, 61.81, and 78.60, respectively. Its sensitivity increases with k due to efficient tunneling at the Ge/Si heterojunction but is limited by higher ambipolarity and abrupt band transitions. The Ge-Si-Si configuration showed the lowest sensitivity, with values of 3.85, 8.26, 11.25, 14.70, and 17.49, resulting from significant tunneling resistance due to abrupt Ge/Si and Si/Si interfaces, which hinder BTBT efficiency. The Ge-$Si_{0.5}Ge_{0.5}$-Si structure provided significantly higher sensitivity, with values of 15.31, 42.42, 66.08, 96.91, and 123.63, benefiting from the intermediate SiGe layer that smoothens the bandgap transition and reduces

tunneling resistance. The highest sensitivity was observed in the Ge_Gr.SiGe_Si structure, with values of 17.47, 48.70, 76.09, 111.84, and 142.79, due to its graded composition, which creates a continuous potential barrier, minimizes lattice mismatch, and reduces defect density. This design ensures enhanced tunneling efficiency and amplifies the device's response to dielectric variations, making it the most suitable for high-sensitivity biosensing applications

For selectivity of k=2 with respect to other bimolecular dielectricity, Ge-Si-Si achieves the highest values 46.57, Ge-Gr.SiGe-Si shows slightly lower but comparable values to Ge-$Si_{0.5}Ge_{0.5}$-Si, indicating its effectiveness in low-dielectric environments. Ge-Ge-Si shows consistently lower selectivity compared to graded structures, with a steep decline as k increases. For selectivity of k=4 the Ge-Ge-Si structure demonstrates the highest selectivity for k=4/2 (296.27), followed by Ge-$Si_{0.5}Ge_{0.5}$-Si (277.13) and Gr.SiGe-Si (278.59) emphasizing their suitability for intermediate contrasts. For Selectivity of k=6, Gr.SiGe-Si and Ge-$Si_{0.5}Ge_{0.5}$-Si alternate as the best performers in this range, with near-identical selectivity values for all k. Ge-Ge-Si and Ge-Si-Si shows weaker performance in this range. For Selectivity of k=9 and k=12, Graded SiGe-Si and Ge-$Si_{0.5}Ge_{0.5}$-Si consistently outperform others in high dielectric contrast scenarios. For k=12/2, the Graded SiGe-Si structure achieves the highest selectivity (815.71), followed closely by Ge-$Si_{0.5}Ge_{0.5}$-Si (807.54). Ge-Ge-Si performs well in extreme ratios but shows a sharper decline in intermediate ranges. Ge-Si-Si remains the weakest across all high-dielectric contrast cases due to its abrupt interfaces and limited electrostatic control. Graded and intermediate SiGe structures show superior scalability, sensitivity and maintain consistent performance across all k.

The below mentioned data compares the selectivity values (defined as the ratio of sensitivities) of four TFET-based biosensor structures—Ge-Ge-Si, Ge-Si-Si, Ge-$Si_{0.5}Ge_{0.5}$-Si, and Graded SiGe-Si—under various dielectric constant (k) ratios.

Table 6.2: Selectivity for k=2 with respect to k=4,6,9,12

	Selectivity with respect to k=4	Selectivity with respect to k=6	Selectivity with respect to k=9	Selectivity with respect to k=12
Ge –Ge- Si	33.75278	21.34846	14.51167	11.41209
Ge -Si -Si	46.56948	34.19523	26.18202	22.00104
Ge -$Si_{0.5}Ge_{0.5}$ -Si	36.08461	23.16738	15.79636	12.38329
Ge -Gr. SiGe -Si	35.89538	22.9855	15.64552	12.25922

Table 6.3: Selectivity for k=4 with respect to k=2,6,9,12

	Selectivity with respect to k=2	Selectivity with respect to k=6	Selectivity with respect to k=9	Selectivity with respect to k=12
Ge –Ge- Si	296.2719	63.24948	42.99399	33.81081
Ge -Si -Si	214.7329	73.42842	56.22142	47.24348
Ge -$Si_{0.5}Ge_{0.5}$ -Si	277.1265	64.20295	43.7759	34.31739
Ge -Gr. SiGe -Si	278.5874	64.03472	43.58644	34.15265

Table 6.4: Selectivity for k=6 with respect to k=2,4,9,12

	Selectivity with respect to k=2	Selectivity with respect to k=4	Selectivity with respect to k=9	Selectivity with respect to k=12
Ge –Ge- Si	468.4179	158.1041	67.97524	53.45626
Ge -Si -Si	292.4385	136.1871	76.5663	64.33951
Ge -$Si_{0.5}Ge_{0.5}$ -Si	431.6414	155.7561	68.18362	53.45142
Ge -Gr. SiGe -Si	435.0568	156.1653	68.06688	53.33457

Table 6.5: Selectivity for k=9 with respect to k=2,4,6,12

	Selectivity with respect to k=2	Selectivity with respect to k=4	Selectivity with respect to k=6	Selectivity with respect to k=12
Ge –Ge- Si	689.1007	232.5907	147.1124	78.64078
Ge -Si -Si	381.9415	177.8681	130.6058	84.03111
Ge -$Si_{0.5}Ge_{0.5}$ -Si	633.0572	228.4362	146.6628	78.39334
Ge -Gr. SiGe -Si	639.1608	229.4292	146.9143	78.35613

Table 6.6: Selectivity for k=12 with respect to 2,4,6,9

	Selectivity with respect to k=2	Selectivity with respect to k=4	Selectivity with respect to k=6	Selectivity with respect to k=9
Ge –Ge- Si	876.2639	295.7634	187.0688	127.1605
Ge -Si -Si	454.5239	211.6694	155.4255	119.0036
Ge -$Si_{0.5}Ge_{0.5}$ -Si	807.5396	291.3975	187.0858	127.5619
Ge -Gr. SiGe -Si	815.7126	292.8031	187.4957	127.6224

References

[6.1] Varnakavi. Naresh and N. Lee, "A Review on Biosensors and Recent Development of Nanostructured Materials-Enabled Biosensors," Sensors, vol. 21, no. 4, p. 1109, Feb. 2021, doi: https://doi.org/10.3390/s21041109.

[6.2] D. Sarkar and K. Banerjee, "Fundamental limitations of conventional-FET biosensors: Quantum-mechanical-tunneling to the rescue," 70th Device Research Conference, University Park, PA, USA, 2012, pp. 83-84, doi: 10.1109/DRC.2012.6256950.

[6.3] R. Misra, K. Singh, A. Agarwal, R. Rastogi, and S. Dubey, "Electronic Noise Analysis of Source-Engineered Phosphorene/Si Heterojunction Dopingless Tunnel-FET," Silicon, vol. 15, no. 1, pp. 263–267, Jul. 2022, doi: https://doi.org/10.1007/s12633-022-02019-5.

[6.4] Sarkar, S.; Banerjee, K. Fundamental limitations of conventional-FET biosensors: Quantum-mechanical-tunneling to the rescue. In Proceedings of the 70th Device Research Conference, University Park, PA, USA, 18–20 June 2012; pp. 83–84.

[6.5] Narang, R.; Reddy, K.V.S.; Saxena, M.; Gupta, R.S.; Gupta, M. A Dielectric-Modulated Tunnel-FET-Based Biosensor for Label-Free Detection: Analytical Modeling Study and Sensitivity Analysis. IEEE Trans. Electron Devices 2012, 59, 2809–2817.

[6.6] Narang, R.; Saxena, M.; Gupta, R.S.; Gupta, M. Dielectric Modulated Tunnel Field-Effect Transistor—A Biomolecule Sensor. IEEE Electron Device Lett. 2012, 33, 266–268.

[6.7] Kanungo, S.; Chattopadhyay, S.; Gupta, P.S.; Rahman, H. Comparative Performance Analysis of the Dielectrically Modulated Full-Gate and Short-Gate Tunnel FET-Based Biosensors. IEEE Trans. Electron Devices 2015, 62, 994–1001.

[6.8] Anam, A.; Anand., S.; Amin, S.I. Design and Performance Analysis of Tunnel Field Effect Transistor with Buried Strained Si1−xGex Source Structure Based Biosensor for Sensitivity Enhancement. IEEE Sens. J. 2020, 20, 13178–13185.

[6.9] Arimura, E. Capogreco, A. Vohra et al., (2020) Toward high-performance and reliable Ge channel devices for 2 nm node and beyond. In: 2020 IEEE International Electron Devices Meeting (IEDM). IEEE, San Francisco, CA, USA, p 2.1.1–2.1.4

[6.10] J. Mitard, L. Witters, Y. Sasaki et al., (2016) A 2nd Generation of 14/16nm-node compatible strained-Ge pFINFET with improved performance with respect to advanced Si-channel FinFETs. In: 2016 IEEE Symposium on VLSI Technology. pp 1–2

[6.11] Y. Li, F. Zhao, X. Cheng et al., Integration of Si0. 7Ge0. 3 fin onto a bulk-Si substrate and its P-type FinFET device fabrication. Semicond. Sci. Technol. 36, 125001 (2021)

[6.12] Maximilian Georg Bartmann et al., "Verifying the band gap narrowing in tensile strained Ge nanowires by electrical means," Nanotechnology, vol. 32, no. 14, pp. 145711–145711, Jan. 2021, doi: https://doi.org/10.1088/1361-6528/abd0b2.

[6.13] Kim, G.; Lee, J.; Kim, J.H.; Kim, S. High On-Current Ge-Channel Heterojunction Tunnel Field-Effect Transistor Using Direct Band-to-Band Tunneling. Micromachines 2019, 10, 77. https://doi.org/10.3390/mi10020077

[6.14] L. Witters, G. Eneman, J. Mitard et al., Integration aspects of strained Ge pFETs. Solid State Electron. 98, 7–11 (2014). https://doi.org/10.1016/j.sse.2014.04.009

[6.15] S. Verdonckt-Vandebroek et al., "SiGe-channel heterojunction p-MOSFET's," in IEEE Transactions on Electron Devices, vol. 41, no. 1, pp. 90-101, Jan. 1994, doi: 10.1109/16.259625.

[6.16] K. Cheng et al., "High performance extremely thin SOI (ETSOI) hybrid CMOS with Si channel NFET and strained SiGe channel PFET," 2012 International Electron Devices Meeting, San Francisco, CA, USA, 2012, pp. 18.1.1-18.1.4, doi: 10.1109/IEDM.2012.6479063.

[6.17] D. Guo et al., "FINFET technology featuring high mobility SiGe channel for 10nm and beyond," 2016 IEEE Symposium on VLSI Technology, Honolulu, HI, USA, 2016, pp. 1-2, doi: 10.1109/VLSIT.2016.7573360.

[6.18] C. H. Lee et al., "Toward High Performance SiGe Channel CMOS: Design of High Electron Mobility in SiGe nFinFETs Outperforming Si," 2018 IEEE International Electron Devices Meeting (IEDM), San Francisco, CA, USA, 2018, pp. 35.1.1-35.1.4, doi: 10.1109/IEDM.2018.8614581.

[6.19] C.-J. Sun et al., "Low Ge Content Ultra-Thin Fin Width (5nm) Monocrystalline SiGe n-Type FinFET With Low Off State Leakage and High

ION/IOFF Ratio," IEEE Journal of the Electron Devices Society, vol. 8, pp. 1016–1020, 2020, doi: https://doi.org/10.1109/jeds.2020.3023953.

[6.20] Y. Li et al., "A novel approach to Si0.5Ge0.5 channel FinFET fabrication: utilizing a three-layer SiGe strain relaxation buffer and In-Situ phosphorus doping," Journal of materials science. Materials in electronics, vol. 35, no. 6, Feb. 2024, doi: https://doi.org/10.1007/s10854-024-12174-7.

[6.21] B. Vincent et al., "The Ge condensation technique: A solution for planar SOI/GeOI co-integration for advanced CMOS technologies?," Materials science in semiconductor processing, vol. 11, no. 5–6, pp. 205–213, Oct. 2008, doi: https://doi.org/10.1016/j.mssp.2008.10.005.

[6.22] N. D. Chien, "Design Optimization Of Extremely Short-Channel Graded Si/Sige Heterojunction Tunnel Field-Effect Transistors For Low Power Applications," Vietnam Journal of Science and Technology, vol. 51, no. 6, p. 757, Mar. 2018, doi: https://doi.org/10.15625/2525-2518/51/6/11642.

[6.23] R. Lee et al., "Vertically-Stacked Si0.2Ge0.8 Nanosheet Tunnel FET With 70 mV/Dec Average Subthreshold Swing," in IEEE Electron Device Letters, vol. 42, no. 7, pp. 962-965, July 2021, doi: 10.1109/LED.2021.3079246.

[6.24] C. Shih and Nguyễn Đăng Chiến, "Physical operation and device design of short-channel tunnel field-effect transistors with graded silicon-germanium heterojunctions," Journal of Applied Physics, vol. 113, no. 13, Apr. 2013, doi: https://doi.org/10.1063/1.4795777.

[6.25] S. Choudhury, Krishna Lal Baishnab, K. Guha, Zoran Jakšić, O. Jakšić, and J. Iannacci, "Modeling and Simulation of a TFET-Based Label-Free Biosensor with Enhanced Sensitivity," vol. 11, no. 5, pp. 312–312, May 2023, doi: https://doi.org/10.3390/chemosensors11050312.

[6.26]Grace Huiqi Wang, E.-H. Toh, C.-H. Tung, S. Tripathy, G. S. Samudra, and Y.-C. Yeo, "Concept of Strain-Transfer-Layer and Integration with Graded Silicon–Germanium Source/Drain Stressors for p-Type Field Effect Transistor Performance Enhancement," Japanese journal of applied physics, vol. 47, no. 4S, pp. 2551–2551, Apr. 2008, doi: https://doi.org/10.1143/jjap.47.2551.

[6.27] H. Zhang, H. Han, S. Xiong, H. Wang, S. Volz, and Y. Ni, "Impeded thermal transport in composition graded SiGe nanowires," Appl. Phys. Lett., vol. 111, no. 12, Sep. 2017, doi: 10.1063/1.4998998.

[6.28] T. Kuykendall, P. Ulrich, S. Aloni, and P. Yang, "Silicon-germanium nanowires," Nat. Mater., vol. 6, pp. 951, 2007.

[6.29] Y. Liu, J. A. Zapien, Y. Y. Shan, C. Y. Geng, C. S. Lee, and S. T. Lee, "Synthesis and characterization of silicon-germanium nanowires," Adv. Mater., vol. 17, pp. 1372, 2005.

[6.30] A. Pan, R. Liu, M. Sun, and C. Ning, "Controlled synthesis of single crystalline silicon nanowires," ACS Nano, vol. 4, pp. 671, 2010.

[6.31] S. Larson and Y. Zhao, "Nanostructured materials for energy applications," Nanotechnology, vol. 27, no. 255401, 2016.

[6.32] Y. He, J. Fan, and Y. Zhao, "Alleviating strain in Ge films by organic-inorganic hybrid materials," Cryst. Growth Des., vol. 10, pp. 4954, 2010.

[6.33] P. Ferrandovillalba, A. F. Lopeandia, F. X. Alvarez, B. Paul, C. De Tomas, M. I. Alonso, M. Garriga, A. R. Goni, J. Santiso, G. Garcia, et al., "Nano-engineered materials for various applications," Nano Res., vol. 8, pp. 2833, 2015.

[6.34] V. Naresh and N. Lee, "A review on biosensors and recent development of nanostructured materials-enabled biosensors," Sensors, vol. 21, no. 4, p. 1109, Feb. 2021.

[6.35] D. Sarkar and K. Banerjee, "Fundamental limitations of conventional-FET biosensors: Quantum-mechanical-tunneling to the rescue," in Proc. 70th Device Research Conf., University Park, PA, USA, 2012, pp. 83–84.

[6.36] R. Misra, K. Singh, A. Agarwal, R. Rastogi, and S. Dubey, "Electronic noise analysis of source-engineered phosphorene/Si heterojunction dopingless tunnel-FET," *Silicon*, vol. 15, no. 1, pp. 263–267, Jul. 2022.

[6.37] R. Narang, K. V. S. Reddy, M. Saxena, R. S. Gupta, and M. Gupta, "A dielectric-modulated tunnel-FET-based biosensor for label-free detection: Analytical modeling study and sensitivity analysis," *IEEE Trans. Electron Devices*, vol. 59, no. 9, pp. 2809–2817, 2012.

[6.38] R. Narang, M. Saxena, R. S. Gupta, and M. Gupta, "Dielectric-modulated tunnel field-effect transistor—A biomolecule sensor," *IEEE Electron Device Lett.*, vol. 33, no. 2, pp. 266–268, 2012.

[6.39] S. Kanungo, S. Chattopadhyay, P. S. Gupta, and H. Rahman, "Comparative performance analysis of the dielectrically modulated full-gate and short-gate tunnel FET-based biosensors," *IEEE Trans. Electron Devices*, vol. 62, no. 3, pp. 994–1001, 2015.

[6.40] A. Anam, S. Anand, and S. I. Amin, "Design and performance analysis of tunnel field effect transistor with buried strained $Si_{1-x}Ge_x$ source structure based biosensor for sensitivity enhancement," *IEEE Sens. J.*, vol. 20, no. 22, pp. 13178–13185, 2020.

[6.41] E. Arimura, A. Capogreco, A. Vohra *et al.*, "Toward high-performance and reliable Ge channel devices for 2 nm node and beyond," in *IEDM Tech. Dig.*, IEEE, San Francisco, CA, USA, 2020, pp. 2.1.1–2.1.4.

[6.42] J. Mitard, L. Witters, Y. Sasaki *et al.*, "A 2nd generation of 14/16 nm-node compatible strained-Ge pFINFET with improved performance with respect to advanced Si-channel FinFETs," in *Proc. Symp. VLSI Technol.*, 2016, pp. 1–2.

[6.43] Y. Li, F. Zhao, X. Cheng *et al.*, "Integration of $Si_{0.7}Ge_{0.3}$ fin onto a bulk-Si substrate and its P-type FinFET device fabrication," *Semicond. Sci. Technol.*, vol. 36, p. 125001, 2021.

[6.44] M. G. Bartmann *et al.*, "Verifying the band gap narrowing in tensile strained Ge nanowires by electrical means," *Nanotechnology*, vol. 32, no. 14, p. 145711, 2021.

[6.45] G. Kim, J. Lee, J. H. Kim, and S. Kim, "High on-current Ge-channel heterojunction tunnel field-effect transistor using direct band-to-band tunneling," *Micromachines*, vol. 10, no. 2, p. 77, 2019.

[6.46] L. Witters, G. Eneman, J. Mitard *et al.*, "Integration aspects of strained Ge pFETs," *Solid-State Electron.*, vol. 98, pp. 7–11, 2014.

[6.47] S. Verdonckt-Vandebroek *et al.*, "SiGe-channel heterojunction p-MOSFET's," *IEEE Trans. Electron Devices*, vol. 41, no. 1, pp. 90–101, Jan. 1994.

[6.48] K. Cheng *et al.*, "High performance extremely thin SOI hybrid CMOS with Si channel NFET and strained SiGe channel PFET," in *IEDM Tech. Dig.*, 2012, pp. 18.1.1–18.1.4.

[6.49] D. Guo *et al.*, "FINFET technology featuring high mobility SiGe channel for 10 nm and beyond," in *Proc. Symp. VLSI Technol.*, 2016, pp. 1–2.

[6.50] C. H. Lee *et al.*, "Toward high performance SiGe channel CMOS: Design of high electron mobility in SiGe nFinFETs outperforming Si," in *IEDM Tech. Dig.*, 2018, pp. 35.1.1–35.1.4.

[6.51] C.-J. Sun *et al.*, "Low Ge content ultra-thin fin width (5 nm) monocrystalline SiGe n-type FinFET with low off state leakage and high Ion/Ioff ratio," *IEEE J. Electron Devices Soc.*, vol. 8, pp. 1016–1020, 2020.

[6.52] Y. Li *et al.*, "A novel approach to $Si_{0.5}Ge_{0.5}$ channel FinFET fabrication: Utilizing a three-layer SiGe strain relaxation buffer and in-situ phosphorus doping," *J. Mater. Sci. Mater. Electron.*, vol. 35, no. 6, 2024.

[6.53] B. Vincent *et al.*, "The Ge condensation technique: A solution for planar SOI/GeOI co-integration for advanced CMOS technologies?," *Mater. Sci. Semicond. Process.*, vol. 11, no. 5–6, pp. 205–213, 2008.

[6.54] N. D. Chien, "Design optimization of extremely short-channel graded Si/SiGe heterojunction tunnel field-effect transistors for low power applications," *Vietnam J. Sci. Technol.*, vol. 51, no. 6, pp. 757–764, 2018.

[6.55] R. Lee *et al.*, "Vertically-stacked $Si_{0.2}Ge_{0.8}$ nanosheet tunnel FET with 70 mV/dec average subthreshold swing," *IEEE Electron Device Lett.*, vol. 42, no. 7, pp. 962–965, 2021.

[6.56] C. Shih and N. D. Chiến, "Physical operation and device design of short-channel tunnel field-effect transistors with graded silicon–germanium heterojunctions," *J. Appl. Phys.*, vol. 113, no. 13, 2013.

[6.57] S. Choudhury, K. L. Baishnab, K. Guha, Z. Jakšić, O. Jakšić, and J. Iannacci, "Modeling and simulation of a TFET-based label-free biosensor with enhanced sensitivity," *Chemosensors*, vol. 11, no. 5, p. 312, 2023.

[6.58] H. Zhang, H. Han, S. Xiong, H. Wang, S. Volz, and Y. Ni, "Impeded thermal transport in composition graded SiGe nanowires," *Appl. Phys. Lett.*, vol. 111, no. 12, 2017.

Chapter 7

Conclusion and Future Work

7.1 Conclusion

The overall research presented in this thesis consolidates the theoretical, simulation-based, and comparative studies of advanced nanostructured solar cells and sensors, emphasizing the integration of material science, semiconductor physics, and device engineering. The work provides a comprehensive understanding of how nanoscale modification and heterostructure design can significantly enhance energy conversion efficiency and sensing performance in emerging photovoltaic and sensor technologies.

The first phase of this research focused on the Axially Graded $Si_{(1-x)}Ge_{(x)}$ Nanowire Solar Cell, which introduced a compositional gradient along the nanowire axis to optimize band alignment, carrier mobility, and optical absorption. Through Monte Carlo-based simulations, it was demonstrated that axial grading of germanium content allows smoother band transitions and improved carrier separation compared to abrupt heterojunction structures. This results in minimized recombination losses and an optimized built-in electric field, achieving notable improvement in short-circuit current density and conversion efficiency. The graded structure also successfully addressed the limitations of traditional Si or SiGe core–shell designs by maintaining structural compatibility and reducing strain-induced defects, providing a strong foundation for high-performance, cost-effective nanowire photovoltaics.

In the second phase, the research extended to Quantum Dot Metal Oxide for UV Ray Utilization in Tandem Solar Cells, where TiO_2 quantum dots were integrated as an

upper sub-cell material to exploit the high-energy ultraviolet spectrum. The study addressed a key bottleneck in conventional silicon and perovskite photovoltaics — their limited response in the UV region. By incorporating TiO_2 QDs in a tandem configuration, enhanced photon absorption and multiple exciton generation (MEG) were achieved, thereby extending the spectral range and improving quantum efficiency. The simulation and optical modeling indicated that quantum confinement effects within TiO_2 QDs significantly elevate electron excitation rates, thus enhancing photocurrent generation in tandem architectures. This work also established the design rule for optimal thickness, bandgap tuning, and interface passivation to suppress recombination and maintain stability under varying illumination conditions.

The third component of this research dealt with the Crossbar Architecture-Based Hydrogen Gas Sensor (CAS), a novel two-terminal silicon–palladium hybrid system proposed for high-density, scalable gas detection platforms. Using TCAD simulations coupled with a palladium-hydrogen adsorption model, the study provided computational insights into how work function modulation governs sensitivity and response characteristics. The analysis of interconnect resistance, array size, and sneak path current behavior revealed the trade-off between sensitivity and scalability in large crossbar networks. The proposed fabrication route offered a viable path for realizing compact, low-power hydrogen sensors compatible with semiconductor integration. This study also highlighted how crossbar geometry enables spatial mapping of sensing signals, transforming a traditional single-point measurement into a multidimensional, pattern-based detection system — an innovation directly applicable to Internet of Things (IoT) and environmental monitoring systems.

The final phase focused on Graded SiGe Channel Dielectric Modulated TFET Biosensors, where a novel Ge–SiGe–Si heterostructure was introduced to enhance label-free biomolecule detection. The graded channel structure was strategically engineered to overcome challenges such as low ON-current, high tunneling resistance, and interface-induced defects common in conventional TFET biosensors. Comparative analysis among Ge–Ge–Si, Ge–Si–Si, and Ge–$Si_{0.5}Ge_{0.5}$–Si configurations established that the graded SiGe channel offers superior performance,

achieving higher ON/OFF ratios, enhanced subthreshold swing, and improved Ion sensitivity across different biomolecular dielectric constants. The study concluded that graded SiGe channels minimize lattice mismatch and strain, reducing defect density and enabling precise electrostatic control. These findings contribute significantly to the design of ultra-sensitive, CMOS-compatible biosensors capable of real-time, label-free biological detection.

Collectively, the research outcomes validate that graded composition, quantum confinement, and nanoscale engineering are key enablers for next-generation nanodevices. Whether in photovoltaics or sensing, smooth energy band transitions, reduced defect densities, and optimized tunneling mechanisms are crucial to achieving higher efficiency and selectivity. Moreover, the integration of simulation and theoretical modeling with fabrication considerations bridges the gap between computational design and practical implementation, thereby enhancing device reliability and scalability. The synergy among these studies also establishes a common theme — that nanostructured semiconductor architectures not only improve energy conversion and detection efficiency but also pave the way for self-powered, intelligent sensor systems that merge energy harvesting with sensing functionality.

7.2 Future Work

While the current studies establish a solid foundation in simulation-driven nanodevice design, several avenues remain for extending this research toward experimental realization and multidisciplinary applications:

1. Experimental Fabrication and Characterization:

   Future work should aim to experimentally realize the proposed axially graded $Si_{(1-x)}Ge_{(x)}$ nanowires and TiO_2 quantum dot tandem structures. Techniques such as chemical vapor deposition (CVD), molecular beam epitaxy (MBE), and pulsed laser deposition (PLD) can be employed to fabricate controlled gradient profiles. Comprehensive characterization using XRD, TEM, PL, and I–V measurements will be essential to validate the simulated results and to study real-world issues like interface defects, carrier recombination, and thermal stability.

2. Integration of Solar Energy Harvesting with Sensors: Building on the demonstrated synergy between solar cells and sensors, a promising direction is to develop self-powered sensing systems where nanowire solar cells directly energize gas or biosensors. Such integration can lead to continuous, maintenance-free monitoring platforms for environmental and biomedical applications, especially in remote or resource-limited areas.

3. Exploration of Alternative Materials and Hybrid Architectures: Future investigations could extend the graded concept to other material systems such as perovskite/SiGe heterojunctions, MoS_2/graphene hybrid channels, or wide-bandgap semiconductors (e.g., ZnO, GaN) for UV and gas sensing. These combinations may yield multifunctional devices with tunable optical, electrical, and catalytic properties.

4. Advanced Modeling and Machine Learning Integration: Incorporating machine learning algorithms with TCAD and Monte Carlo simulations can accelerate design optimization by predicting complex parameter interactions. Such AI-driven models could enable real-time design feedback and parameter tuning for large-scale nanodevice networks like crossbar sensor arrays.

5. Miniaturization and Bio-Compatibility:

   The graded SiGe TFET biosensor can be advanced through biocompatible encapsulation layers and microfluidic integration for real-time bioassays. Scaling down to sub-10 nm gate lengths and exploring flexible substrates would make the devices suitable for wearable and implantable healthcare systems.

6. Reliability, Stability, and Long-Term Operation:

   Long-term performance analysis under varying environmental conditions (humidity, temperature, and radiation) remains essential. Future work should include accelerated aging tests and encapsulation strategies to ensure stable operation for field-deployed sensors and photovoltaic units.

7. Towards Quantum-Aware Nanodevices:

   Given the strong coupling between electronic confinement and charge transport in these devices, the next phase could involve quantum transport simulations and experimental verification of multiple exciton generation (MEG) and tunneling effects. These efforts could lead to quantum-engineered solar cells and sensors with unprecedented performance metrics.

7.3 Final Remarks

In conclusion, this thesis collectively demonstrates how nanoscale engineering—through composition grading, quantum confinement, and structural optimization—advances both solar energy harvesting and sensing technologies. The four studies bridge the domains of energy and detection, establishing a unified framework for designing high-efficiency, scalable, and self-sustaining nanodevices. These contributions not only advance scientific understanding but also provide a technological roadmap toward autonomous, intelligent, and sustainable energy–sensing ecosystems.

Abir Jana
24.06.2026